

Modelling of geomechanical performance of underground compressed air energy storage

Niels Tommelein

Master thesis submitted under the supervision of
Prof. Pierre Gerard

Academic year
2015-2016

In order to be awarded the Master's Degree in
Civil Engineering option Construction and Geomaterials

Modelling of geomechanical performance of underground compressed air energy storage

Niels Tommelein

Vrije Universiteit Brussel
Pleinlaan 2
1050 Brussel

Master of Science in
Civil Engineering option Construction and Geomaterials

Niels.Tommelein@vub.ac.be

June 2016

Keywords: CAES, Air leakage, Lined rock cavern, Geomechanical performance, Thermo-hydraulic analysis

abstract

The subject of this master thesis is the study of the thermo-hydraulic behaviour of underground compressed air energy storage. The effects of storage on the surroundings in combination with the efficiency of storage are the main objectives of this thesis. Simulations are performed in Lagamine finite element software for a 1D axisymmetric thermo-hydraulic model of 30m long. CAES-operation is simulated by daily cycles of 8h injection, 4h storing, 4h producing and 8h of stabilising. The daily average leakage is determined over 80 cycles. The unlined hydraulic model showed the need of a lining when the permeability is rather high ($>10^{-18}m^2$). The sensitivity analysis of the hydraulic lined model lead to a set of optimal parameters that allow reducing the leakage. A base pressure of 5.5MPa or slightly lower in a cavern with a high impermeable lining of $10^{-20} m^2$ and high air entry pressure (1.47MPa-14.7MPa) is advised. Rock parameters are less important but a high air entry pressure allows to reduce the leakage further. Injection during daily cycles happens at an injection rate of $7.913 \cdot 10^{-5}kg/s$ or preferentially higher with air that is cooled to temperatures that are close to the ambient temperature of the surrounding rock. The thermo-hydraulic model showed that the coupling between the temperature and pressure is low. The efficiency is best for a large cavern at high pressure after injection instead of smaller caverns at low pressure.

Modelleren van geotechnische performantie van ondergrondse energiestockage met gecomprimeerde lucht

Niels Tommelein

Vrije Universiteit Brussel
Pleinlaan 2
1050 Brussel

Master of Science in
Civil Engineering option Construction and Geomaterials

Niels.Tommelein@vub.ac.be

Juni 2016

Trefwoorden: CAES, lucht lekkage, afgesloten rots holte, geotechnische performantie, thermo-hydraulische analyse

samenvatting

Het onderwerp van deze masterthesis is de studie van het thermo-hydraulisch gedrag van ondergrondse energieopslag in holtes met gecomprimeerde lucht. Het effect van de opslag op de omgeving in combinatie met het rendement van de opslag zijn de hoofddoelen van deze thesis. De simulaties zijn uitgevoerd met een eindige elementen software, Lagamine, voor een 1D axi-symmetrisch thermo-hydraulisch model van 30m lang. CAES-exploitatie is gesimuleerd door dagelijkse cyclussen van 8h injecteren, 4h rusten, 4h produceren en 8h stabiliseren. De dagelijkse gemiddelde lekkage is berekend op basis van 80 cyclussen. Het rots-model toont de nood van een voering wanneer de permeabiliteit eerder hoog is ($>10^{-18}m^2$). De gevoeligheidsanalyse van het hydraulisch gevoerde model leidt tot een set van parameters die toelaten de lekkage te minimaliseren. Een basisdruk van 5.5MPa of iets lager in een holte met een zeer ondoordringbare voering ($10^{-20}m^2$) en hoge zuigkracht (1.47-14.7MPa) wordt geadviseerd. De rots parameters zijn minder belangrijk, maar een hoge zuigkracht van de rots laat toe de lekkage verder te verlagen. Injecteren tijdens de dagelijkse cyclussen gebeurt met een injectiesnelheid van $7.913 \cdot 10^{-5}kg/s$ of liefst hoger met lucht die gekoeld is tot de omgevingstemperatuur van de rots. Het thermo-hydraulisch model toont aan dat de koppeling tussen de temperatuur en de druk zwak is. Het beste rendement wordt bereikt in een grote holte op een hoge druk na het injecteren in plaats van kleinere holtes op lagere druk.

Modélisation de la performance géotechnique du stockage d'énergie par air comprimé dans le souterrain

Niels Tommelein

Vrije Universiteit Brussel
Pleinlaan 2
1050 Brussel

Master dans
Ingénieur civil option construction et géomatériaux

Niels.Tommelein@vub.ac.be

Juin 2016

Mots clés: CAES, fuite d'air, bordée caverne rocheuse, performance géotechnique, analyse thermo-hydraulique

abrégé

Le sujet de cette thèse est l'étude du comportement thermo-hydraulique du stockage d'énergie par air comprimé dans le souterrain. Les effets du stockage sur l'environnement en combinaison avec l'efficacité du stockage sont les objectifs principaux de cette thèse. Des simulations sont effectuées en Lagamine, un logiciel d'éléments finis, pour un modèle 1D axisymétrique thermo-hydraulique de 30m de long. CAES-exploitation est simulée par des cycles quotidiens de l'injection de 8h, 4h de stockage, 4h de production et 8h de stabilisation. La fuite moyenne quotidienne est déterminée sur base de 80 cycles. Le modèle hydraulique de roche a montré la nécessité d'une doublure quand la perméabilité est assez élevée ($>10^{-18}m^2$). L'analyse de sensibilité du modèle hydraulique de revêtement en béton conduit à un ensemble de paramètres optimaux qui permettent de réduire les fuites. Une pression de base de 5.5MPa ou légèrement inférieure dans une caverne avec un revêtement imperméable à haute de $10^{-20}m^2$ et une pression d'entrée d'air élevée (1.47-14.7MPa) sont conseillées. Les paramètres rocheux sont moins importants, mais une pression d'air élevée permet de réduire la fuite plus. Injection au cours des cycles quotidiens se produit à une vitesse d'injection de $7.913 \cdot 10^{-5} kg/s$ ou préférentiellement supérieur avec de l'air qui est refroidi à des températures comparable aux températures de la roche. Le modèle thermo-hydraulique a montré que le couplage entre la température et la pression est faible. L'efficacité est la meilleure pour une grande caverne à haute pression après l'injection au lieu de petites cavernes à basse pression.

Acknowledgement

I would first like to deeply thank my thesis promotor Pierre Gerard of Université Libre de Bruxelles who offered continuous guidance and advice throughout the course of this thesis. His guidance was essential to this master thesis delivery. I thank him for the excellent support on the Lagamine software as his office was always open in case of questions.

Finally, I take this opportunity to express the gratitude to my parents, grandparents, and my siblings for providing support during my years of study.

Niels Tommelein

Contents

Chapter 1	General introduction	17
1.1	Renewable energy storage	17
1.2	Objectives of the thesis	17
1.3	Description of the remaining chapters.....	18
Chapter 2	Literature review	19
2.1	Compressed air energy storage.....	19
2.2	Storage locations	20
2.2.1	Rock caverns.....	20
2.2.2	Salt domes	20
2.2.3	Aquifer	21
2.3	Operational facilities.....	22
2.4	Previous research	22
2.5	Further investigation	23
Chapter 3	Boundary value problem	25
3.1	Geometry.....	25
3.2	Initial conditions	26
3.3	Boundary conditions.....	26
3.3.1	Simulation.....	27
3.3.1.1	Excavation phase	27
3.3.1.2	Initialisation phase.....	27
3.3.1.3	Operational phase	27
3.4	Balance equations and constitutive equations	28
3.4.1	Fluid mass balance equations.....	28
3.4.2	Fluid transport constitutive equations	29
3.4.3	Equilibrium restriction laws.....	30
3.4.4	Water retention curve.....	30
3.4.5	Relative permeability.....	30
3.4.6	Thermal conductivity.....	31
3.4.7	Dynamic viscosity	31
3.5	Parameters of the model.....	31
3.5.1	Hydraulic parameters	31

3.5.2	Thermal parameters	33
3.5.3	Fluid properties	34
Chapter 4	Results.....	35
4.1	Hydraulic model.....	35
4.1.1	Injection in rock without lining.....	35
4.1.1.1	Excavation and drainage.....	35
4.1.1.2	Initialisation phase.....	35
4.1.1.3	Operational phase	36
4.1.1.4	Effect of the permeability on leakage	38
4.1.2	Injection in rock with lining	41
4.1.2.1	Reference model	41
4.1.2.1.1	<i>Excavation and drainage.....</i>	<i>41</i>
4.1.2.1.2	<i>Initialisation phase</i>	<i>41</i>
4.1.2.1.3	<i>Operational phase.....</i>	<i>42</i>
4.1.2.2	Sensitivity analysis	46
4.1.2.2.1	<i>Intrinsic permeability.....</i>	<i>46</i>
4.1.2.2.2	<i>Air entry pressure</i>	<i>48</i>
4.1.2.2.3	<i>Injection rate</i>	<i>52</i>
4.1.2.3	Leakage.....	57
4.2	Thermo-hydraulic model	58
4.2.1	Thermal reference case	58
4.2.2	Sensitivity analysis	61
4.2.2.1	Increased injection temperature.....	61
4.2.2.2	Injection temperature imposed at whole cavern.....	62
4.2.2.3	Cavern thermal conductivity	64
4.2.2.4	Adapted permeability.....	65
4.2.2.5	Air entry pressure	67
4.2.2.6	Injection rate	68
4.3	Efficiency.....	71
4.4	Perspectives on rock cracking	72
Chapter 5	Conclusion.....	73
Chapter 6	Bibliography	75
Appendix A	Unlined hydraulic model	77
Appendix B	Lined hydraulic model	78
B.1	Reference case	78

B.2	Adapted permeabilities	79
B.3	Air entry pressure	80
Appendix C	Leakage calculation	83
C.1	Unlined hydraulic model	83
C.2	Lined hydraulic model	85
C.3	Thermo-hydraulic model	88

List of figures

Figure 1 Overview of a possible layout for a CAES-facility with underground caverns. (Kim, et al., 2012)	19
Figure 2 Operation of an aquifer for natural gas storage. For CAES-applications, daily cycles are used. Thus, the summer case presented in the figure stand for the injection period and the winter case for the withdrawal of air. (Fluxys, 2012)	21
Figure 3 Cavern lay-out of the model in the case of a lined cavern with materials, dimensions and boundary conditions.	25
Figure 4 Finite element model with a concrete lining and variable mesh.....	26
Figure 5 Injection rate during a daily cycle.....	28
Figure 6 Water retention curve by the Van Genuchten equation for the lining/rock and the cavern.	32
Figure 7 Relative permeability for water and air depending on the degree of saturation.	33
Figure 8 Water pressure distribution in the rock during the excavation phase of a rock with an intrinsic permeability of 10-18m ² for different time periods in order to find a steady-state solution.	35
Figure 9 Water and air pressure distribution after the initialisation phase and zoom on the first meter in the rock.....	36
Figure 10 Horizontal air pressure profile for different cycle during CAES-operation after the last waiting period in the cycle.	36
Figure 11 Horizontal water pressure profile for different cycles during CAES-operation after the last waiting period in the cycle.	37
Figure 12 Horizontal degree of saturation profile for different cycles during CAES-operation after the end of the last waiting period in the cycle.	37
Figure 13 Horizontal water pressure profile for different rock permeabilities after drainage.	39
Figure 14 Cavern pressure evolution during CAES-operation for different intrinsic permeabilities.	39
Figure 15 Horizontal air pressure profile at the end of cycle 81 for different rock permeabilities and the water profile for the highest permeability.....	40
Figure 16 Water pressure after the initialisation phase with at the concrete lining an imposed value related to the suction at a saturation of 70% (H).....	41
Figure 17 Evolution of the cavern pressure at the end of the initialisation phase (H).	41
Figure 18 Degree of saturation after initialisation phase with the lining clearly still at 70% (H).....	42
Figure 19 Water and air pressure after the initialisation phase when a concrete lining separates the cavern from the rock (H).....	42
Figure 20 Evolution of the cavern pressure during one operational cycle for different cycles (H).	43
Figure 21 Air pressure profile at different stages of the 1 st cycle (H).	43
Figure 22 Evolution of the cavern air pressure during the CAES-operational cycles at the end of each cycle (H).	43
Figure 23 Transition of the air pressure throughout the rock at the end of CAES-operational cycles (left) and evolution of the degree of saturation with increasing number of CAES-cycles showing the situation at the end of the cycle (right) (H).	44
Figure 24 Migration of the air pressure front in the surroundings of the cavern, situation at the end of the cycle (H).	45
Figure 25 Evolution of the water pressure at the end of CAES-operational cycles (H).	45
Figure 26 Longitudinal air pressure profile for adapted permeability after the initialisation phase (H).	46
Figure 27 Longitudinal water pressure profile for adapted permeability after initialisation (H).....	47
Figure 28 Cavern pressure evolution during CAES-operation at the end of each cycle with adapted permeability (H).	47
Figure 29 Longitudinal air pressure profile during CAES-operation with adapted permeability at the end of cycle 81.....	47
Figure 30 Longitudinal water pressure profile at the end of cycle 81 for the adapted permeability (H).	48
Figure 31 Horizontal degree of saturation profile for different air entry pressures after initialisation (H).....	48
Figure 32 Air pressure in cavern during the initialisation phase for different air entry pressures (H).	49
Figure 33 Horizontal air pressure profile after initialisation for different air entry pressure (H).	49
Figure 34 Horizontal water pressure profile for different air entry pressures after initialisation (H).	50
Figure 35 Cavern pressure evolution during CAES-operation for different air entry pressures at the end of each cycle (H). .	50
Figure 36 Horizontal air pressure profile at the end of cycle 81 for different air entry pressures (H).	51
Figure 37 Horizontal water pressure profile at the end of cycle 81 for different air entry pressures (H).	51
Figure 38 Horizontal degree of saturation profile at end of cycle 81 for different air entry pressures (H).....	52
Figure 39 Cavern pressure evolution during the operational phase for different injection rates (H).	53
Figure 40 Longitudinal air pressure profile in the operational phase for different injection rates at the end of cycle 81 (H). .	53
Figure 41 Longitudinal water pressure profile in the operational phase for different injection rates at the end of cycle 81 (H).	54
Figure 42 Cavern air pressure evolution during initialisation for different global injection rates(H).....	54
Figure 43 Horizontal water pressure profile after initialisation for different global injection rates (H).....	55

Figure 44 Evolution of the cavern pressure during CAES-operation for different global injection rates at the end of each cycle (H).....	56
Figure 45 Horizontal air pressure profile at the end of cycle 81 for different global injection rates (H).....	56
Figure 46 Horizontal water pressure profile at the end of cycle 81 for different global injection rates (H).....	57
Figure 47 Cavern air pressure envelop for the first cycle of the hydraulic and thermal case (TH).....	58
Figure 48 Temperature evolution in the cavern for the first thermal cycle at the cavern side and cavern middle (TH).....	59
Figure 49 Horizontal temperature profile during CAES-operation for different cycles in end-state (TH).	60
Figure 50 Cavern pressure evolution at the end of each cycle during CAES-operation (TH).....	60
Figure 51 Horizontal air pressure profile during CAES-operation for different cycles end-state (TH).....	60
Figure 52 Horizontal water pressure profile during CAES-operation for different cycles end-state (TH).	60
Figure 53 Horizontal degree of saturation profile during CAES-operation for different cycles end-state (TH).....	60
Figure 54 Horizontal temperature profile during CAES-operation at the end of cycle 81 for different injection temperatures (TH).....	61
Figure 55 Cavern pressure evolution at the end of each cycle during CAES-operation for different injection temperatures (TH).....	62
Figure 56 Horizontal air pressure profile during CAES-operation at the end of cycle 81 for different injection temperatures (TH).....	62
Figure 57 Horizontal water pressure profile during CAES-operation at the end of cycle 81 for different injection temperatures (TH).....	62
Figure 58 Horizontal degree of saturation profile during CAES-operation at the end of cycle 81 for different injection temperatures (TH).....	62
Figure 59 Horizontal temperature profile during CAES-operation at the end of cycle 81 for different injection modes (TH).	63
Figure 60 Cavern pressure evolution at the end of each cycle during CAES-operation for different injection modes (TH).....	63
Figure 61 Horizontal air pressure profile during CAES-operation at the end of cycle 81 for different injection modes (TH). .	63
Figure 62 Horizontal water pressure profile during CAES-operation at the end of cycle 81 for different injection modes (TH).	63
Figure 63 Horizontal degree of saturation profile during CAES-operation at the end of cycle 81 for different injection modes (TH).....	63
Figure 64 Horizontal temperature profile during CAES-operation at the end of cycle 81 for different thermal conductivities of the cavern (TH).....	64
Figure 65 Cavern pressure evolution at the end of each cycle during CAES-operation for different thermal conductivities of the cavern (TH).....	65
Figure 66 Horizontal air pressure profile during CAES-operation at the end of cycle 81 for different thermal conductivities of the cavern (TH).....	65
Figure 67 Horizontal water pressure profile during CAES-operation at the end of cycle 81 for different thermal conductivities of the cavern (TH).....	65
Figure 68 Horizontal degree of saturation profile during CAES-operation at the end of cycle 81 for different thermal conductivities of the cavern (TH).	65
Figure 69 Horizontal temperature profile during CAES-operation at the end of cycle 81 for different permeability configurations (TH).....	66
Figure 70 Cavern pressure evolution at the end of each cycle during CAES-operation for different permeability configurations (TH).....	66
Figure 71 Horizontal air pressure profile during CAES-operation at the end of cycle 81 for different permeability configurations (TH).....	66
Figure 72 Horizontal water pressure profile during CAES-operation at the end of cycle 81 for different permeability configurations (TH).....	66
Figure 73 Horizontal degree of saturation profile during CAES-operation at the end of cycle 81 for different permeability configurations (TH).....	66
Figure 74 Horizontal temperature profile during CAES-operation at the end of cycle 81 for different air entry pressures (TH).	67
Figure 75 Cavern pressure evolution at the end of each cycle during CAES-operation for different air entry pressures (TH).	68
Figure 76 Horizontal air pressure profile during CAES-operation at the end of cycle 81 for different air entry pressures (TH).	68
Figure 77 Horizontal water pressure profile during CAES-operation at the end of cycle 81 for different air entry pressures (TH).....	68
Figure 78 Horizontal degree of saturation profile during CAES-operation at the end of cycle 81 for different air entry pressures (TH).	68
Figure 79 Horizontal temperature profile during CAES-operation at the end of cycle 81 for operational injection rates (TH).	69

Figure 80 Cavern pressure evolution at the end of each cycle during CAES-operation for operational injection rates (TH)...	69
Figure 81 Horizontal air pressure profile during CAES-operation at the end of cycle 81 for operational injection rates (TH).	69
Figure 82 Horizontal water pressure profile during CAES-operation at the end of cycle 81 for operational injection rates (TH).....	69
Figure 83 Horizontal degree of saturation profile during CAES-operation at the end of cycle 81 for operational injection rates (TH).....	69
Figure 84 Horizontal temperature profile during CAES-operation at the end of cycle 81 for global injection rates (TH).	70
Figure 85 Cavern pressure evolution at the end of each cycle during CAES-operation for global injection rates (TH).....	70
Figure 86 Horizontal air pressure profile during CAES-operation at the end of cycle 81 for global injection rates (TH).....	70
Figure 87 Horizontal water pressure profile during CAES-operation at the end of cycle 81 for global injection rates (TH).	70
Figure 88 Horizontal degree of saturation profile during CAES-operation at the end of cycle 81 for global injection rates (TH).	70
Figure 89 Horizontal profile of the degree of saturation at the end of cycle 81 for different permeabilities for the unlined hydraulic model.....	77
Figure 90 Full horizontal air pressure profile for the reference concrete case (H).....	78
Figure 91 Full horizontal water pressure profile for the reference concrete case (H).	78
Figure 92 Horizontal water pressure profile for the sensitivity analysis with adapted intrinsic permeability after the excavation stage (H).	79
Figure 93 Horizontal profile of degree of saturation for the adapted permeability sensitivity analysis during CAES-operation (H).....	79
Figure 94 Horizontal profile of degree of saturation for operational air entry pressure sensitivity analysis during CAES-operation (H).	80
Figure 95 Horizontal profile of degree of saturation for global air entry pressure sensitivity analysis after initialisation (H).	80
Figure 96 Full horizontal air pressure profile at the end of cycle 81 during CAES-operation for different global injection rate (H).....	81
Figure 97 Full horizontal water pressure profile at the end of cycle 81 during CAES-operation for different global injection rate (H).	81
Figure 98 Horizontal profile of degree of saturation for operational air entry pressure sensitivity analysis during CAES-operation (H).	82
Figure 99 Full horizontal water pressure profile for different air entry pressures (H).	82

List of tables

Table 1 Material properties used as base for modelling the underground cavern.	31
Table 2 Thermal parameters used as base case for modelling of the thermal aspect of CAES-operation in a lined cavern.	33
Table 3 Parameters for water and air for modelling the underground cavern.	34
Table 4 Leakage rate and leakage for different permeabilities based on 80 cycles	40
Table 5 Intrinsic permeabilities for the hydraulic lined reference model.	41
Table 6 Leakage for all hydraulic simulations.	57
Table 7 Cavern thermal conductivity sensitivity analysis: changed parameter.	64
Table 8 Overview of leakage percentage based on the mean daily air mass loss for all simulated cases in the hydraulic and thermo-hydraulic model with the difference between both.	71

Chapter 1 General introduction

This Master Thesis studies the (thermo)hydraulic behaviour of an underground cavern used for compressed air storage as energy storing facility. The main focus of the thesis lies on the effects caused by CAES-operation on the surrounding rock and the installed lining. This is directly related to the leakage of air out of the cavern, so the efficiency of operation. The introduction starts with a general problem statement in the energy world, followed by the objective of this thesis and a description of the general content.

1.1 Renewable energy storage

Energy has become indispensable in our world. The risks and consequences with energy shortage and the related power outage are huge, in particular for the economy. Energy load levelling is therefore a main principle in the energy sector. The balance between supply and demand is a crucial element for the stability of the power grid. The transition to more sustainable energy production methods, like solar and wind, puts this principle under pressure. Fact is that most renewable energy sources are non-demand-oriented. The fluctuating energy production may cause problems for the power grid. Off-shore turbines need to transmit their energy to locations on land where the energy is needed. This generally high distance causes high transmission costs as the power cable also have to be able to transmit all the energy at peak production moments. In the current energy production world, thermal power stations and gas turbines are often used to balance supply/demand, on a less efficient manner (Bullough, et al., 2004).

In order to cope with those fluctuations, storing energy is the promising solution. Classical storage on batteries, fuel cells and supercapacitors are not cost-efficient at large scale. At large scale, like for wind energy, pumped hydroelectric energy storage can be a promising solution. However, this method asks for the presence of water and useful topography. It is a quite effective storage solution with a conversion efficiency of 65-80% but it has some important geological limitations (Ibrahim, et al., 2008).

Another storage solution that has the same kind of effectiveness but that is more flexible in implementation, is compressed air energy storage. This kind of storage adds an additional part in the production process of a gas turbine in order to shift the compression process in time, as this can take up to two-thirds of the natural gas used in a gas turbine. CAES efficiency is between 66% and 82% (Rutqvist, et al., 2012). By compressing the air in advance, when energy is available from renewable resources during off-peak hours, a higher efficiency of the gas turbine can be obtained. During peak hours, when the air is retrieved from the cavern, up to three times the power can be produced with the same amount of fuel consumption (Ibrahim, et al., 2008). The exact process is described in Literature review.

1.2 Objectives of the thesis

The objective of this thesis is to extent the knowledge that is already present in the field of CAES. However as is showed in Literature review, research often focuses on the thermo-mechanical analysis. For this reason, the investigation in this thesis focuses on providing additional insights in the thermo-hydraulic analysis in combination with air leakage. Together with a sensitivity analysis, this allows to define a set of parameters that are preferential for an efficient operation with limited air leakage.

1.3 Description of the remaining chapters

The thesis exists of three main chapters.

In Chapter 2, a literature review is presented. The concept of compressed air energy storage is further highlighted. The different options/locations as storage space are summed up, followed by a presentation of the operational facilities based in different regions. Next, the results and conclusions from previous researches are presented. Finally, the value of the thesis to the field of study is justified.

In Chapter 3, the boundary value problem is treated. First, a general overview of the geometry of the installation is given. Followed by the initial and boundary conditions that are related to the location of the cavern. The used software is briefly explained together with the model and its equations. The translation of the operational process to simulation phases guarantees the right base to start operations. The chapter finished with all other parameters.

Chapter 4 presents the results of all numerical simulations. The need of a lining system is first shown for an unlined, hydraulic model. Followed by the simulations of a realistic cavern layout, a reference case is fixed and a sensitivity analysis is performed on a set of important parameters for the hydraulic model. Afterwards the same is done for the thermo-hydraulic model with an extended sensitivity analysis for the thermal parameters. Finally, the chapter is concluded with the efficiency of operation determined by the mean daily leakage. This allows to answer all the questions and to determine the best set of parameters and conditions.

Chapter 5 concludes this thesis and gives a brief overview of the most important results and conclusions obtained from the thermo-hydraulic simulations. Again the best set of parameters and conditions is mentioned.

Chapter 2 Literature review

This chapter contains a literature review. The problem of energy storage and possible solutions are described before. The principle of CAES is explained beneath, followed by an overview of the storage location, the operational compressed air energy storage systems in the world and research done in this field. The chapter is ended with what this thesis can mean for the field of research.

2.1 Compressed air energy storage

As mentioned in General introduction, CAES is an energy storage solution that is used in combination with a gas turbine to produce power. In a gas turbine, a large part of the fuel is used to compress the combustion air (Ibrahim, et al., 2008). It is possible to compress air before and use it later. This forms the principle of CAES.

During off-peak hours, the excess of electricity is used to compress air. As the air heats up during compression, it has to be cooled down to more ambient temperature by an intercooler or other kind of heat exchanger. The compressed air is stored in the cavern until the peak-hours to meet the large demand of electricity (Figure 1). The compressed air is then heated and lead into the combustor and turbine of a modified gas turbine. This system of energy storage can be used to flatten the load demand curve and provides the ability for thermal power plants to produce constant at maximum efficiency as overproduction can be stored temporarily. Compressed air energy storage is a technique that is implemented for short term use. Daily cycles are possible, but also longer injection periods in weekends can be used to top up the storage space.



Figure 1 Overview of a possible layout for a CAES-facility with underground caverns. (Kim, et al., 2012)

After installation of the cavern, it is pressurised to a certain base pressure, which is called the initialisation phase. This base pressure is responsible for an easier injection and withdrawal of air during operation. As it is possible that some of the air migrates into the lining and rock, it would not be possible to withdraw the same amount of air as injected. This base pressure is mostly needed to get the air out without much equipment as the pressure should ideally never go below the base pressure. However, in the case of small leakage this base pressure is able to compensate slight losses of air mass. This unfortunately leads to a lowering of the base pressure.

Generally, there is a difference between diabatic and adiabatic CAES. The diabatic CAES concept, is in fact explained above. The compressed air is cooled and stored and afterwards during withdrawal reheated before adding it in the modified gas turbine. This cooling and reheating has a slightly negative effect on the efficiency (Bullough, et al., 2004). Thermodynamically there will be a heat exchange between the cavern air and the environment (Xia, et al., 2015).

The adiabatic CAES concept is going to extract the heat from the compressed air and store it in a thermal energy storage. The thermal energy storage can be cast iron, ceramics, natural stone, oil, ... When withdrawing air, this heat can be reused to heat the air from the cavern before it enters the gas turbine. This adiabatic process leads to higher efficiencies and less emissions of greenhouse gasses in the overall process (Bullough, et al., 2004). However, the heat does not have to be stored, it can also be used to heat water in residential areas. This latter is also applicable on the diabatic CAES concept. With heat exchangers it is possible to reuse the heat waste on an environmental friendly way.

2.2 Storage locations

The storage of compressed air can take place in a lot of caverns that are naturally present or that were artificially made.

2.2.1 Rock caverns

There exist two types of rock caverns. The unlined rock cavern (ULR) which is often located at higher depths, stores the gas due to a higher groundwater pressure in the cavern rock. In this case it is important that the water pressure is higher than the maximal air pressure in the cavern. If this is not the case, the permeability of the rock might be able to limit the leakage in combination with the present water pressure. A lined rock cavern (LRC) is more flexible. Leakage is prevented by a thin steel lining which acts as a complete sealing and does not supply load. The forces due to the gas pressure are transferred to the rock by an at least 2m concrete wall, in the case of large (15-20m) diameter caverns, which is located in between the steel lining and the rock (Zlender, et al., 2013).

LRC are located at depths of 100 to 300m. The minimum design life time is 500 cycles. During operation there exists several failure risks. Failure of the rock mass, uplift of the cavern top, instabilities when placed in group, unequal deformations causing leakage by fracturing the steel lining (Zlender, et al., 2013). At a depth of 100m, a typical operating pressure is 5 to 8MPa, which is supported by the surrounding rock. This technique is advantageous due to its lower depth and thus lower construction costs. The site selection can occur more flexible and close to existing transmission grids.

2.2.2 Salt domes

Salt domes are commonly used for underground storage as they have low porosities, near-zero permeabilities in the undisturbed rock, high ductility, a healing capacity and a high thermal conductivity (Martin, et al., 2015). The domes are constructed in salt rock which are present in specific regions. Often the method of solution mining is used. By this water is injected at the wanted cavern location. The salt will dissolve with the water and form brine which is removed from the cavern and

can be used industrially. In China, the caverns created due to the brine production were later used for underground storage (Kim, et al., 2012).

Stability is assured if a minimum operating pressure is maintained. This has to counteract the stress concentration created by making the cavern. Depending on the design, instabilities can be avoided by releasing these additional stresses. A typical shape of a salt dome is a pear or cone shaped structure. The upper structure of the cavern is typically a pressure arch. If not present, big displacements or partial collapse will lead to this self-stable structure. High cohesion and friction angle are positive for the stability. Thus, geomechanical parameters play major role in the design of salt domes. In (Wang, et al., 2013) the safety factor on the lower structure was almost linearly dependent on those parameters.

Generally, a higher operating pressure is advantageous for several reasons. It counteracts partially some in situ stresses in the rock salt. This directly leads to a reduction of the creep rate. Due to the outside ground pressure, the cavern undergoes a volume shrinkage over its working life. However, if the use at minimum operation pressure can be minimized in time, the volume shrinkage lowers exponentially. This leads to a longer life expectancy of the salt cavern. A typical design service lifetime is 30 years (Yang et al 2015). To ensure a minimum operating pressure, the base pressure, a cushion gas, often just air, is needed which is about $\frac{1}{3}$ to $\frac{1}{2}$ of the total storage space.

2.2.3 Aquifer

An aquifer used for storage is a confined aquifer. Typically, it exists of a cap rock which is impermeable. It forms the sealing of a porous rock which is filled with water. The aquifer has to be transformed minimally to be 'activated'. Mainly by the construction of the operating shaft going through the cover layer.

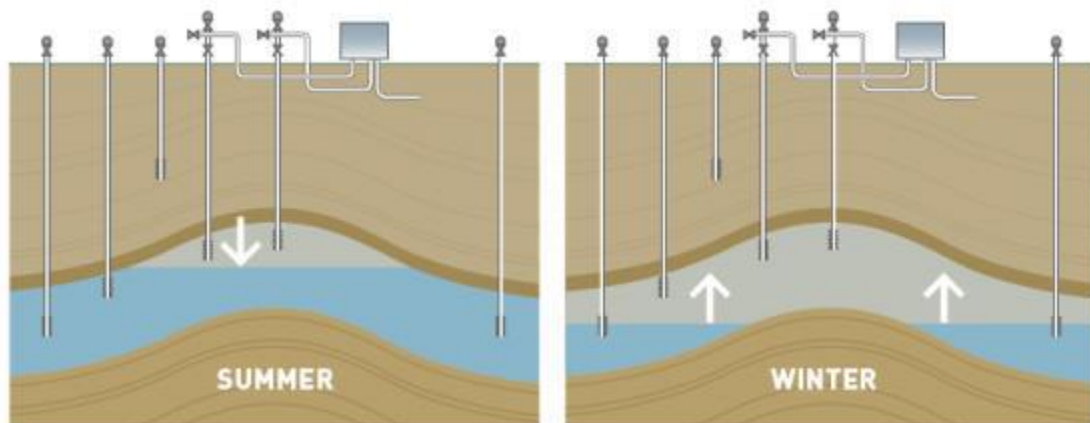


Figure 2 Operation of an aquifer for natural gas storage. For CAES-applications, daily cycles are used. Thus, the summer case presented in the figure stand for the injection period and the winter case for the withdrawal of air. (Fluxys, 2012)

The injection of gas has to happen under a pressure that is higher than the water pressure in the aquifer, but has to be limited to prevent failing by lifting the overburden or the creation of fractures (Wyllie, 1965). During the injection, the underground water table lowers due to the pressure of the natural gas. Withdrawal of the gas causes a rise in the water table. To assure that the withdrawal pressure and flow level is adequate, a cushion gas, often air, is needed. This volume of gas is permanently present in the aquifer to reassures a consistent pressure and flow. It can take up to 50% of the total volume of the aquifer. Some of this cushion gas is permanently trapped in the porous rock. A big disadvantage of aquifers is the fact it is an expensive solution. Mostly the structural description

and gas tightness of the cap rock is not well known. Thus, a thorough investigation should be done (British Geological Survey, 2015).

2.3 Operational facilities

CAES is a technique that is known for a long time and is still under development. In the world there are some real-scale CAES-plants. Mostly they were created for experimental use, after which they also were converted for commercial activities. However, these plants are of medium size.

In 1978 the first CAES-facility was built in Huntorf, Germany in a salt rock. It was created by solution mining. The two caverns are located at a depth of 600m which can guarantee a stability for months of storing. The maximum operating pressure is about 10 MPa (Kim, et al., 2012). The Huntorf facility is able to store 310 000m³ of compressed air. The diabatic CAES-facility was able to produce 290MW of electricity. Improvements in the last decade, like a waste-heat recovery system was installed to increase its overall efficiency. Due to this, it is able to produce 321MW with the same amount of fuel (Xia, et al., 2015).

A second facility is located in McIntosh, Alabama in rock salt. It is in commercial operation since 1991. The underground cavern, located at 450m, provides a 500 000m³ storage volume. In this plant the pressure varies between 4.5MPa and 7.4MPa. It is able to provide 110MW (Kim, et al., 2012).

For research purposes, Japan had two facilities located at 200m and 500m in a crystalline rock. They were caverns as described in Rock caverns with the deeper one unlined, and the other was an old lined mine cavern (Kim, et al., 2012).

For the future new facilities are planned/investigated. Ohio is planning to create a very large-scale CAES-facility of 2700MW in a converted limestone mine located at 670m depth. The low permeable host rock is responsible for the air tightness at operation pressures between 6 and 11MPa. Aquifer CAES is in the early stage of development in the American continent for their wind farms (Rutqvist, et al., 2012).

2.4 Previous research

This chapter makes a summary of prior research that was done in the field of CAES.

(Kim, et al., 2012) explored the possibilities of lined caverns at shallow depth. Main issue was providing sufficient air tightness. This could be obtained by having a low permeability of the concrete lining and the surrounding rock. During cycles the cavern pressure varied between 4MPa and 8MPa. A lining permeability of less than 10⁻¹⁸m² lead to an air leakage rate of less 1%. They also observed the important influence of the retention properties on the air leakage. For impermeable linings, the heat loss was observed mostly due to heat conduction. This heat loss could be minimized by lowering the injected air temperature to the ambient temperature of the rock. By this, the leaked heat into the rock during injection and storing could be retracted for the main part during withdrawal of air.

(Rutqvist, et al., 2012) investigated the thermodynamic and geomechanical performance of a shallow concrete-lined CAES-cavern. This was the same cavern as in (Kim, et al., 2012). The operational pressure was 5 to 8MPa. Thermodynamic analysis showed a 3.3% energy loss due to heat conduction. The geomechanical performance had a focus on the stresses in the concrete lining. The observed maximal tensile stress in the concrete was 8MPa due to a pressurized cavern. The thermal stresses are smaller and compressive. The application of a synthetic seal (rubber or steel) on the inside of the cavern reduced the tensile stresses in the concrete to 5MPa. For one compression, a loss of air mass of 0.16% was observed.

(Kim, et al., 2013) investigated the effect of the excavation damaged zone and stability of a lined rock cavern. This investigation leads to the conclusion that the excavation damaged zone should be limited as much as possible for purposes of tensile cracks and air leakage. Next to this, a favourable design for stability purposes was proposed. The cavern should be equipped with a compliant, internal sealed, concrete lining in a stiff host rock with extreme care during construction of the cavern.

(Xia, et al., 2015) investigated the temperature and pressure variation in CAES-caverns with a diabatic analytical solution. The solution is based on two assumptions. The cavern air density, which is approached by an average value, and the cavern wall temperature are constant.

(Mohanto, et al., 2014) studied the cyclic thermo-mechanical analysis of a horizontal wellbore. The simulated cavern has a steel lining directly in contact with the rock. The main focus of the investigation was on the mechanical effects. The influence of different mechanical parameters, like dilation angle, friction angle, Poisson's coefficient, loading frequency and temperature cycles, was studied. The observation was that when introducing the thermal aspect of the simulation, the plastic strains increased with 33%. It also shows that the mechanical parameters of the rock play an important role as a weak sandstone has 700% higher displacements than in granite. The conclusion to limit the displacements in the rock were a low dilation angle, high friction angle and a high stress ratio.

(McGrail, et al., 2013) investigated the use of more permeable and porous rock structures like basalt deposits instead of salt caverns to go around geological constraints. At Columbia Hills a CAES-plant is designed to take 231MW of load for storage and will regenerate 207MW. The storage is designed to have a 40 days' continuous storage capacity which results in 400 hours of regeneration. A basalt deposit has a quite high permeability and is perfect for storage if there is an overlying rock present with a low permeability.

2.5 Further investigation

As Previous research showed, the main investigations happened on the thermo-mechanical behaviour of CAES-operation. However, the hydraulic aspect has also a major influence in the cavern at shallow depth. As the ambient hydrostatic water pressure is often not sufficient to prevent air leakage, an important interaction between water and air pressures can be expected.

This thesis therefore focuses on the thermo-hydraulic analysis of the surrounding of a CAES-cavern. The mechanical parameters like stress and deformations are not studied. For this reasons the displacements are imposed to be fixed. The numerical analysis is performed with the finite element software Lagamine.

The previous research of Kim and Rutqvist forms a decent basis to start with. This is why the modelled cavern is partially bases on these research papers. Some important parameters are derived from those papers as they are reliable values that are in some cases also linked to the real-life operational caverns.

The thermo-hydraulic simulation is performed for a reference case, that is described in the Boundary value problem. But as Mohanto did a mechanical parametric study, this is here done for hydraulic and thermal parameters. This parametric study allows to define the best conditions where CAES-caverns should be located and how they should be operated to have a maximal efficiency of the storage process, thus a limited air leakage. However, as is mentioned throughout this document, the efficiency of the air storage can affect the overall efficiency of the power plant that includes all processes from renewable production to the transfer to the grid. As always an equilibrium has to be found.

Chapter 3 Boundary value problem

This chapter includes all aspects of the boundary value problem. The geometry of the plant is based on references and research papers as mentioned in Further investigation.

The thermo-hydraulic simulation is performed in an underground cavern at shallow depth located in a sedimentary claystone. The cavern is considered as a porous medium. Both unlined and lined caverns are studied to show the need of the lining. This kind of cavern has less geological restrictions than the salt caverns and could be possible, if the rock is mechanically sufficient, in the claystone found in West-Europe.

The thermo-hydraulic model with all its parameters regarding geometry, hydraulic behaviour, thermal behaviour and others are addressed. Of course multiple possibilities exist. In order to make a relevant choice some parameters are taken equal to the ones in the research of (Kim, et al., 2012) and (Rutqvist, et al., 2012).

3.1 Geometry

The geometrical parameters are important for the analysis and the problem type. As prior researches of Rutqvist and Kim (Kim, et al., 2012; Rutqvist, et al., 2012) provide a decent modelling and a realistic model, the cavern geometry is partially based on those papers.

A choice was made to simulate a cylindrical, tubular underground cavern. In real-scale facilities, multiple caverns are present. This allows for a 1D-axisymmetric model that can be of any length, as simulation can be done per unit meter of cavern. This choice is justified by the real-scale facilities that are built by this principle. A different possibility exists in spherical caverns, however, in reality this option is less effective for large scale solutions for size and stability reasons.

Based on prior research (Rutqvist, et al., 2012) a tubular cavern with an inner diameter of 5m is modelled in an axisymmetric model. The center of the cavern is located at a depth of 100m. The simulated part of the surrounding rock has a horizontal extent up to 30m from the cavern center. The concrete lining system has a thickness of 0.5m, which proved to be a good value in earlier research (Kim, et al., 2012). Figure 3 shows the simulated cavern with the different types of materials encountered and the boundary conditions imposed.

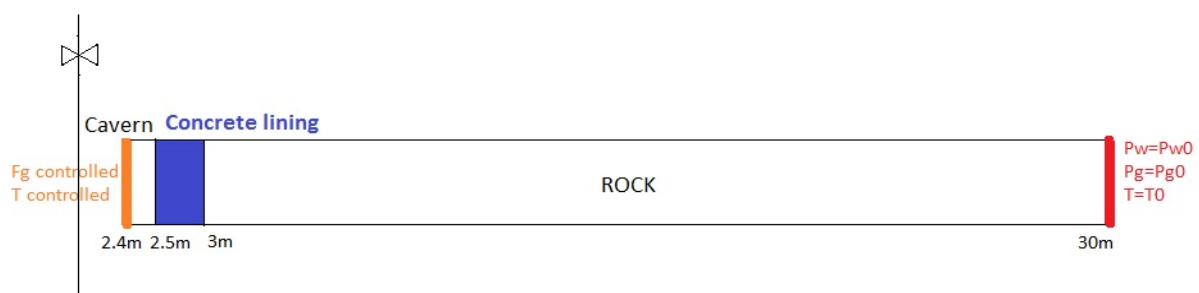


Figure 3 Cavern lay-out of the model in the case of a lined cavern with materials, dimensions and boundary conditions.

The 1D-axisymmetric model consists of one row of elements with unit height as the interest lies in the horizontal influence of CAES-operation. The cavern is simulated as a single element. In this approach, for numerical reasons, the cavern element is modelled for only a certain thickness, 10cm. A smaller cavern is used to prevent any numerical problems; like oscillations and non-physical results due to inhomogeneous pressures induced by the permeability gradient between the cavern and the lining. The small cavern should provide more uniform properties, like what is observed in the real-scale

experiments. As the volume of the cavern is reduced, the injection rate is reduced according to the volume ratio.

The finite element model is meshed with a variable mesh that has different sizes (Figure 4). Generally, three sets of mesh dimensions are used for the rock elements. A closely spaced mesh near the cavern for a detailed analysis and a coarser mesh at the extremities as the effects there should be minimal.

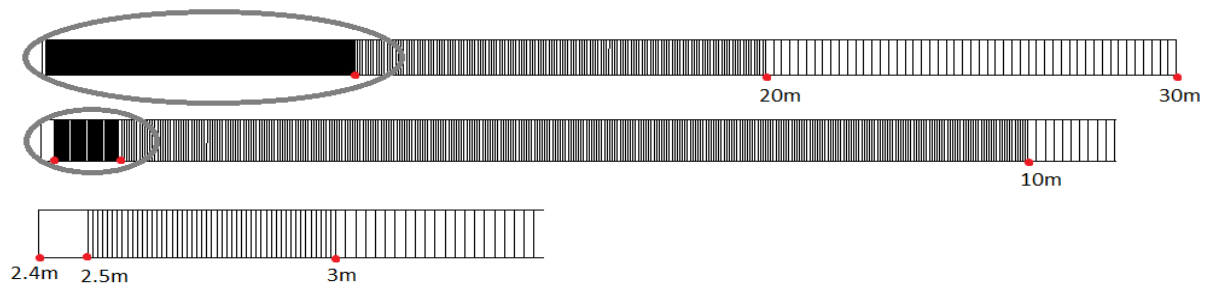


Figure 4 Finite element model with a concrete lining and variable mesh.

3.2 Initial conditions

The initial conditions of the simulation are partially related to the geometry. As the cavern is located at a depth of 100m, the water pressure and temperature can be deduced. Assuming a water table at the surface, an initial water pressure of 1MPa is considered. The rock is assumed to be initially saturated. The temperature is calculated based on a surface temperature of 10°C and a vertical temperature gradient of 0.03°C/m (Kim, et al., 2012). This leads to an initial temperature of 13°C that is set uniform to all elements of the cavern and its surroundings. The initial air pressure is set at the atmospheric pressure of 0.1MPa. A concrete lining is installed with an initial degree of saturation of 70%. This should allow an easier migration of air in the lining.

3.3 Boundary conditions

As the simulation is performed for different underground lay-outs, it is important to set some points and limits to be able to compare data between lay-outs.

- **The outer bound (x=30m) is assumed to stay at all times at constant initial water and gas pressures and at constant initial temperature.**
- The tubular cavern is assumed to have a constant volume and thus diameter of 5m.
- When linings are applied, they are located on the outside of the cavern.
- After excavation, a drain is imposed to lower the water pressure in the rock. This drain is installed at a distance of the cavern center of 2.5m for an unlined cavern and 3m for a lined cavern.
- Air is injected, not in the center, but at the inner boundary of the cavern elements. The injection rate is adapted accordingly.
- For thermal problems, the temperature is imposed on the edge of the cavern during injection periods. The heat is transferred through the system by both conduction and convection.

One of the main important parameters is the air injection rate. The applied injection rate of the model is $7.913 \cdot 10^{-5}$ kg/s. This injection rate corresponds to a 0.0198 kg/s per meter of cavern for a full model. In comparison, in previous researches, 0.022kg/s (Rutqvist, et al., 2012) was used.

One of the most important thermal parameters is temperature of the injected air. The simulated CAES-operation is a diabatic storage. Based on earlier research (Rutqvist, et al., 2012) the air temperature

during injection is set at 21°C. However, as air is heating up during compression, the air should be cooled down to 21°C before injection in the cavern. This can be done with intercooler or other types of heat exchangers. Depending on the used solution, it is possible to use this waste heat for other purposes like heating water to limit the energy waste. This temperature is directly imposed on the extremity of the cavern during the injection phase.

3.3.1 Simulation

This subchapter explains the different steps which are modelled. In short, three stages are present with their proper boundary conditions:

- Excavation phase
- Initialisation phase
- Operational phase

3.3.1.1 Excavation phase

The first major step is preparing the model. In the excavation stage, which can also be used to make the cavern, install a lining, a seal or technical equipment, a drain is imposed at the end of the lining (or cavern in the unlined case). The main purpose of this step is to reduce the water pressure in the cavern to atmospheric pressure. This creates a varying water pressure throughout the model that corresponds to the water pressure in the rock mass when injection starts. The decrease from 1MPa to 0.1MPa happens in ten seconds. This is maintained for 30 days. After these 30 days, the lining/seal is installed instantly for the lined cavern. This approach is justified as only the final situation before injection is of importance to start the actual simulations for this thesis.

The following boundary conditions are specific to the excavation phase:

- Temperature T is kept constant
- Water pressure $P_w=0.1\text{MPa}$ after 10s with a linear decrease and then maintained constant at the $x=3\text{m}$ for a lined cavern (2.5m if unlined)
- Gas pressure P_a is constant at the initial gas pressure (0.1MPa)

3.3.1.2 Initialisation phase

The second major phase exists in bringing the cavern to a certain base pressure on which it operates. This pressure is needed to have a certain efficiency. If the base pressure would be the atmospheric pressure it would be difficult to extract all the air that was pumped in as some of the air is trapped in porosities in the lining/rock. The main goal of this phase is to facilitate the operational phase. The base pressure pushes the air injected at the operational phase out of the cavern at sufficient high pressures to use directly in the modified gas turbine. The air pressure in the cavern is brought up during one full day of injection.

The following boundary conditions are specific to the initialisation phase:

- Temperature T is kept constant
- Water pressure P_w is free
- Air pressure P_a is free
- Air flow F_g is constant at the cavern wall during 24h at the injection rate ($7.913 \cdot 10^{-5}\text{kg/s}$)

3.3.1.3 Operational phase

The third phase is the most important phase where the real compressed air energy storage happens. In this model daily cycles are chosen. However, depending on the problem it is possible to have different durations, injection/withdrawal rates etc. The fact that daily cycles seem logic, as at night

there is a potential overcapacity of energy and during the day this is not the case in general, justifies this choice.

A 24h cycle starts with 8h of injection followed by 4h of storing. After this, energy is produced during 4h by air withdrawal at twice the rate of injection. To finish the cycle, the cavern will rest 8h (Rutqvist, et al., 2012). Figure 5 shows the imposed injection rate during a full daily cycle.

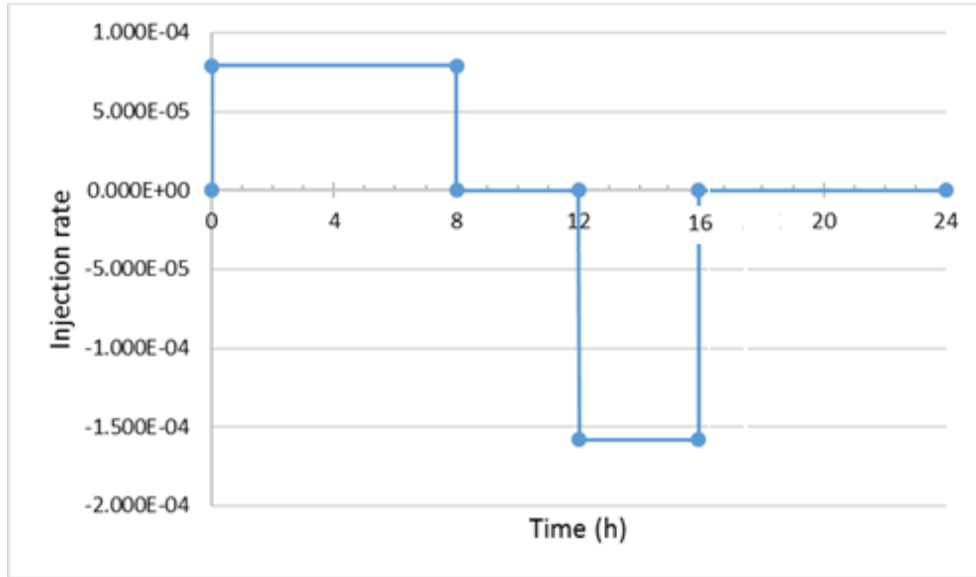


Figure 5 Injection rate during a daily cycle.

As the same amount of air is injected and extracted, the volume of air that is recoverable should always be available. If the base pressure in the cavern would be too low, pumps can be used to extract the air out of the cavern. This however has a negative influence on the overall efficiency of the energy plant. To prevent this, the base pressure can be used as a 'back-up' reservoir to cover leakage of air and guarantee the conservation of mass that comes in and goes out during a cycle.

3.4 Balance equations and constitutive equations

A 1D thermo-hydraulic axisymmetric model with unsaturated conditions is built based on the geometry specified above. In the porous medium two fluids are encountered: water and air but air dissolved in water and water vapour are also present. All simulations are executed with Lagamine finite element software developed at the University of Liège. The software was first developed at the end of the 70's but has been developed further over the years. The code is able to perform non-linear constitutive modelling, multi-physics, ... in the field of metal forming and environmental geotechnics. In the following, the equations of the model are discussed.

3.4.1 Fluid mass balance equations

In the model two chemical species are present: water and air. The fluid mass balance equations are defined for both of them (Charlier, et al., 2013). The water mass balance equation is given by:

$$\text{div}(\underline{f}_w) + \frac{\partial}{\partial t}(\rho_w \phi S_{rw})_w + \text{div}(\underline{f}_v) + \frac{\partial}{\partial t}(\rho_v \phi (1 - S_{rw})) - Q_w = 0$$

Where the first two terms represent the liquid water and the last two terms the water vapour.

The air mass balance equation is given by:

$$\text{div}(\underline{f}_{air}) + \frac{\partial}{\partial t}(\rho_{air} \phi (1 - S_{rw})) + \text{div}(\underline{f}_{air-a}) + \frac{\partial}{\partial t}(\rho_{air-a} \phi S_{rw}) - Q_{air} = 0$$

Where the first two terms represent dry air in gaseous phase and the last two terms represent dissolved air in water.

In the equations above:

- ρ_v, ρ_{air} and ρ_{air-d} are respectively the density of water vapour, air and dissolved air
- $\underline{f}_w, \underline{f}_v, \underline{f}_{air}$ and \underline{f}_{air-d} are the total mass flow for respectively liquid water, water vapour, air and dissolved air
- Q_w and Q_{air} are the sink terms for water and air
- ϕ is the porosity
- S_{rw} the water relative saturation

3.4.2 Fluid transport constitutive equations

Fluid transport is based on a 2-phase flow model. The liquid phase is composed of liquid water and dissolved air; The gaseous phase is a mixture of dry air and water vapour. The mass flows contain the advection of each phase defined by the generalised Darcy's law and the diffusion of the components within the phase given by Fick's law (Charlier, et al., 2013):

$$\underline{f}_w = \rho_w \underline{q}_l \quad \text{and} \quad \underline{f}_v = \rho_v \underline{q}_g + \underline{i}_v$$

$$\underline{f}_{air} = \rho_{air} \underline{q}_g + \underline{i}_{air} \quad \text{and} \quad \underline{f}_{air-d} = \rho_{air-d} \underline{q}_l + \underline{i}_{air-d}$$

Where:

- \underline{q}_l and \underline{q}_g are the advective fluxes for the liquid and gaseous phases
- $\underline{i}_v, \underline{i}_{air}$ and \underline{i}_{air-d} are the diffusion fluxes respectively for the water vapour, the dry air and the dissolved air

The advective fluxes are defined by the generalised Darcy's law for unsaturated cases (Charlier, et al., 2013):

$$\underline{q}_l = -\frac{\underline{K}_w^{sat} k_{rw}}{\mu_w} * \underline{grad}(p_w)$$

$$\underline{q}_g = -\frac{\underline{K}_g^{dry} k_{rg}}{\mu_g} * \underline{grad}(p_g)$$

Where:

- \underline{K}_w^{sat} and \underline{K}_g^{sat} are the water and gas permeabilities tensor in saturated and dry conditions
- k_{rw} and k_{rg} are the water and gas relative permeabilities
- μ_w and μ_g are the water and gas dynamic viscosities and $\mu_g = \frac{1}{\rho_g \mu_{air} + \rho_g \mu_v}$

The diffusion fluxes are related to Fick's law (Charlier, et al., 2013):

$$\underline{i}_v = -\phi(1 - S_{rw})\tau D_{v/air} \rho_g \underline{grad}\left(\frac{\rho_v}{\rho_g}\right) = -\underline{i}_{air}$$

$$\underline{i}_{air-d} = -\phi S_{rw} \tau D_{air-d/w} \rho_w \underline{grad}\left(\frac{\rho_{air-d}}{\rho_w}\right)$$

Where:

- $D_{v/air}$ and $D_{air-d/w}$ are the diffusion coefficient in the gaseous mixture of respectively dry air & water vapour and dissolved air in water
- τ is the tortuosity of the porous medium

3.4.3 Equilibrium restriction laws

Kelvin's law imposes the equilibrium between the water vapour in porous media and liquid water. This equilibrium restriction for vapour concentration in the gaseous phase is given by (Charlier, et al., 2013):

$$RH = h_r = \frac{p_v}{p_{v0}} = \exp\left(-\frac{sM_v}{RT\rho_w}\right)$$

Where:

- $RH=h_r$ is the relative humidity
- p_{v0} is the water vapour saturation pressure at the same temperature
 $\frac{1}{p_{v0}} = 194.4 \exp(-0.06374(T - 273) + 0.1634 \cdot 10^{-3}(T - 273)^2)$
- s is the suction
- R is the universal gas constant
- T is the absolute temperature.

Henry's law defines that the amount of dissolved air in the liquid phase should be in equilibrium with the quantity of dry air.

$$\rho_{air-d} = H_{air}(T)\rho_{air}$$

Where H_{air} is a temperature and water pressure dependent Henry's coefficient for dissolved air.

The heat flux \underline{f}_T is in this model dependent on two ways of heat transfer: conduction and fluid convection (Gerard, 2011):

$$\underline{f}_T = -\Gamma\nabla T + (c_{pw}\underline{f}_w + c_{pv}\underline{f}_v + c_{pair}\underline{f}_{air} + c_{pair-d}\underline{f}_{air-d})(T - T_0)$$

Where:

- Γ is the thermal conductivity of the porous medium
- c_{pw} , c_{pv} , c_{pair} and c_{pair-d} are the specific heats of water, water vapour, dry air and dissolved air respectively

3.4.4 Water retention curve

In the simulation the Van Genuchten retention curve is used. The Van Genuchten water retention curve is given by (Lagamine, 2008):

$$S_{rw} = \left(1 + \left(\frac{s}{P_0}\right)^m\right)^{-\left(1 - \frac{1}{m}\right)}$$

Where

- S_{rw} is the water relative saturation
- P_0 is a value close to the air entry pressure; it is not the real air entry pressure but for the sake of simplicity, this is called the air entry pressure throughout this document
- m is a fitting parameter

3.4.5 Relative permeability

The relative permeability of the fluids is not constant but depends on the degree of saturation. First the relative water permeability is given by the Van Genuchten water relative permeability model (Lagamine, 2008):

$$k_{rw} = \sqrt{S_{rw}} \left(1 - \left(1 - S_{rw}^{\frac{1}{n}}\right)^n\right)^2$$

Where

- $n = 1 - \frac{1}{m}$
- S_{rw} the degree of saturation obtained from the Van Genuchten curve

Second there is also the relative air permeability by the Van Genuchten model. That is given by the following equations (Lagamine, 2008):

$$k_{ra} = A \sqrt{1 - S_{rw}} \left(1 - S_{rw}^{\frac{1}{n}} \right)^{2n}$$

Where:

- A is a correction factor
- S_{rw} obtained from the Van Genuchten water retention curve

3.4.6 Thermal conductivity

The imposed thermal conductivity for the cavern, rock and lining was calculated based on the degree of saturation of water and air. This calculation is given by (Lagamine, 2008):

$$\Gamma_T = \eta S_w \Gamma_w + \eta S_a \Gamma_a + (1 - \phi) \Gamma_s$$

Where:

- Γ_T is the thermal conductivity of the material
- S_x is the degree of saturation for property x (water or air)
- Γ_x is the thermal conductivity of property x (water, air or rock)

3.4.7 Dynamic viscosity

The dynamic viscosity of water and air depends on the temperature. This relation is given by (Lagamine, 2008):

$$\mu_x(T) = \mu_x - \alpha_x^T \mu_x (T - T_0)$$

Where μ_x is the dynamic viscosity at reference conditions of material x and α_x^T the thermal coefficient.

3.5 Parameters of the model

This chapter deals with all the parameters excluding the geometrical and initial ones as they are already determined before. The parameters are categorized according to their property. The rock and concrete elements are mainly sharing elastic properties as they are within acceptable ranges and adequate for this study, as the focus lies on the thermo-hydraulic behaviour and not the mechanical behaviour. The reference temperature and pressure is set at 20°C and 0.1MPa respectively.

3.5.1 Hydraulic parameters

Table 1 gives an overview of the hydraulic parameters of the different materials.

Table 1 Material properties used as base for modelling the underground cavern.

Parameter	Symbol	Cavern	Concrete Lining	Rock
Porosity (-)	ϕ	1.00	0.15	0.15
Tortuosity (-)	τ	0.412	0.412	0.412
Intrinsic permeability (m ²)	K	10 ⁻⁹	10 ⁻¹⁹	10 ⁻¹⁷
Air entry pressure (MPa)	P ₀	1.47 10 ⁻²	1.47	1.47
Van Genuchten fitting parameter (-)	m	15	2.469	2.469
Relative permeability parameter (-)	n	0.933	0.595	0.595
Relative water permeability (-)	k _{rw}	1	Variable	Variable
Relative air permeability (-)	k _{ra}	1	Variable	Variable

The type of rock simulated is a sedimentary claystone. The concrete lining and the rock are assumed to share most hydraulic parameters, except the intrinsic permeability. The porosity is assumed to be 0.15 and the intrinsic permeability $10^{-17}m^2$. For the concrete lining, a higher intrinsic permeability is of $10^{-19}m^2$ is taken. All rock parameters were obtained from (Gerard, 2011). The tortuosity of the porous medium is related to the diffusion of gas given by the Fick's law. This parameter was obtained from (Gerard, 2011) and gives an idea of the ease molecules can move between the pores.

The cavern is a porous medium and assumed to have a porosity of 1. The tortuosity is taken equal to the one of the rock and lining. The intrinsic permeability is de facto 1, however for numerical reasons a value that is orders of magnitude lower than the one for rock and lining is used.

Next, the hydraulic parameters cover also the water retention curve. The general retention curve used for the lining and the rock is the one used in (Kim, et al., 2012). Remark again that the P_0 is not the real air entry pressure, it is a value close to it. As the cavern has no real physical water retention curve, an artificial one is created for numerical purposes. This curve should have a sharp and steep transition at low suction in comparison with the other water retention curve. The cavern has ideally an air entry pressure close of 0 MPa. However, for numerical reasons this would not be possible. This is why the air entry pressure is taken two orders of magnitude smaller as the one of the rock at 14.7kPa, which is sufficient. The fitting parameter is put at 15 to have a steeper slope of the curve. Figure 6 shows both water retention curves in a log-scale.

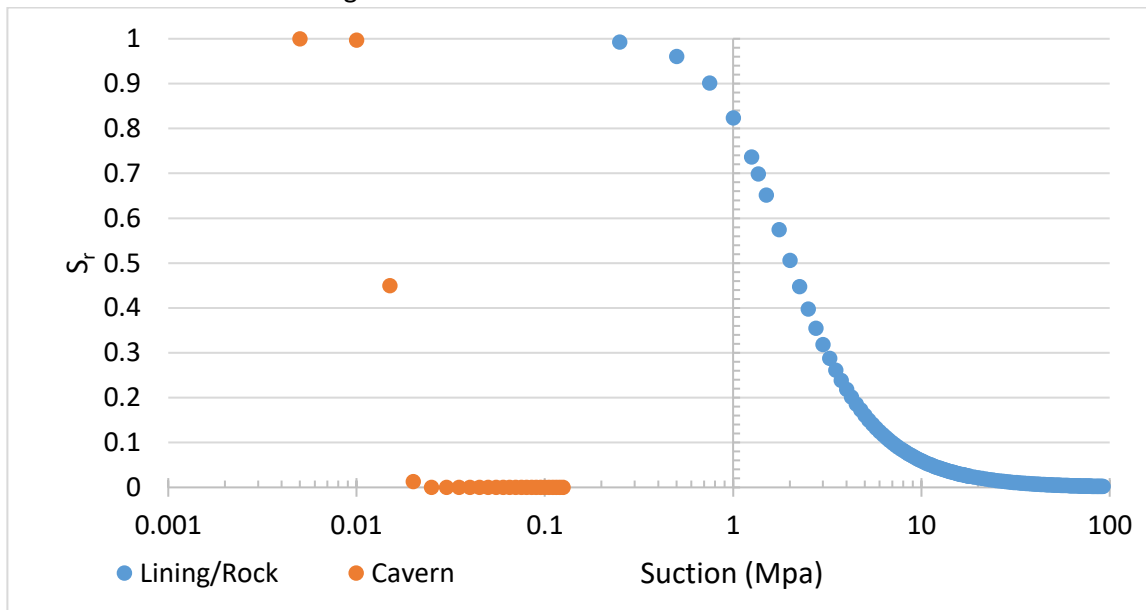


Figure 6 Water retention curve by the Van Genuchten equation for the lining/rock and the cavern.

The concrete lining is installed at a degree of saturation of 70%. With a backward calculation, it is possible to determine the corresponding suction:

$$s = P_0 \left(S_r^{-\frac{1}{m}} - 1 \right)^{\frac{1}{m}}$$

This leads to a suction pressure of 1.357MPa. To determine the initial water pressure that is imposed on the lining elements, it is still needed to take into account the initial gas pressure as the suction is given by:

$$s = P_g - P_w$$

Thus the water pressure in the concrete is $P_w = P_g - s = 0.1MPa - 1.357MPa = -1.257MPa$

As showed before in Balance equations and constitutive equations, the relative permeability is linked to the Van Genuchten retention curve. Therefore, both parameters of the water retention curve and the relative water/air permeability are taken the same. The dependency between the degree of saturation and the relative permeability is plotted in Figure 7. For the cavern it is assumed that the relative water/air permeability is equal to 1.

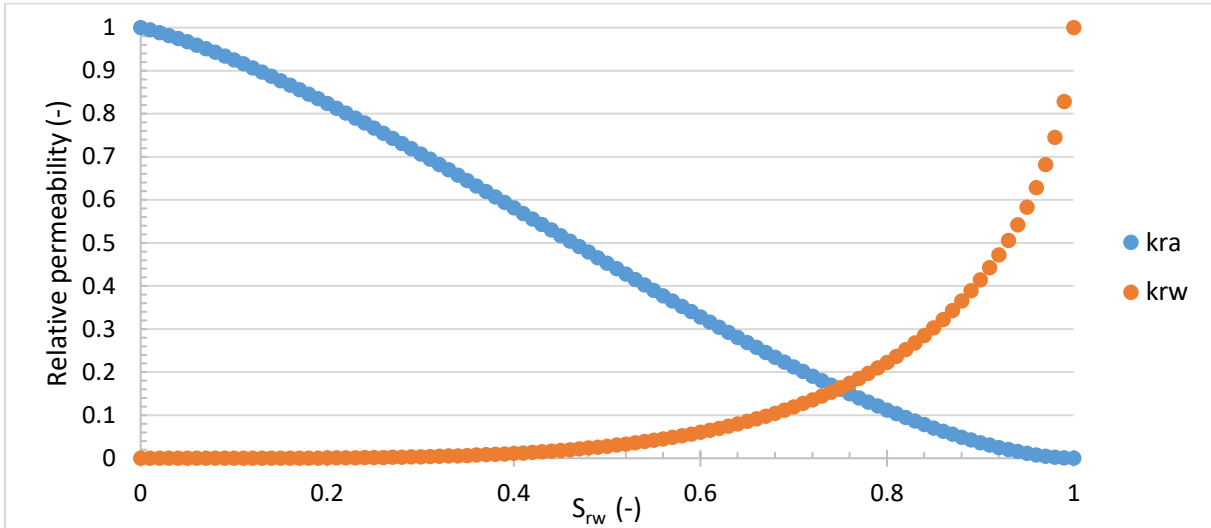


Figure 7 Relative permeability for water and air depending on the degree of saturation.

3.5.2 Thermal parameters

As mentioned before in Initial conditions, initially the temperature is 13°C. The thermal parameters are of great importance in the thermo-hydraulic simulation as they cause pressure variations due to the temperature variation. This is based on the ideal gas law as the volume of the cavern stays constant. The thermal parameters for the different materials are given in Table 2. Thermal parameters that are applied are the thermal conductivity and the specific heat. The thermal conductivity is used in the model to simulate the heat transfer by conduction. The specific heat is used to simulate heat transfer by convection. The thermal conductivity for the rock and lining has a constant value attributed that is calculated based on its properties. For the cavern, the value of air is used.

The thermal properties of the lining and rock were taken from Rutqvist's research (Rutqvist, et al., 2012) with an equal specific heat of 900J/kg.K and a thermal conductivity of 3W/m.K. This value has to be used as Γ_x in the formula defined in the subchapter Thermal conductivity.

For the solid particles of the concrete lining which is installed at a degree of saturation of 70% the thermal conductivity is obtained through:

$$\Gamma_{T_{lining}} = 0.15 * 0.70 * 0.58 \frac{W}{mK} + 0.15 * 0.30 * 0.0257 \frac{W}{mK} + 0.85 * 3 \frac{W}{mK} = 2.612 \frac{W}{mK}$$

For the rock, which is assumed to be always completely saturated to determine the conductivity:

$$\Gamma_{T_{rock}} = 0.15 * 1 * 0.58 \frac{W}{mK} + 0.85 * 3 \frac{W}{mK} = 2.637 \frac{W}{mK}$$

Table 2 Thermal parameters used as base case for modelling of the thermal aspect of CAES-operation in a lined cavern.

	Thermal conductivity Γ (W/m.K)	Specific heat c_p (J/kg.K)
Cavern	0.0257	1005
Concrete lining	2.612	900
Rock	2.637	900

3.5.3 Fluid properties

In this part all parameters related to the water and air are mentioned. In the model air and water are two important materials as they flow through the model. Therefore, some basic parameters needed to perform the simulation are given in Table 3. These are liquid and gas parameters, which in this simulation are water and air respectively. The Henri coefficient which is related to the gas solubility in water is based on the reference conditions (Gerard, 2011).

Table 3 Parameters for water and air for modelling the underground cavern.

	Symbol	Water	Air
Specific mass (kg/m ³)	ρ_x	1000	1.205
Liquid compressibility (1/Pa)	$\frac{1}{\chi_w}$	$5 \cdot 10^{-10}$	-
Dynamic viscosity (Pa.s)	μ_x	0.001	$1.86 \cdot 10^{-5}$
Dynamic viscosity thermal coefficient (1/K)	α_x^T	$2.07 \cdot 10^{-4}$	0.00343
Henri coefficient (-)	H_{air}	-	0.0234
Thermal conductivity (W/m.K)	γ	0.58	0.0257
Specific heat (J/kg.K)	c_p	4186	1005

Chapter 4 Results

This chapter deals with all obtained results from both the unlined and lined model. The insights provided by this chapter allow to answer the questions posed in Objectives of the thesis.

4.1 Hydraulic model

4.1.1 Injection in rock without lining

This chapter deals with the easiest case. Its goal is to show the need of a lining system to have an efficient operation. This model can be applicable on a cavern that is already present in the underground or that can be made by human without much disturbance of the surrounding rock. In fact, to have acceptable leakage, the ground has to be low permeable as different earlier studies have shown, like (McGrail, et al., 2013; Kim, et al., 2012). Depleted reservoirs or artificially made salt caverns are closely related to this model. The most important parameter is the intrinsic permeability which should be as low as possible. Leakage of air out of the cavern is directly related to the intrinsic permeability as is proved in the following.

4.1.1.1 Excavation and drainage

The water pressure is lowered as described in Simulation. The time needed to reach a steady-state depends on many factors of the model. For this reason, different times were imposed to find the critical time where steady-state is reached. Figure 8 shows the water pressure profile and the influence of waiting time for a rock with an intrinsic permeability of 10^{-18}m^2 . From this graph it is visible that from one month a steady-state is reached. Remark that the long term drainage has a totally different distribution in reality as the radius of influence will surpass the distance of the model (30m). The size of the mesh should be increased to limit boundary effects. The goal is just to have an equal steady-state in all our simulations. For this reason, one month was chosen as time period for the waiting period between excavation and beginning of injection.

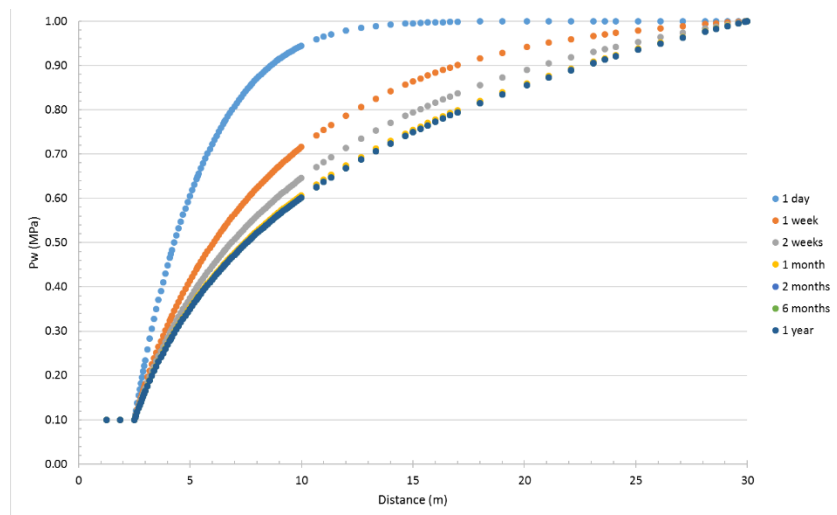


Figure 8 Water pressure distribution in the rock during the excavation phase of a rock with an intrinsic permeability of 10^{-18}m^2 for different time periods in order to find a steady-state solution.

4.1.1.2 Initialisation phase

After the second stage, which brings the cavern up to a base pressure, the water and air pressure distribution in the rock shown in Figure 9 is observed. It is clear that in the unlined model, the air pressure level of the cavern is also observed in the first cm's of rock after which the pressure falls back quite rapidly. This makes that the affected zone is until about 2.9m from the cavern center. The water pressure near the cavern wall increases because water is compressed by the air injection. On the other side the affected zone is much larger, about 10m, reaching a minimum after which it starts to go back to the initial water pressure. The desaturated zone in the rock is about 20cm.

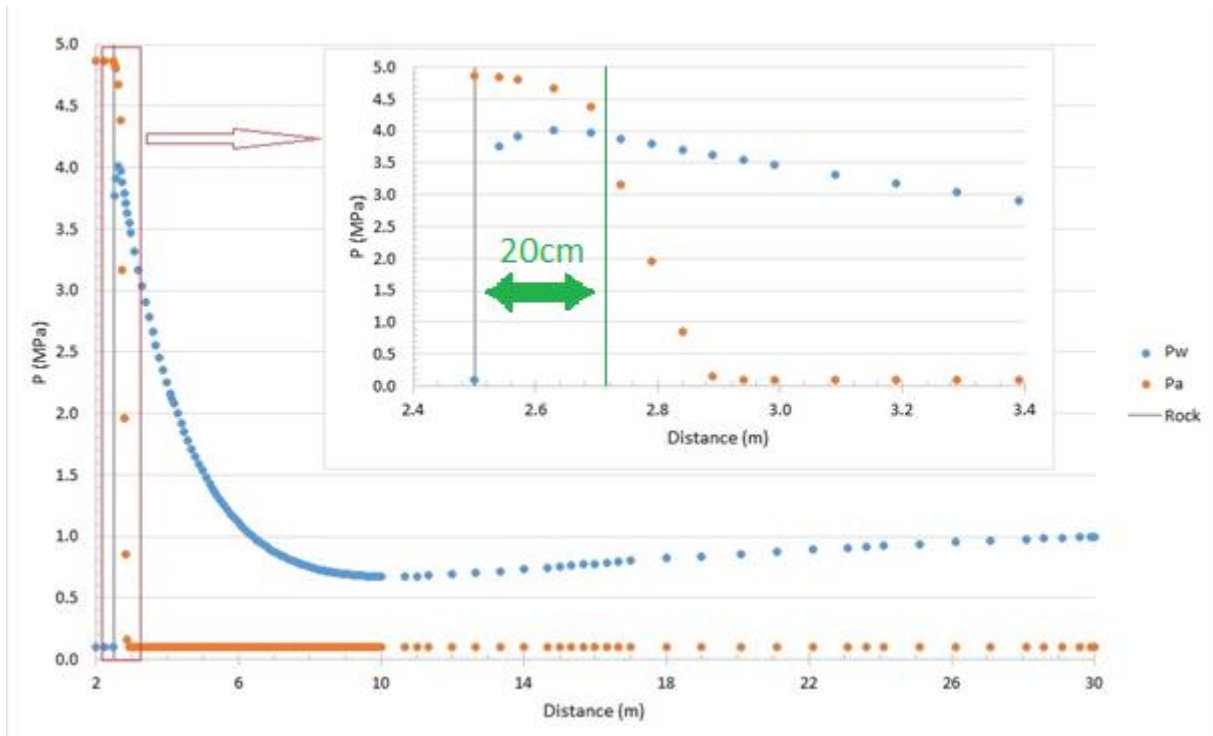


Figure 9 Water and air pressure distribution after the initialisation phase and zoom on the first meter in the rock.

4.1.1.3 Operational phase

The third stage which represents the real CAES-operation with daily cycles was simulated for 81 days.

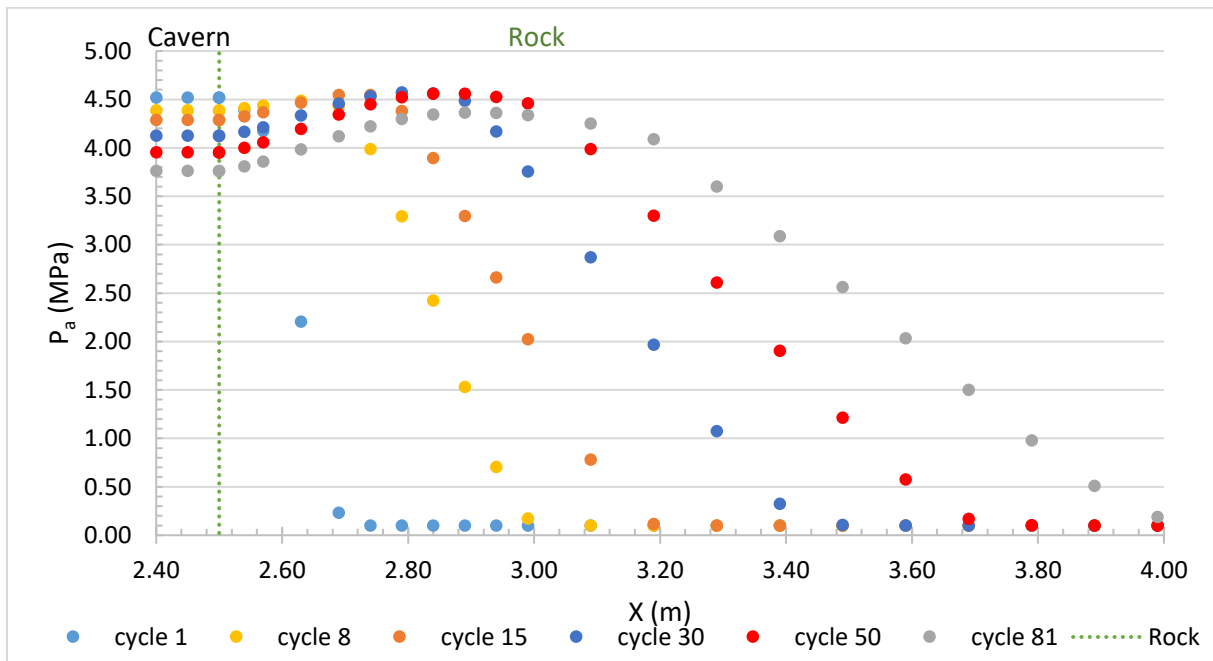


Figure 10 Horizontal air pressure profile for different cycle during CAES-operation after the last waiting period in the cycle.

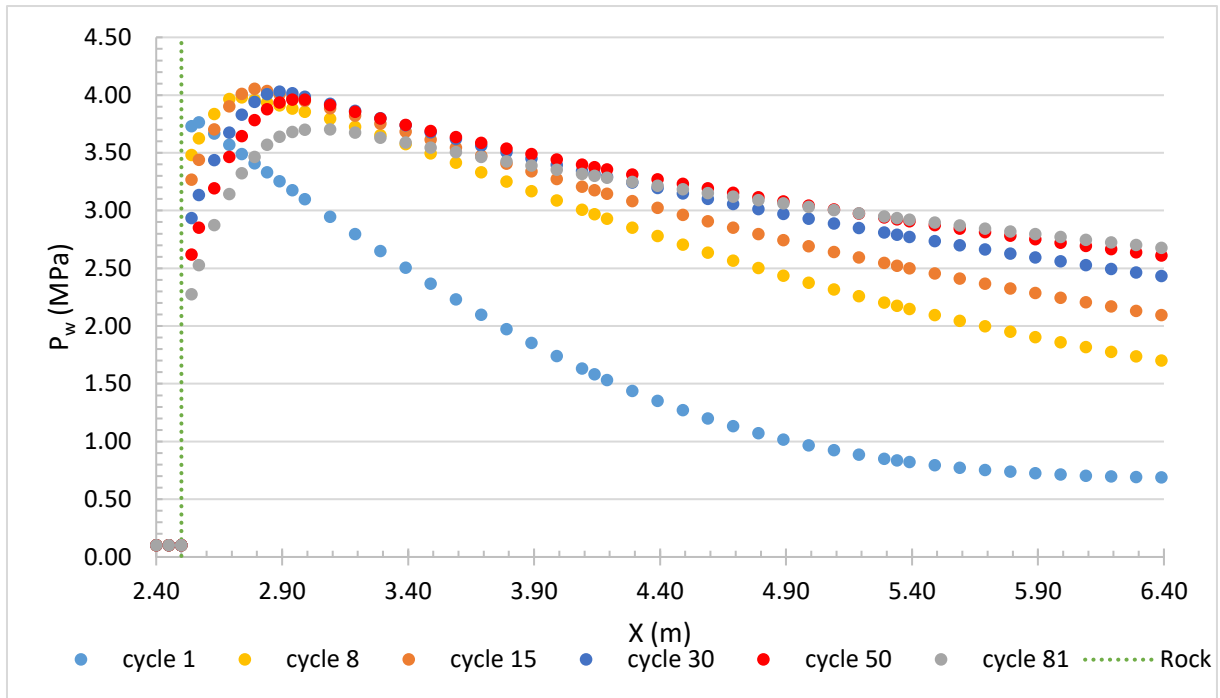


Figure 11 Horizontal water pressure profile for different cycles during CAES-operation after the last waiting period in the cycle.

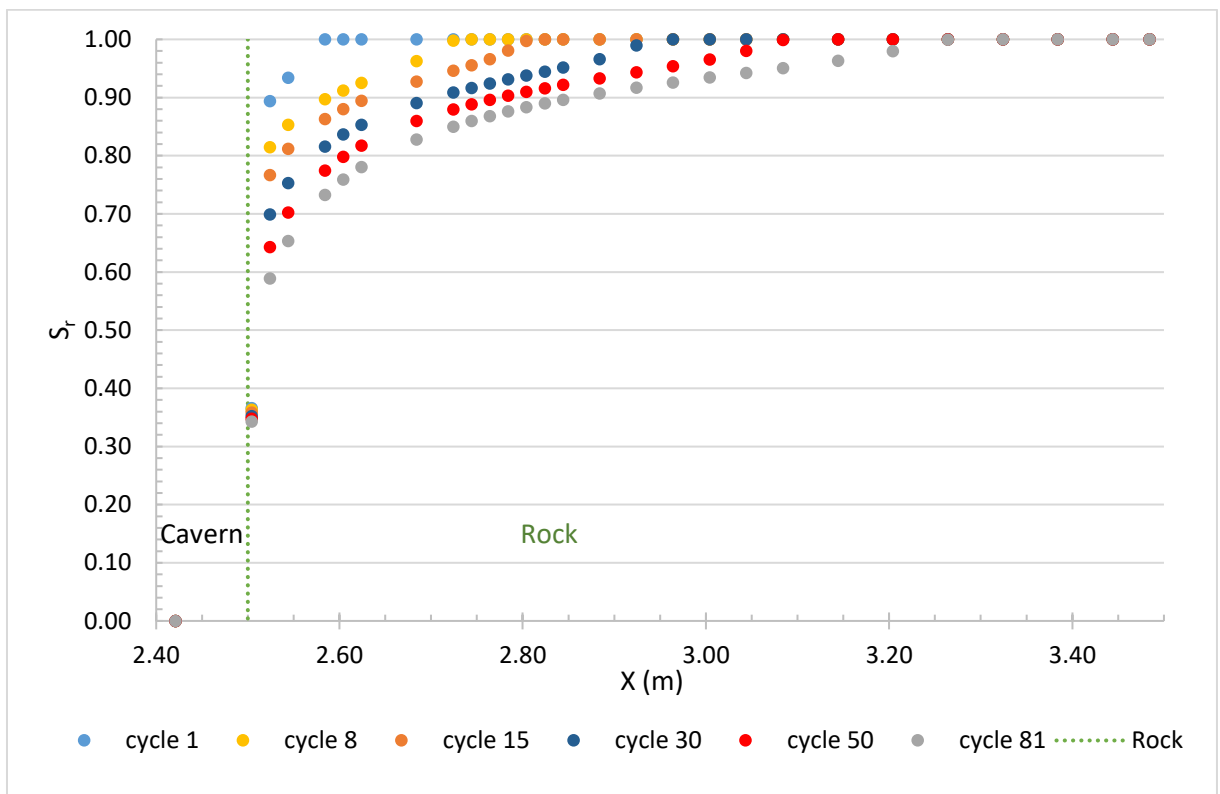


Figure 12 Horizontal degree of saturation profile for different cycles during CAES-operation after the end of the last waiting period in the cycle.

Figure 10-Figure 12 show clearly the migration of air into the rock with each cycle. In the rock, air pressure increases with time and the migration of air also increases. The water pressure changes due to air injection. Close to the cavern it decreases, further away it increases due to the air that compresses water. The degree of saturation lowers as a part of the water is pushed away and replaced

by air. In the cavern, the air pressure decreases with time. This indicates, that there is a loss of air mass in the cavern and thus, leakage of air in the rock. Not only is the leakage an unwanted effect, it can also put the total efficiency of the energy production process under pressure. This is further threatened in Effect of the permeability on leakage.

The efficiency of the CAES-operation can be expressed by the leakage rate. This leakage rate can be calculated based on the ideal gas law and the pressure observed at two equivalent moments in time, preferable the end of a cycle. The time chosen can modify the results because the temperature is fixed and the calculation is based on the ideal gas law. This loss is determined by the average of the air pressure at the different nodes in the cavern. These pressures should be more or less homogeneous due to the high permeability and porosity of the cavern. The efficiency is calculated according to following procedure:

First the mass of air is determined according to the ideal gas law:

$$m = \frac{PV_{cavern}}{R_{air}T}$$

Where:

- m, the mass of air (kg)
- P, the cavern pressure (Pa)
- V, the volume of the cavern (m³)
- R_{air}, specific gas constant for air $R_{air} = \frac{R}{M} = \frac{8.3144598 \frac{J}{K mol}}{28.97 \frac{g}{mol}} = 286.9 \frac{J}{K kg}$

Then the mass of air that is lost is calculated by:

$$\Delta m = \frac{V_{cavern}}{R_{air}} \left(\frac{P_1}{T_1} - \frac{P_2}{T_2} \right)$$

Where the difference is made between the former and latter state. Based on the time between the two states, the leakage rate and average daily leakage can be calculated as:

$$leakage\ rate = \frac{\Delta m}{\Delta t}$$

Based on the original, non-adapted, injection rate of 0.0198 kg/s, the total mass of air injected in the cavern can be calculated by:

$$Injected\ mass = injection\ rate * 8h$$

After which the leakage and efficiency in % can be calculated by:

$$Leakage = \frac{injected\ mass - (injected\ mass - mean\ daily\ leakage)}{injected\ mass} * 100$$

$$Efficiency = 1 - Leakage$$

In the reference case with a permeability of 10⁻¹⁸m² this leads to an average daily leakage of 0.40% calculated over 80 cycles.

4.1.1.4 Effect of the permeability on leakage

In this chapter the influence of the intrinsic permeability is investigated on the observed behaviour.

Figure 14 shows that no matter which intrinsic permeability the rock has, the air pressure in the cavern is always dropping. The size of reduction is strongly influenced by the permeability. Higher permeability leads to easier migration in the rock, which can also migrate further in the rock, explaining the strong decrease in pressure (Figure 15). The strange behaviour of the 10⁻¹⁷m² permeability having a higher

pressure initially is due to the end of the initialisation phase. At the end of this phase, the pressure in the cavern is 5.08MPa, while for a rock permeability with $10^{-18}m^2$ this pressure is 4.55 MPa. An explanation can be found in the water pressure profile obtained after drainage, before injection starts. Figure 13 shows the horizontal pressure profile. Clearly three categories can be distinguished.

The intrinsic permeability of $10^{-19}m^2$ and $10^{-18}m^2$ each have their own curve. All other curves tend towards the same pressure profile due to easier water flow.

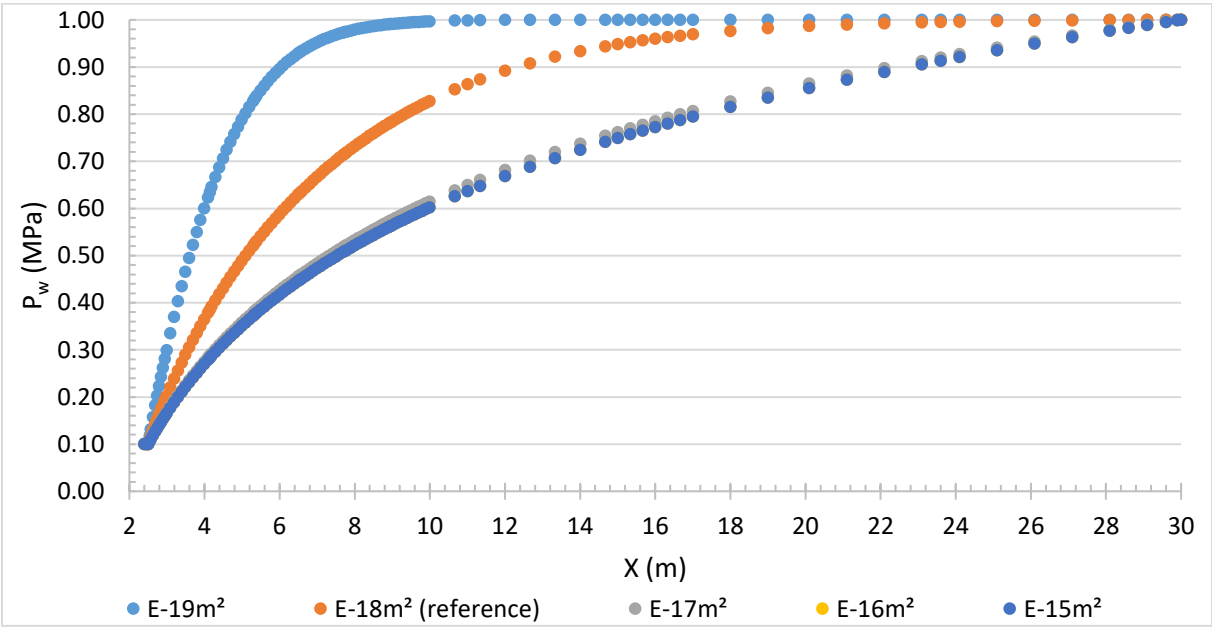


Figure 13 Horizontal water pressure profile for different rock permeabilities after drainage.

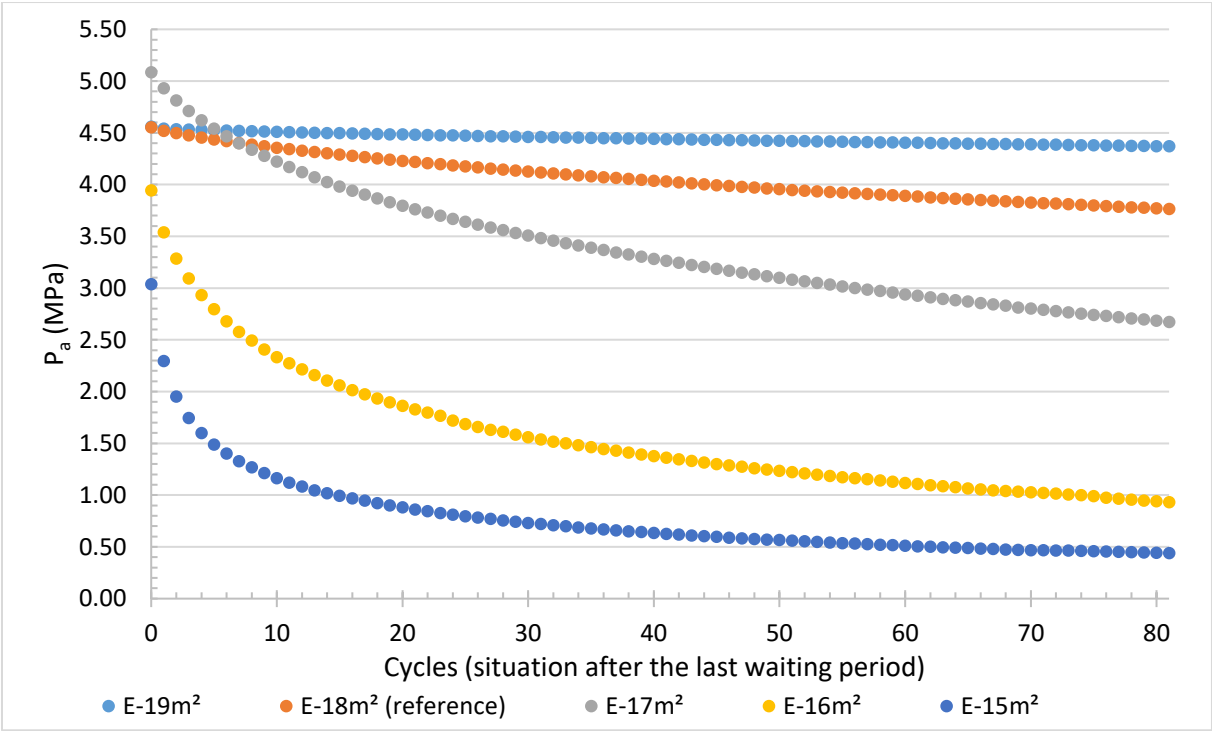


Figure 14 Cavern pressure evolution during CAES-operation for different intrinsic permeabilities.

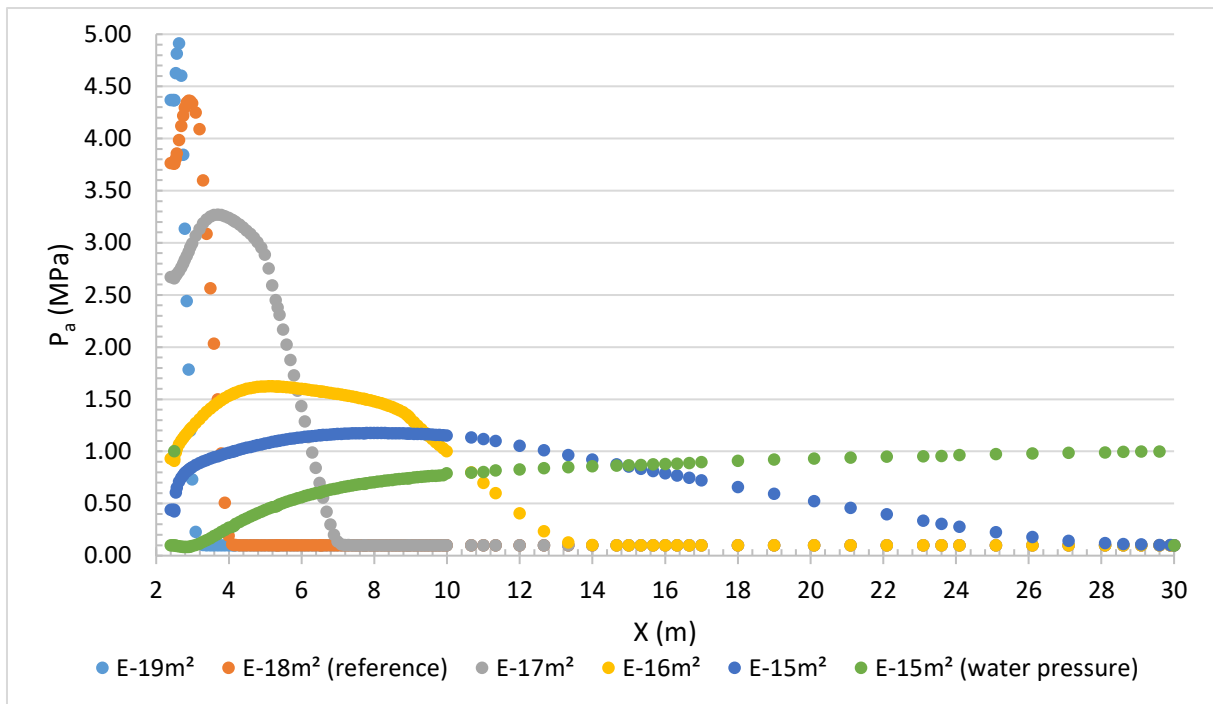


Figure 15 Horizontal air pressure profile at the end of cycle 81 for different rock permeabilities and the water profile for the highest permeability.

Figure 15 shows the horizontal air pressure profile after the last waiting period of cycle 81 for different rock permeabilities. The air migration is directly related to the intrinsic permeability. The air pressure in the cavern lowers due to leakage. This causes more uniform air pressure in the first ten meters of the rock for high permeabilities.

Table 4 Leakage rate and leakage for different permeabilities based on 80 cycles

Permeability	$10^{-19}m^2$	$10^{-18}m^2$	$10^{-17}m^2$	$10^{-16}m^2$	$10^{-15}m^2$
Leakage rate(kg/s)	5.92E-06	2.62E-05	7.81E-05	9.02E-05	6.42E-05
Leakage (%)	0.090	0.397	1.183	1.367	0.972

Table 4 shows the results obtained by using the pressure in the cavern between the end of cycle 1 and the end of cycle 81, thus containing the average of 80 cycles. The full calculation can be found in Appendix C.

Clearly the leakage and leakage rate increase with increasing permeability. However, for high permeabilities $10^{-15}m^2$, these results start again to decrease. As Figure 14 also shows for a permeability of $10^{-15}m^2$, the last 30 cycles, the pressure does not change much as it seems that a plateau has been reached. This can be explained by the fact that never all the air will migrate in the rock. During the 8h waiting time between withdrawal and injection, the pressure is already that low that it does not have sufficient pressure to push the higher initially leaking volumes into the rock. At around 15m the water pressure is sufficient to the hydrostatic water pressure is able to keep the air from migrating further (Figure 15).

In conclusion, without a lining, the leakage stays rather limited. However, on large scale applications this still is a large amount loss in absolute numbers. In the full process where a CAES-plant is integrated, the efficiency of the full process is strongly influenced by the CAES-efficiency as lower pressure means that air has to be recompressed in order to use it in the modified gas turbine. The next section studies the impact of a lining on the efficiency of the system.

4.1.2 Injection in rock with lining

In this stage a lining is introduced. A 50cm thick concrete lining is installed at 2.5m-3m. First, the reference case is discussed which forms a baseline for the sensitivity analysis. The reference case has the same parameters as the previous case studied. The only difference is the water pressure imposed in the concrete lining at -1.257MPa . Table 5 repeats the used material intrinsic permeabilities.

Table 5 Intrinsic permeabilities for the hydraulic lined reference model.

	Cavern	Lining	Rock
Intrinsic permeability (m^2)	10^{-9}	10^{-19}	10^{-17}

4.1.2.1 Reference model

4.1.2.1.1 Excavation and drainage

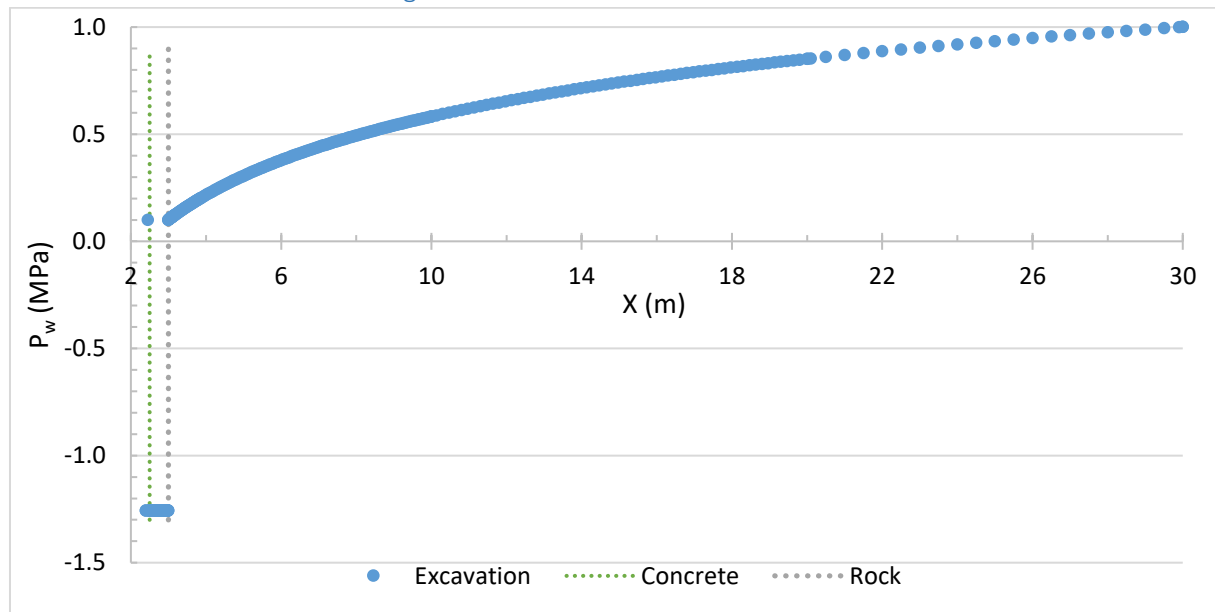


Figure 16 Water pressure after the initialisation phase with at the concrete lining an imposed value related to the suction at a saturation of 70% (H).

The 30 days' drainage is applied at 3m (the future interface between the concrete lining and the rock). The horizontal water pressure profile at the end of the waiting time is shown in Figure 16. On the left side, towards the cavern, a different behaviour is observed as the lining is installed after draining.

4.1.2.1.2 Initialisation phase

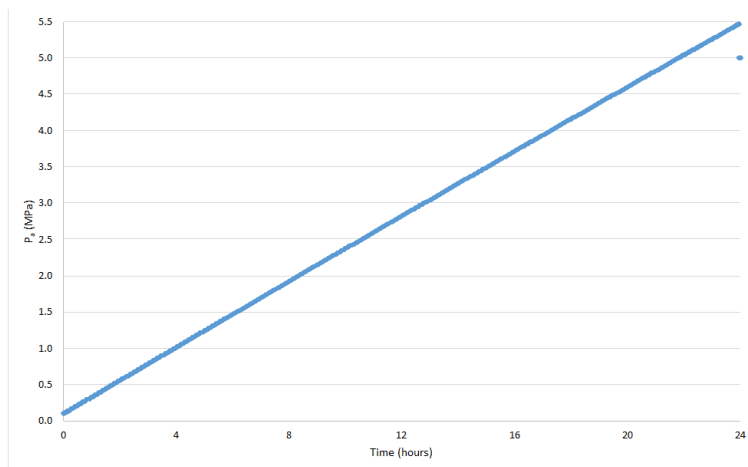


Figure 17 Evolution of the cavern pressure at the end of the initialisation phase (H).

During the initialisation phase, pressure builds up in the cavern, which happens linearly as Figure 17 shows. After the initialisation, the air pressure reaches around 5.5MPa. As the lining has a lower permeability than the unlined model, it is logical that there is less migration of air in the rock in comparison with the model without lining (Figure 19). At 2.7m the air pressure is again almost at the initial

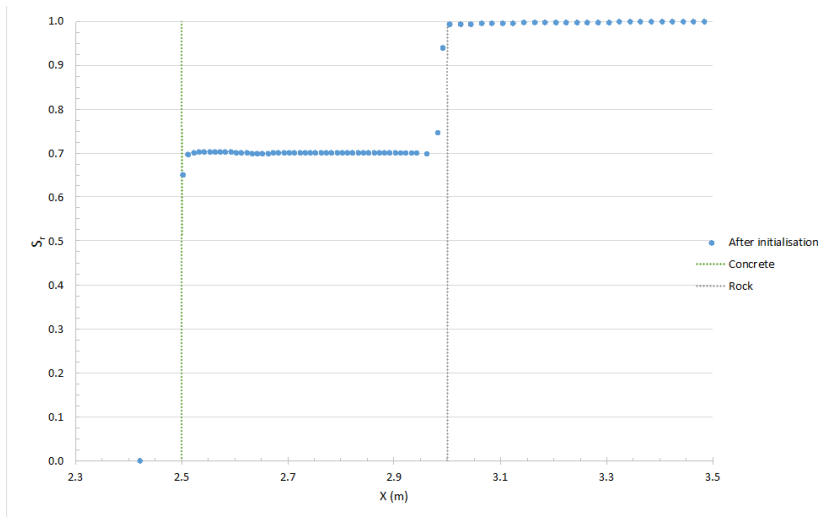


Figure 18 Degree of saturation after initialisation phase with the lining clearly still at 70% (H).

atmospheric pressure at the end of the initialisation phase, which is almost half of the migration distance encountered in the unlined model which was for a rock with an intrinsic permeability of $10^{-18}m^2$. Also the water pressure follows clearly the air pressure in that region, it has the same slope until the initial imposed water pressure. Also the degree of saturation of the lining (Figure 18) does not change except at the boundaries to have a smooth

transfer between the lining (70%) and rock (100%).

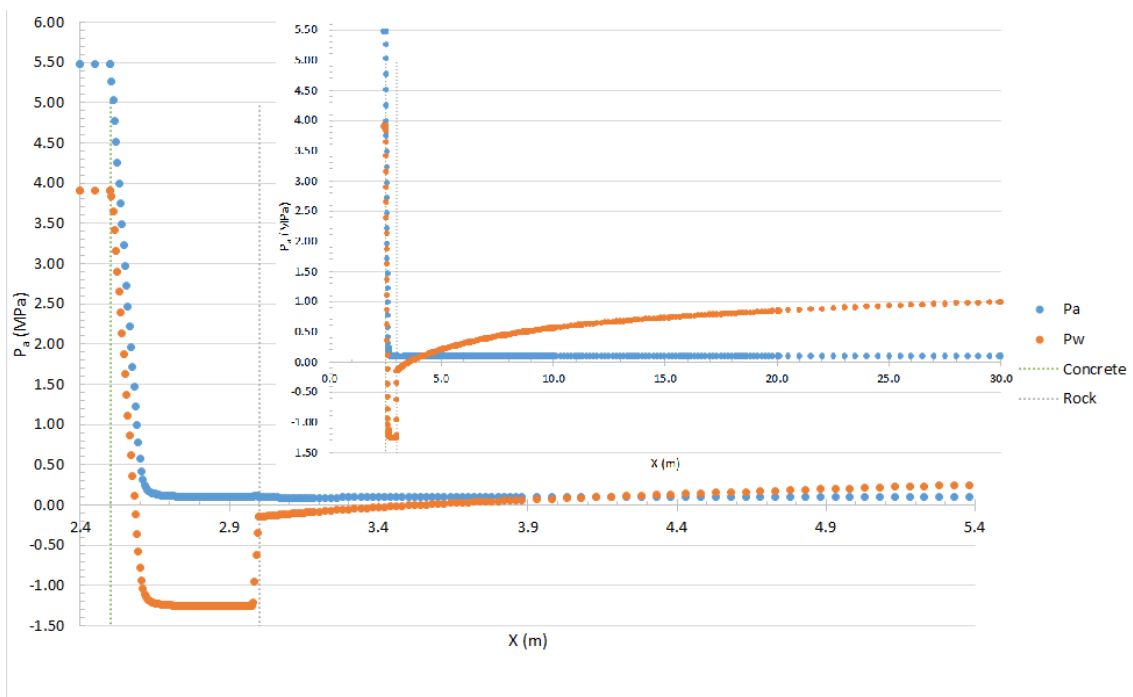


Figure 19 Water and air pressure after the initialisation phase when a concrete lining separates the cavern from the rock (H).

4.1.2.1.3 Operational phase

Before looking at the individual results during the real CAES-operation, let's first look at what happens in the cavern during a cycle. As Figure 20 immediately shows the overall pressure in the cavern decreases with the higher number of cycles performed. While the air pressure during the 1st cycle initially starts at 5.5MPa reaching 7.2Mpa as maximum, due to leakage the pressure decreases with the number of cycles to 3.7 and 5.5 MPa respectively for the 81st cycle. A clear distinguishing can be immediately made between the different stages of a cycle.

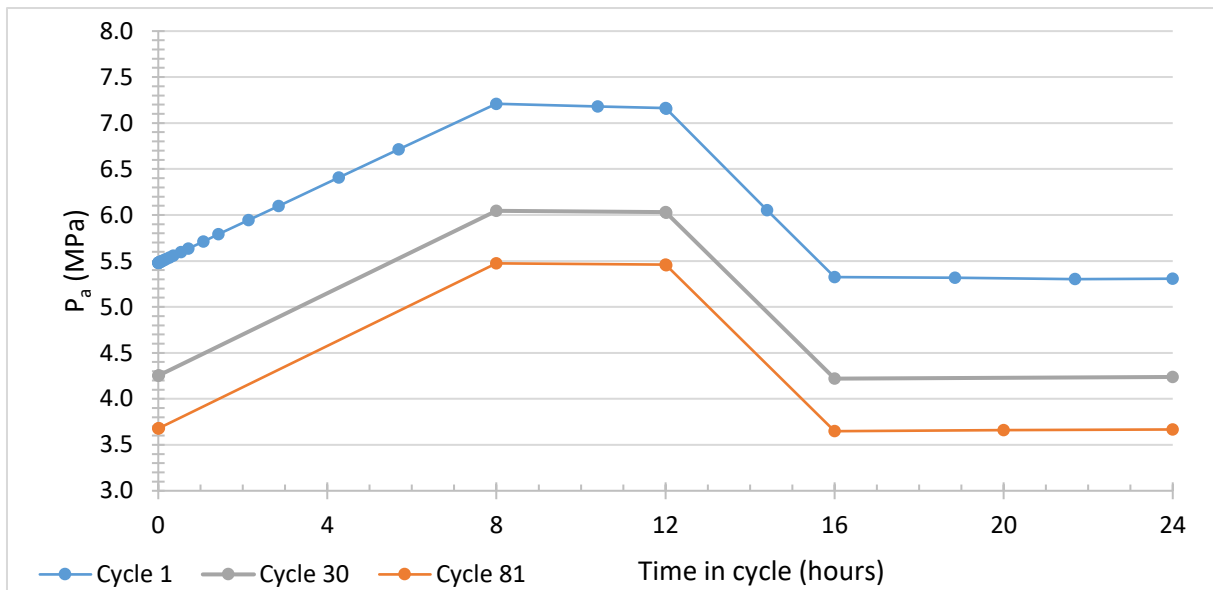


Figure 20 Evolution of the cavern pressure during one operational cycle for different cycles (H).

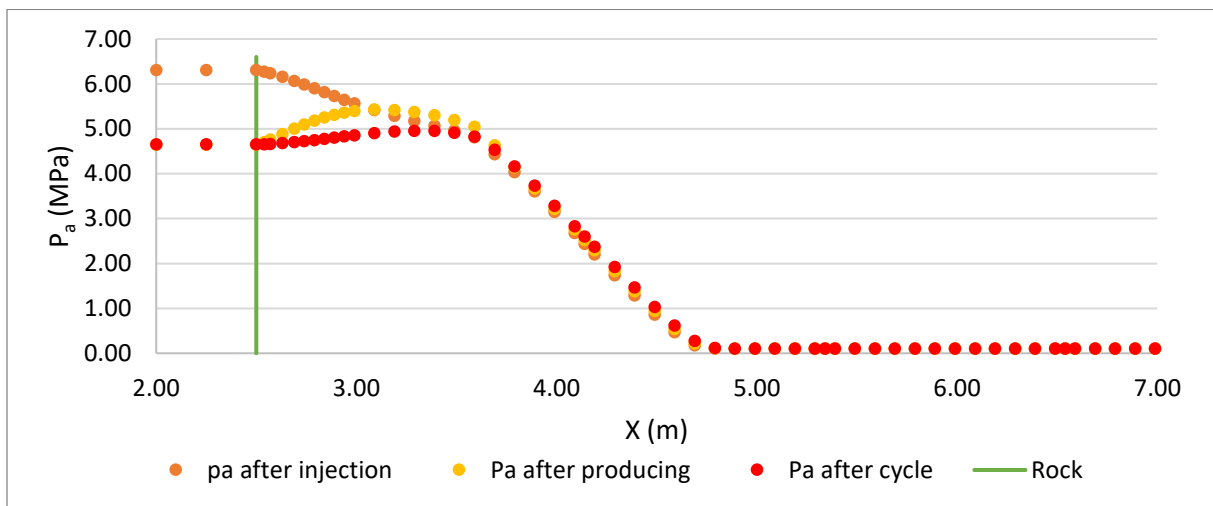


Figure 21 Air pressure profile at different stages of the 1st cycle (H).

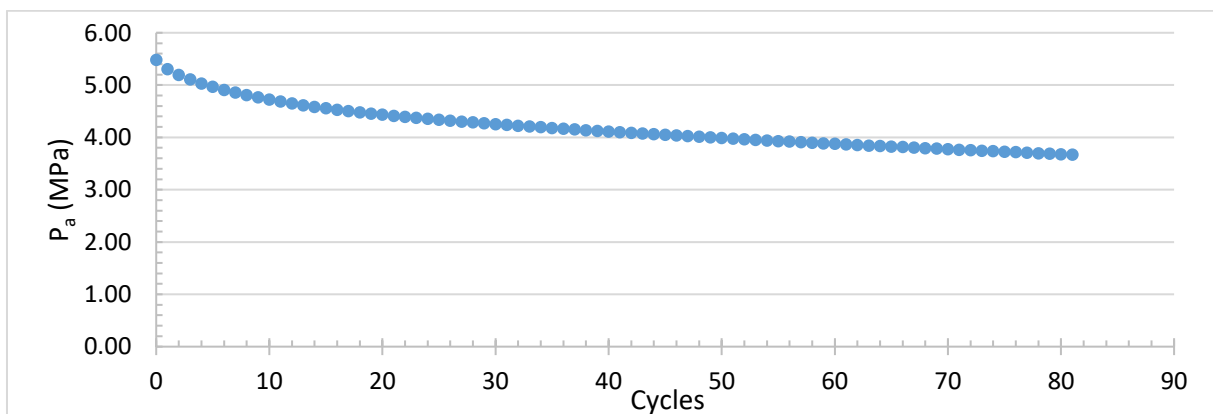


Figure 22 Evolution of the cavern air pressure during the CAES-operational cycles at the end of each cycle (H).

Figure 22 confirms what was observed in the pressure behaviour during a cycle. The general pressure at the end of the cycle, drops continuously. Already after a few daily cycles the pressure starts rising in the rock (Figure 23). In the lining a peak in air pressure is visible at the end of each cycle. This is related

to the status in which the cycle is. Figure 21 shows the pressure in the rock at different stages of the first cycle. After injection, the pressure is monotonically descending. But as air is withdrawn afterwards, air flows back to the cavern and the pressure lowers. Due to the permeability a part of the air remains in the rock, explaining the peak observed for the after producing and after the last waiting period.

In the rock, clearly two slopes are visible in the horizontal air pressure profile (Figure 23). These slopes are related to the velocities of the fluid flows. There is the velocity of the dissolved air on the right and on the left the Darcy flow determines the velocity. On the right axis the degree of saturation for each cycle is shown. Clearly the transition between the two velocities is related to the degree of saturation. In the saturated rock, the dissolved air velocity is active. Those two velocities are also clearly visible in Figure 24 in the dark blue and cyan colour.

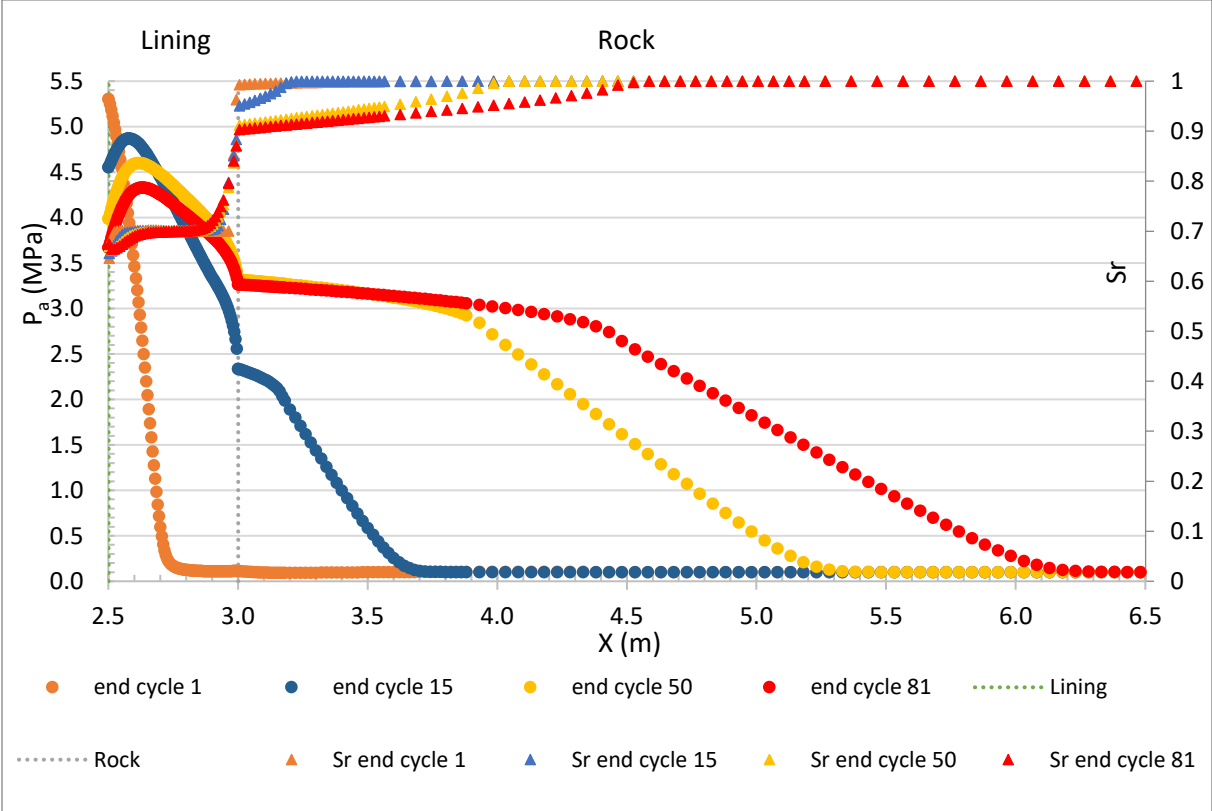


Figure 23 Transition of the air pressure throughout the rock at the end of CAES-operational cycles (left) and evolution of the degree of saturation with increasing number of CAES-cycles showing the situation at the end of the cycle (right) (H).

Figure 25 shows the water pressure profile at the end of different cycles. Initially the water pressure in the lining is negative due to the degree of saturation of 70%. The negative water pressure disappears rapidly due to the air injection as the water is further compressed by the air. Next to this, there is a water flow from the rock to the cavern as the outer boundary of the rock is always imposed at 1MPa. Despite the increasing water pressure, the lining remains desaturated at 70% which is confirmed by Figure 23. This was also observed in the investigation of (Rutqvist, et al., 2012). It is clear that with each cycle the degree of saturation in the rock is lowered further in the rock. At cycle 81 this has influence until 4.5m. The cavern is always completely desaturated.

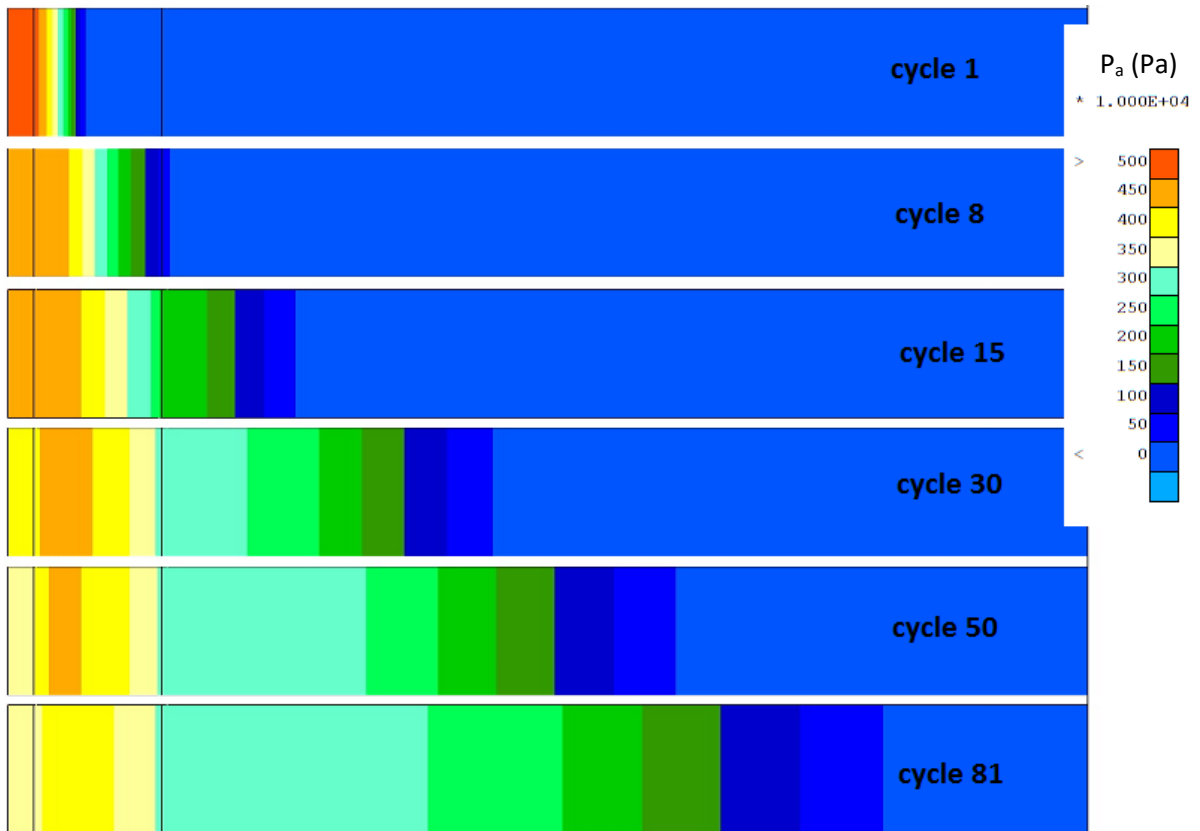


Figure 24 Migration of the air pressure front in the surroundings of the cavern, situation at the end of the cycle (H).

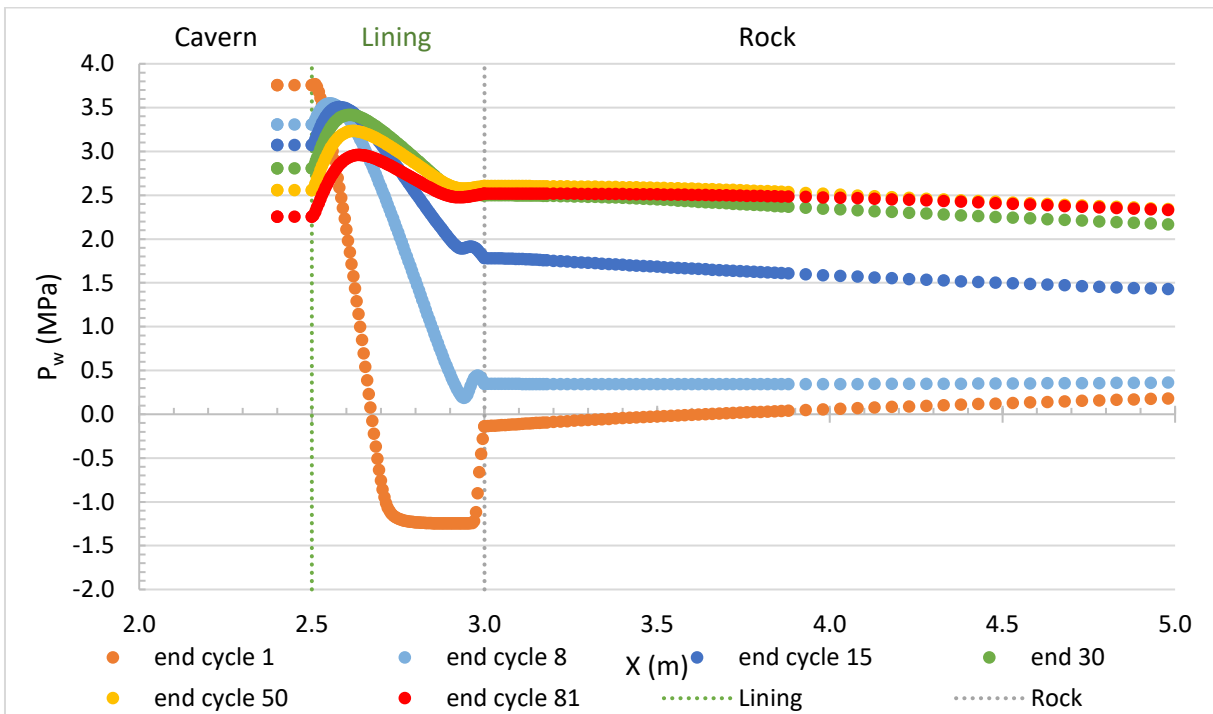


Figure 25 Evolution of the water pressure at the end of CAES-operational cycles (H).

4.1.2.2 Sensitivity analysis

In the following, the effects caused by changing different parameters is compared to the reference case. At the end of the chapter the leakage obtained for all sensitivity analyses are compared.

4.1.2.2.1 Intrinsic permeability

The intrinsic permeability is directly related to the leakage as mentioned in the unlined model. Here an intrinsic permeability of 10^{-20}m^2 for the lining and 10^{-16}m^2 for the rock is used. Thus, one order in magnitude lower and higher, respectively. In the excavation stage the differences are neglectable. Also for the initialisation, in the cavern itself, this is similar to the reference case. The first real influence of the adapted permeability lies in the longitudinal pressure profile after initialisation.

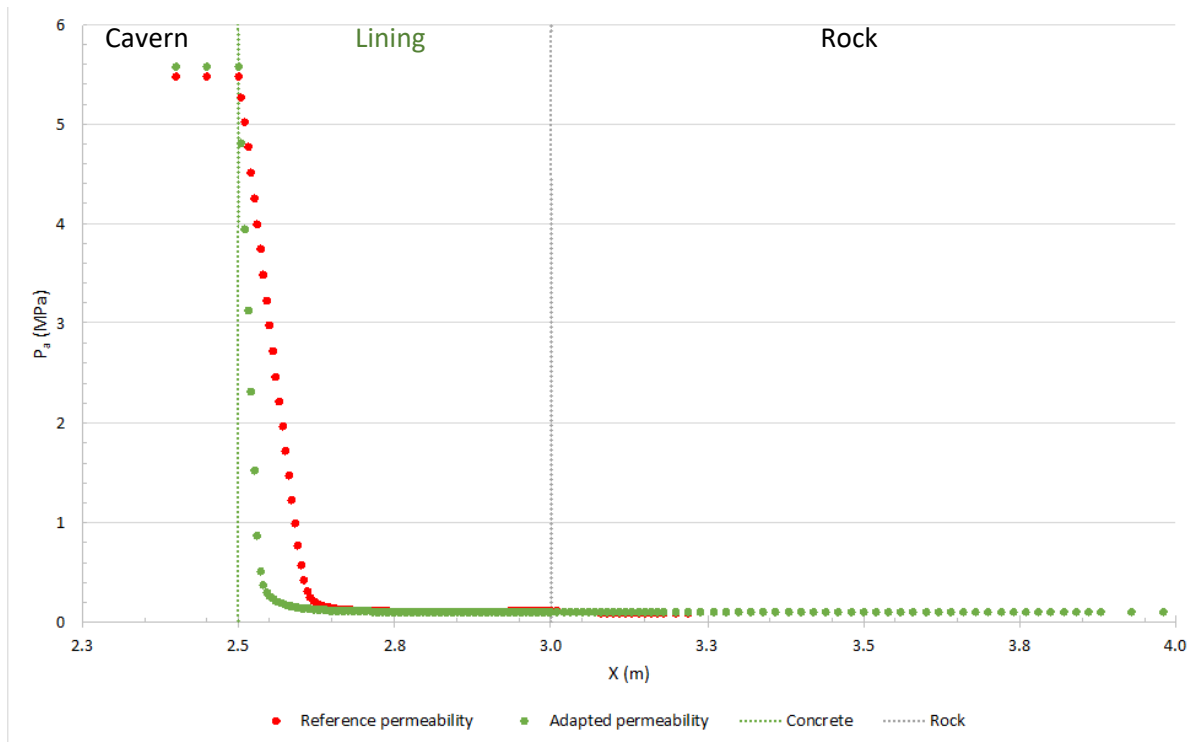


Figure 26 Longitudinal air pressure profile for adapted permeability after the initialisation phase (H).

Figure 26 shows the air pressure profile at the end of the initialisation stage. The results are corresponding to the expectations, in the lining with a lower permeability, the pressure drops much faster. There is a small difference in cavern pressure after the initialisation but the difference is less than 0.1MPa. The fact that the air migrates less into the rock, makes that more air stays in the cavern, causing a slight increase in air pressure.

In Figure 27 the effect on the water pressure after initialisation is immediately visible. In the lining, the water pressure is generally lower due to the lower permeability and has a steep transition. On the other side in the rock with a higher permeability, a higher water pressure is reached. This is due to the boundary condition at 30m which imposed the water to be at a pressure of 1MPa. As the higher permeability facilitates the water flow, a more uniform water pressure in the rock is reached, even if the lining/rock interface was drained to 0.1MPa before. Generally, a higher permeability causes a higher pressure.

The operational phase is again executed for 81 cycles. All graphs show the state at the end of the cycle after the last waiting period.

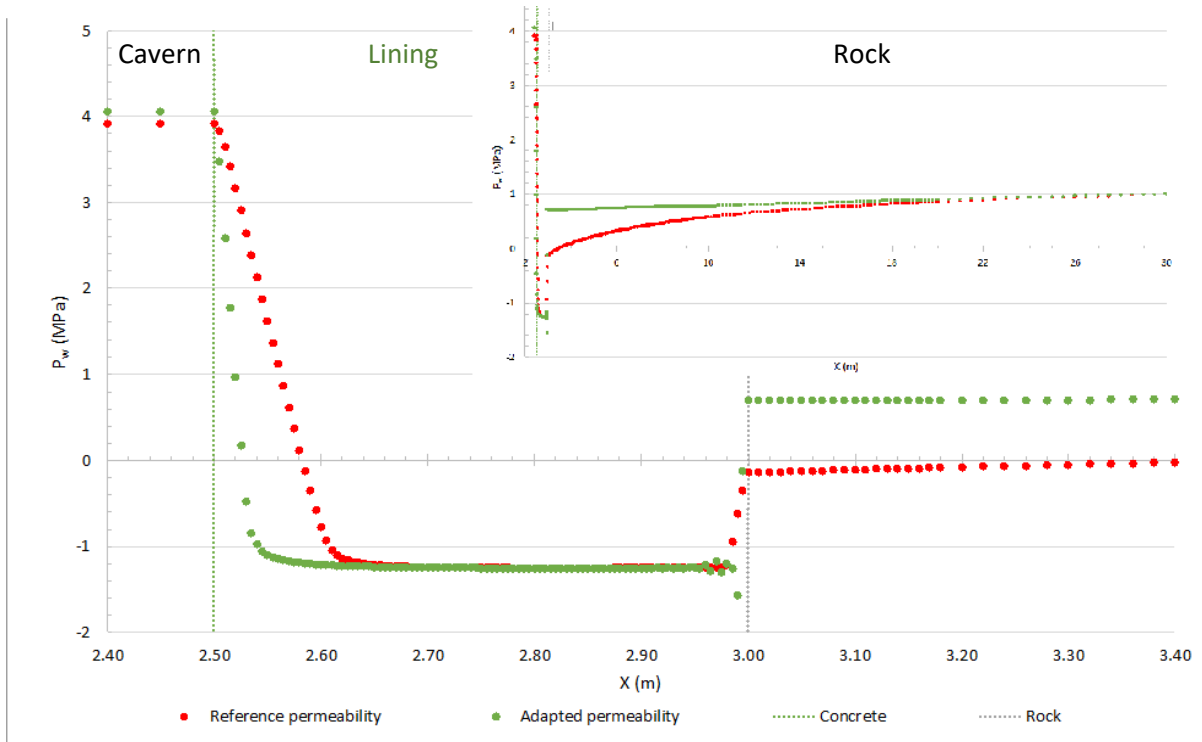


Figure 27 Longitudinal water pressure profile for adapted permeability after initialisation (H).

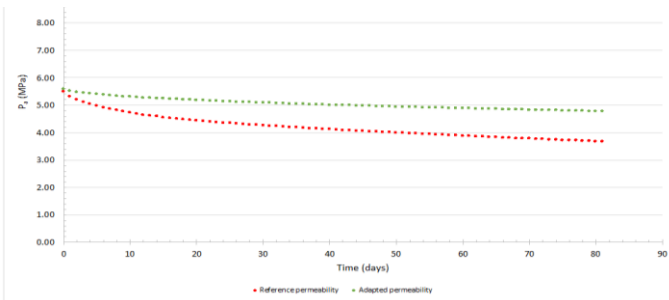


Figure 28 Cavern pressure evolution during CAES-operation at the end of each cycle with adapted permeability (H).

The fact that air migrates slower in the lining has immediate influence on the air pressure during operation. Figure 28 indeed proves that during the operation, the pressure loss is more limited (0.8MPa vs. 1.8 MPa). Figure 29 shows the big influence on the air pressure in the rock. Clearly most of the air leakage, is stored in the lining causing only a slight increase in the rock. This is visible in the sharper and higher peak.

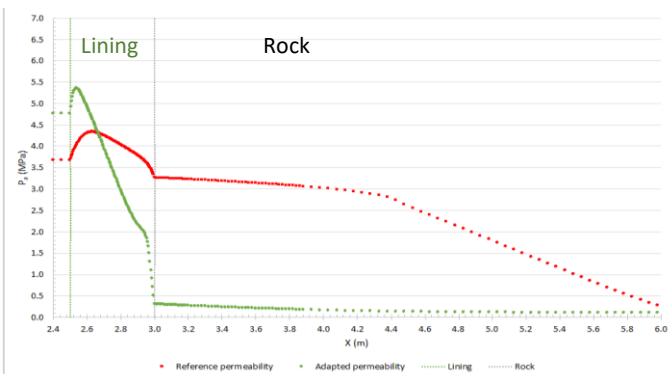


Figure 29 Longitudinal air pressure profile during CAES-operation with adapted permeability at the end of cycle 81.

For the water pressure (Figure 30), the effects on the rock are even greater. Where in the reference case along the whole length the water pressure was influenced, now only in the lining the water pressure is influenced. It takes much more time to compensate the initial negative water pressure, the small peak near the lining-rock interface is due to the start of compensation of the negative water pressure by the water pressure distribution in the rock that is quite rapidly

back at 1MPa. It is assumable that in the next set of cycles this small peak will gradually disappear. For the degree of saturation, there is no visible difference caused by the adapted permeability, the graph is added in Appendix B.

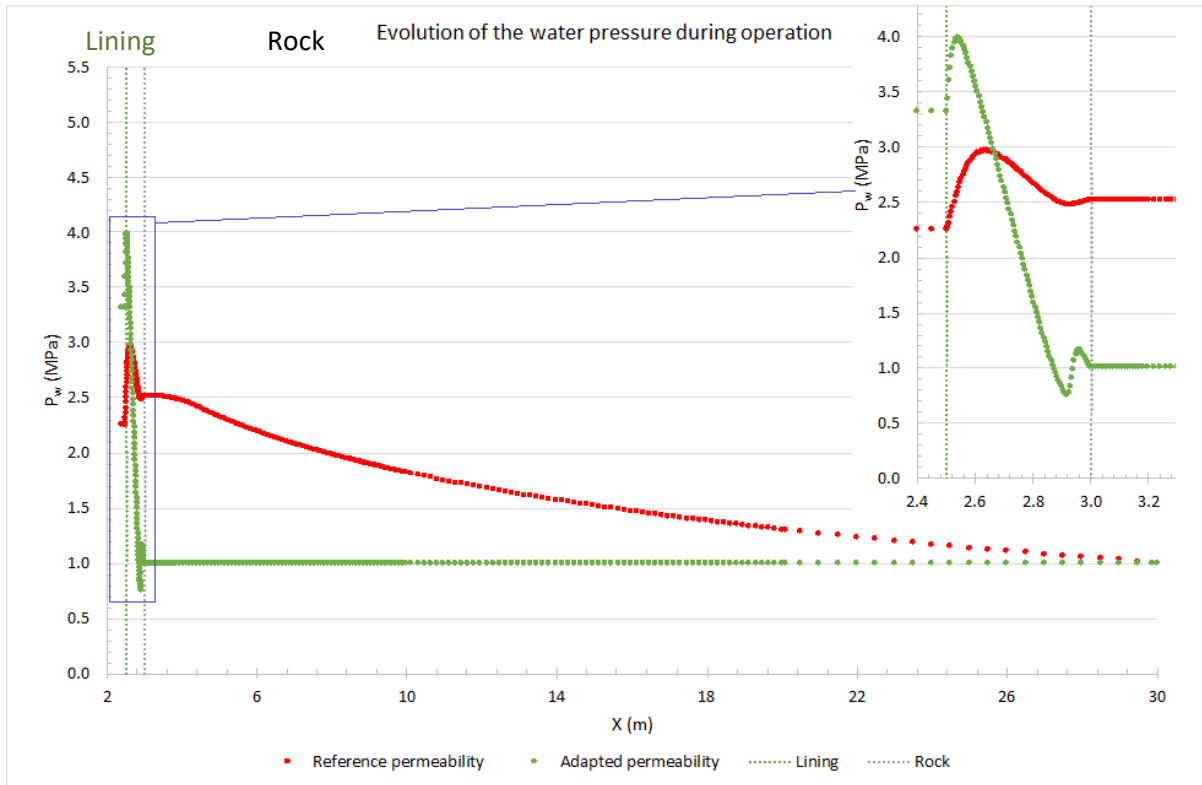


Figure 30 Longitudinal water pressure profile at the end of cycle 81 for the adapted permeability (H).

4.1.2.2.2 Air entry pressure

This chapter deals with a changed air entry pressure (AEP), remember this is not the real air entry pressure but close to it. For this simulation only the value of P_0 has changed. The initial negative water pressure in the lining is not adapted, so this has influence on the saturation in the lining. The following values for air entry pressure are used: 735kPa (reduced), 1.47MPa (reference) and 14.7MPa (increased). Two cases are studied:

- Only AEP of rock is adapted
- AEP of concrete lining and rock is adapted

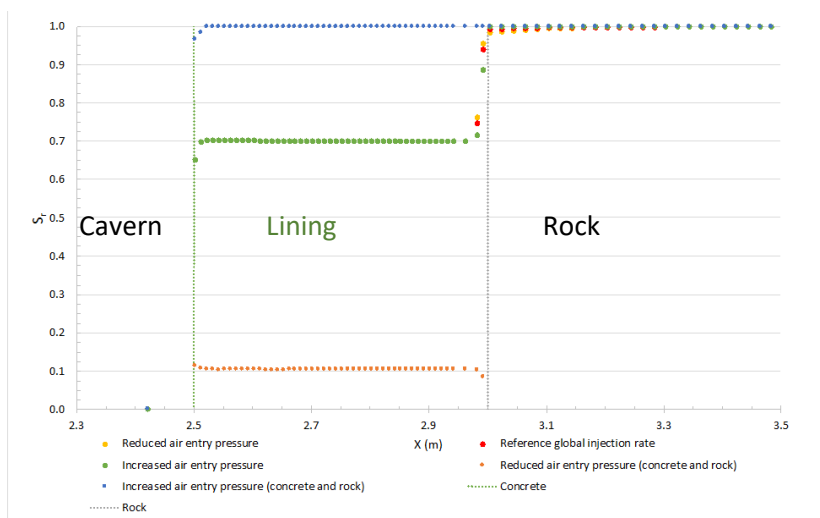


Figure 31 Horizontal degree of saturation profile for different air entry pressures after initialisation (H)

Figure 31 which shows the corresponding degree of saturation immediately shows the influence on the lining. Formerly the lining was at 70% saturation. The lining is only affected if its AEP changes. Due to the increase AEP of the lining, the lining is now still at 100% saturation. On the contrary, for the reduced AEP, the lining is almost completely desaturated.

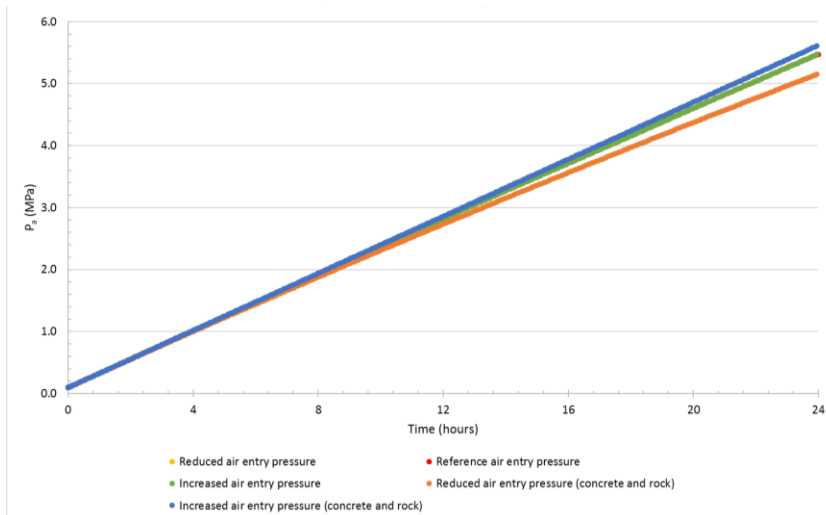


Figure 32 Air pressure in cavern during the initialisation phase for different air entry pressures (H).

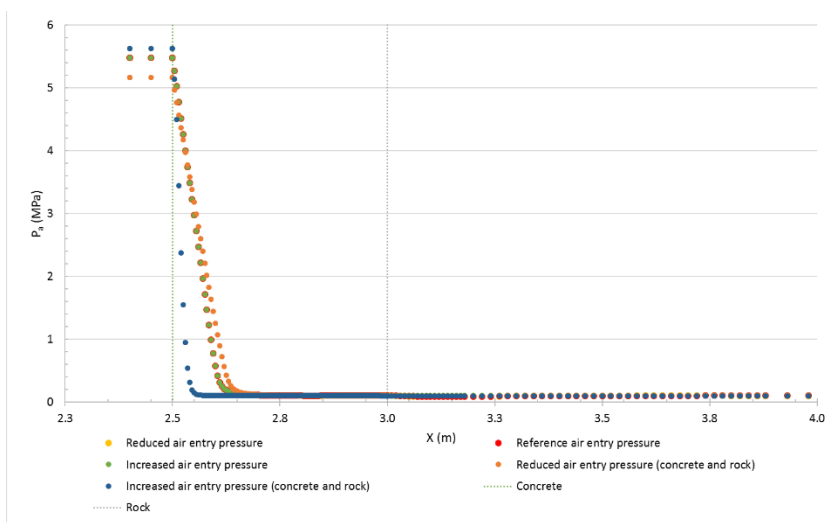


Figure 33 Horizontal air pressure profile after initialisation for different air entry pressure (H).

During the initialisation phase, the cavern pressure in Figure 32 is slightly influenced when the AEP of the rock and concrete is adapted because air migration in the lining is very limited. A reduced air entry pressure causes a lower pressure, what is logical as the air can get easier, earlier and further in the lining and rock (Figure 33). When only the rock is changed of course no difference from the reference case is observed as the air does not yet has migrated to the rock after initialisation.

The first big differences are observed for the water pressure. Figure 34 proves that when only the rock AEP is changed this causes a direct shift of the water pressure in the rock, upwards for reduced AEP.

On the other side, when both the concrete and rock have an increased or decreased AEP, the water pressure generally increases. For the increased AEP in both lining and rock, a big change in the water

pressure in the lining is observed. As the AEP increases the migration decreases. This causes the water to flow easily from the rock into the lining to resaturate the lining and increase the water pressure. This is the first time this is observed in this extent. As previously several times observed, the increase of water pressure due to the migration of air into the lining causes a far higher water pressure increase.

Observations made in the initialisation phase are also valid in the operational phase. The increased AEP in both lining and rock almost has no pressure loss compared to all other cases. Figure 35 also shows that the rock at a reduced EAP does not influence the pressure in the cavern (equals reference case). Thus, this shows the important function and efficiency of the cavern. When both the lining and rock have a reduced AEP, the pressure loss is more than half.

Figure 36 and Figure 37 show the function of the air entry pressure very good. The curve for reduced AEP in the rock shows a lower air pressure in the rock. Which is for the curve with reduced AEP in the lining and rock also the case, including in the lining as air can migrate quite easily. In the case of high AEP in the rock and lining, the air that migrates into the lining causes the highest pressure of all cases in the lining. Because air has difficulties to migrate into the lining, it has also difficulties when migrating

back towards the cavern during withdrawal and waiting periods. However, most of the air does not reach the rock, while all other cases migrate up to 6.5m.

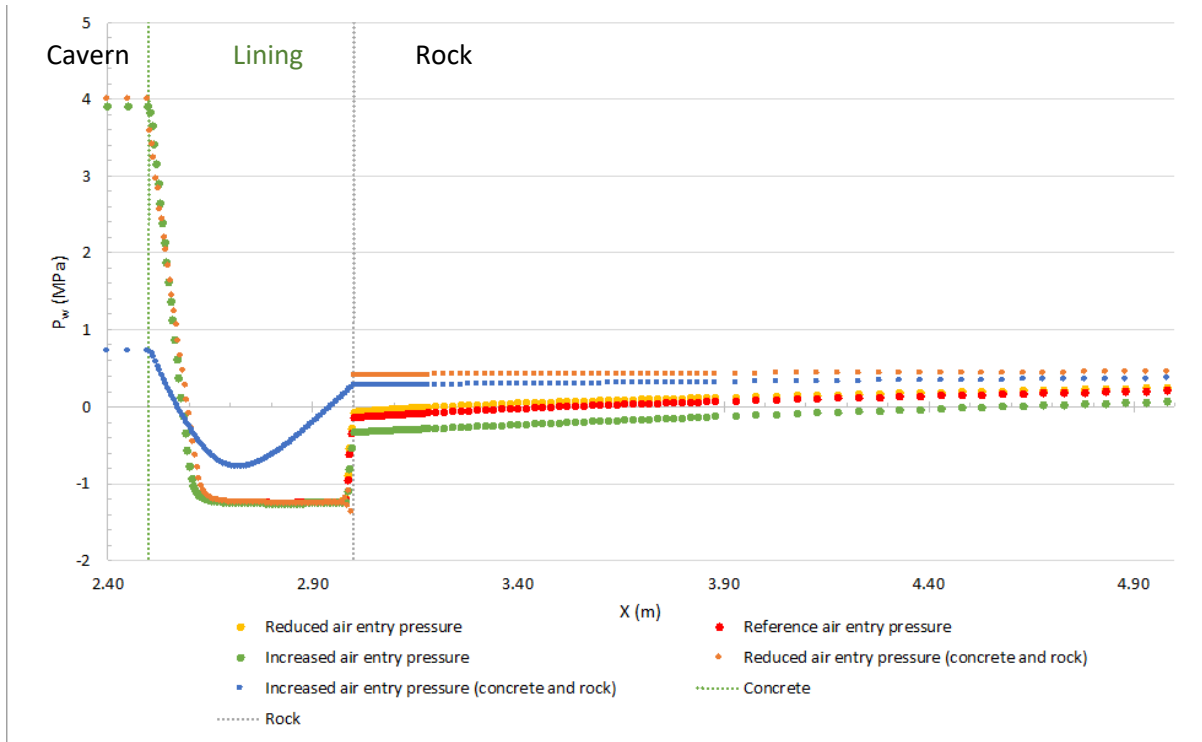


Figure 34 Horizontal water pressure profile for different air entry pressures after initialisation (H).

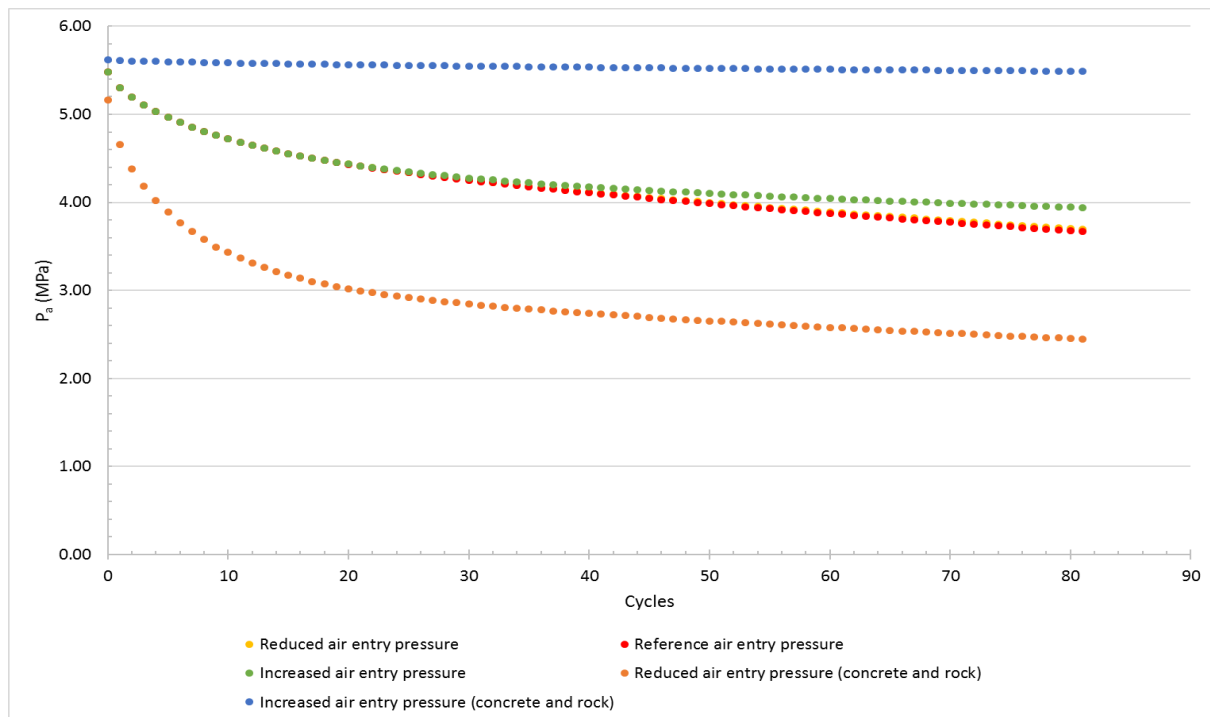


Figure 35 Cavern pressure evolution during CAES-operation for different air entry pressures at the end of each cycle (H).

The curve of increased AEP in the rock on Figure 37 shows the negative effect of a rock with higher air entry pressure than the lining on the water pressure. As it has difficulties to flow into the rock, the water pressure builds-up in the lining. In Figure 36 this is also visible. The air pressure becomes more homogeneous in the lining before it can migrate into the rock which makes that the peak is a very

broad peak covering the lining and a part of the rock. The main problem is that during withdrawal and waiting periods, the air that is in the rock has much more difficulties to go back to the lining and cavern due to the higher air entry pressure.

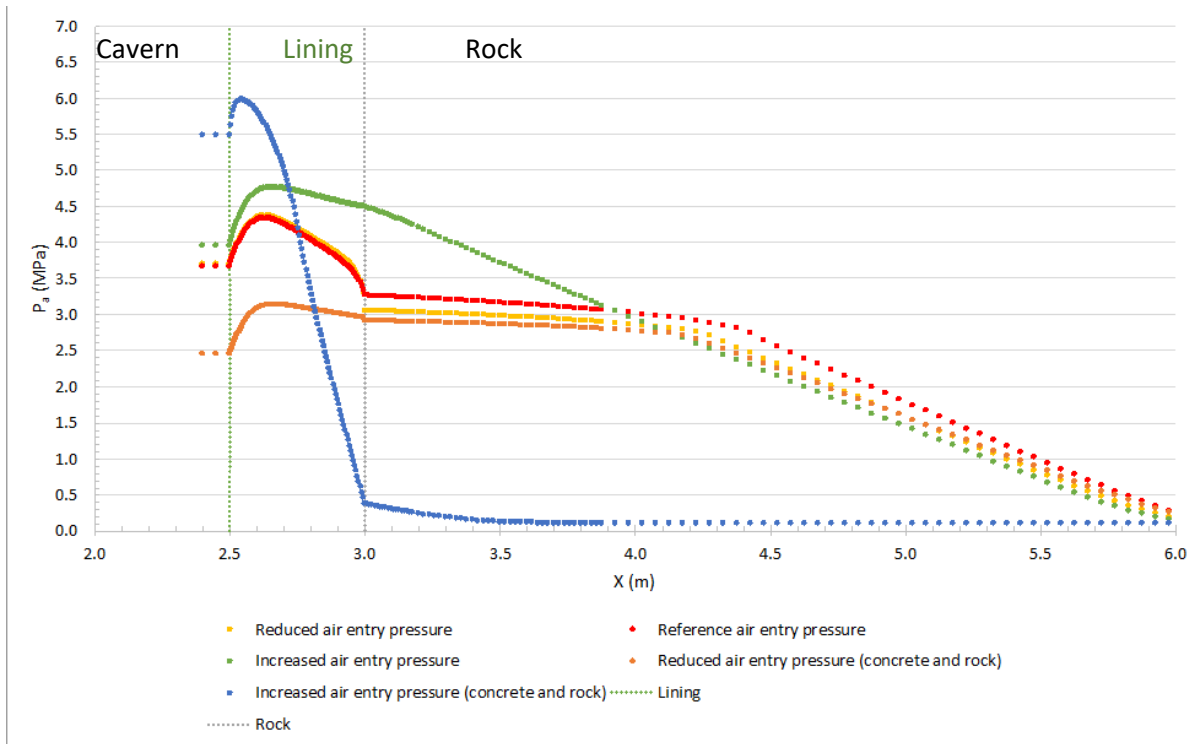


Figure 36 Horizontal air pressure profile at the end of cycle 81 for different air entry pressures (H).

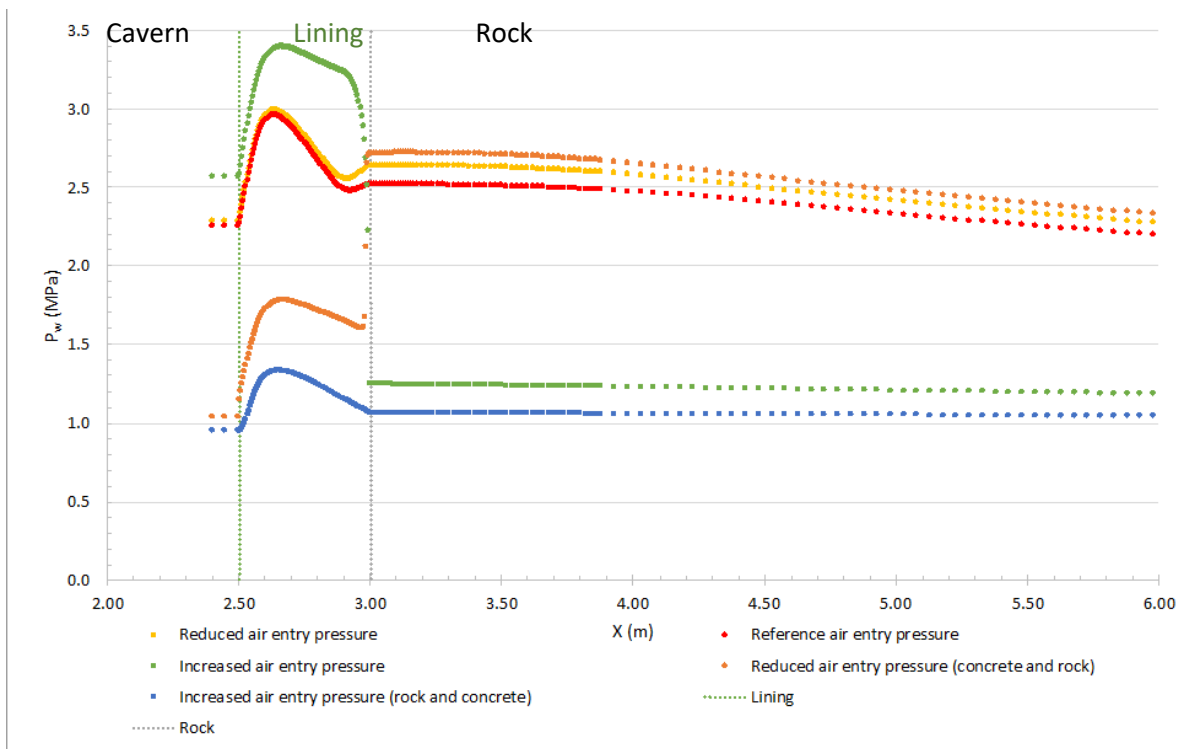


Figure 37 Horizontal water pressure profile at the end of cycle 81 for different air entry pressures (H).

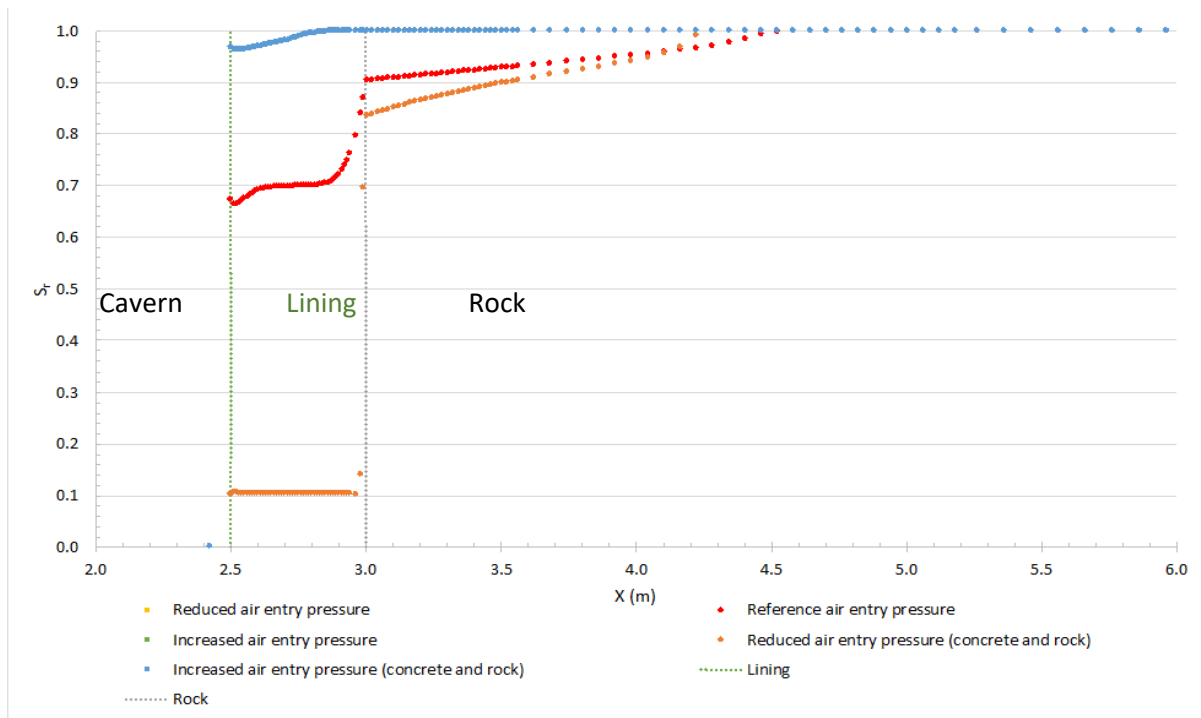


Figure 38 Horizontal degree of saturation profile at end of cycle 81 for different air entry pressures (H).

For the degree of saturation (Figure 38) again no differences for the case where only the rock has an adapted AEP. In the other case, for an overall increase in EAP, the lining slightly starts to desaturate at the end of cycle 81. On the other side the overall reduced EAP causes a bigger desaturation in the rock due to easier air migration.

In conclusion, an overall high air entry pressure in at least the lining is wanted to limit the losses. As the lining forms the main barrier for air leakage, the properties of the rock are less important but the higher air entry pressures for rock do influence positively the leakage. On the other side, when the rock has a lower air entry pressure than the lining, the lining is still able to keep the air as the difference with the reference case is very limited.

4.1.2.2.3 Injection rate

The following chapter deals with the influence of an injection rate that is twice higher or lower. The injection rates used are $3.957 \cdot 10^{-5}$ kg/s (reduced), $7.913 \cdot 10^{-5}$ kg/s (reference) and $15.826 \cdot 10^{-5}$ kg/s (increased). Two cases have been investigated:

- Only the operational phase
- Initialisation + operational phase

The latter case is called global injection rate for further use.

Operational phase

This sensitivity analysis causes only changes in the third operational phase. The excavation and initialisation phase are exactly the same as in the reference case. The results of this simulation lead to the following results for the operational phase:

Due to the fact that only the injection rate of the operational phase is affected, all simulations start at the same pressure. Figure 39 shows the pressure at the end of each cycle. As during this phase, the amount that is injected is also withdrawn, all results are due to the difference in maximum cavern

pressure during a cycle. With a higher injection rate, it is visible that the pressure decrease is higher than with the reference pressure. This is caused by the higher pressure in the cavern, which is also felt in the first elements of the concrete lining. So to speak it is pushing forward the air and compressing the water in the lining, which makes that generally the pressure in the cavern is lower due to higher storage volume in the lining.

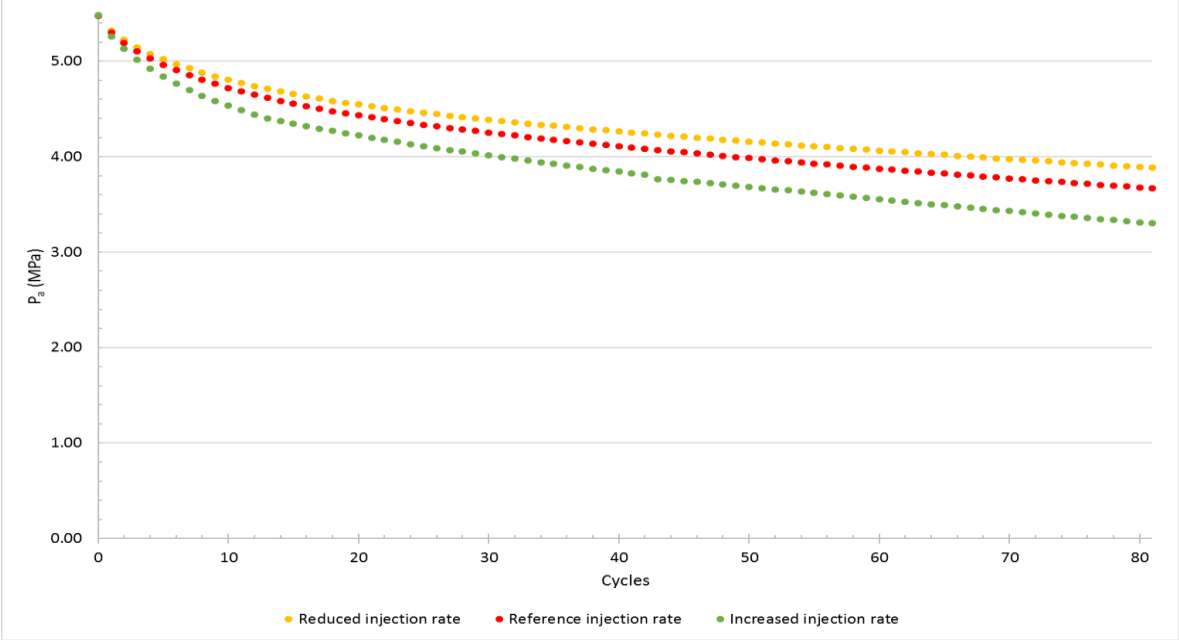


Figure 39 Cavern pressure evolution during the operational phase for different injection rates (H).

For the lower injection rate the inverse is valid, a lower maximum cavern pressure pushes less the air in the rock, leading to lower pressure losses. Figure 40 confirms this reasoning. Between half and twice the injection rate, a more or less constant pressure difference of about 0.5MPa is observed in the lining and rock.

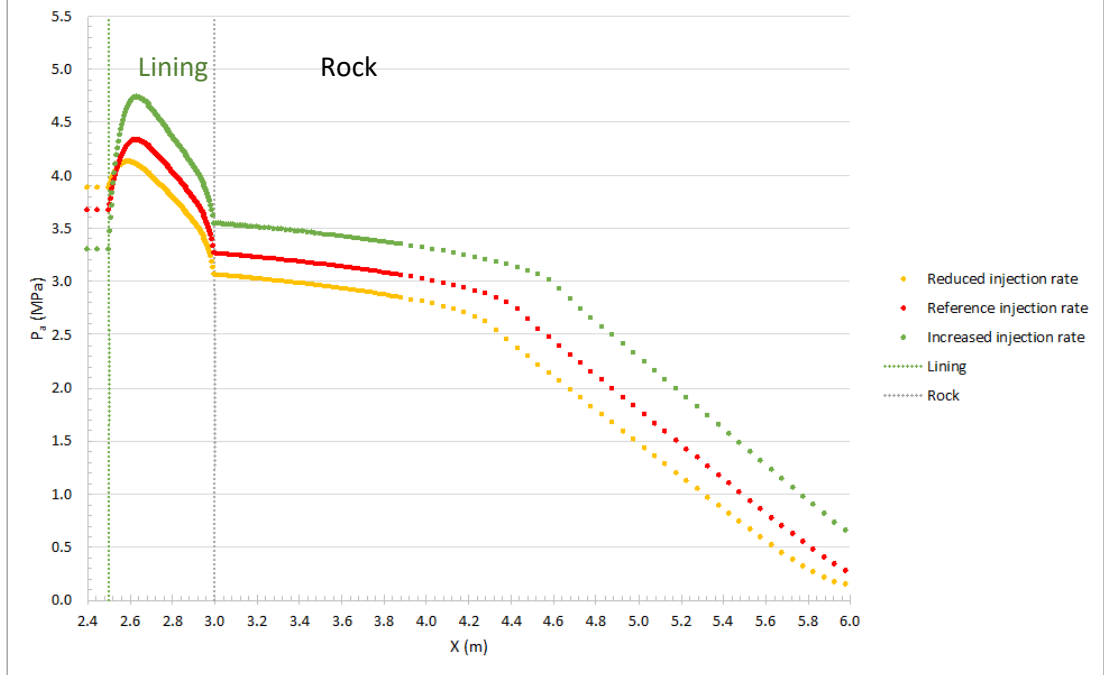


Figure 40 Longitudinal air pressure profile in the operational phase for different injection rates at the end of cycle 81 (H).

For the water pressure between both reduced/increased rate a more or less constant water pressure difference is observed in the rock of around 0.4MPa. In the lining this difference is not constant. The degree of saturation has not changed and is added in Appendix B.

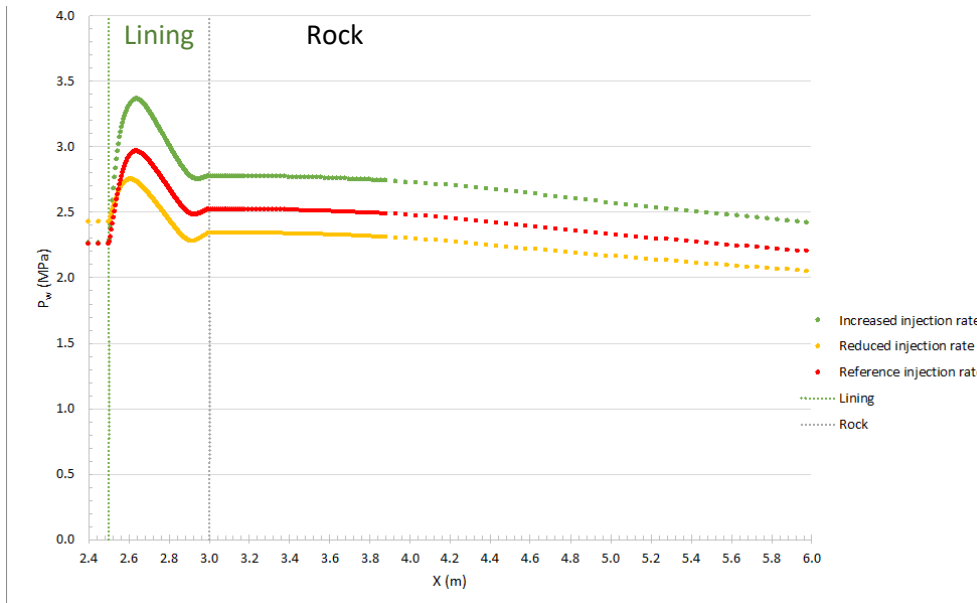


Figure 41 Longitudinal water pressure profile in the operational phase for different injection rates at the end of cycle 81 (H).

In conclusion it can be said that lower injection rate during cycles are more efficient in terms of losses as less pressure is lost but this has immediately an influence on the efficiency of the global energy storage plant as this is not only linked with the leakage but also to the air pressure reached in the cavern as mentioned in Operational phase. Less energy can be recovered because a lower amount of air was injected in the cavern and potentially this air should be recompressed. An equilibrium has to be found between operational conditions and pressure losses. However, the average daily leakage is higher for reduced rates as can be found at the end of the chapter.

Initialisation + operational phase

This simulation also affects the operational phase. Due to the different pressure to start the real CAES-operation, a one-on-one comparison is difficult.

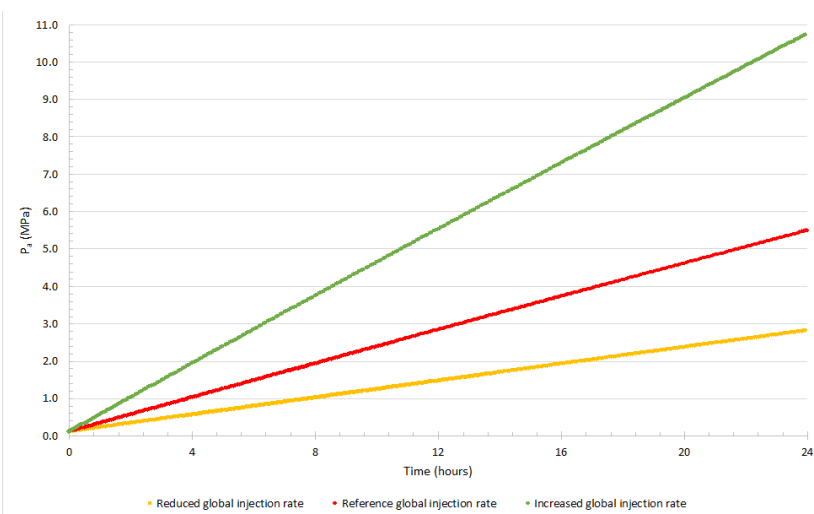


Figure 42 Cavern air pressure evolution during initialisation for different global injection rates(H).

As Figure 42 clearly indicates, the pressure build-up in the cavern stays linear, but the slope depends on the injection rate. The final pressure after 24h is double or half of the reference pressure for increased and reduced injection rate respectively. As Operational phase already proved, the higher cavern pressure causes a deeper migration in the rock.

Figure 42 shows the cavern pressure difference and

evolution of the air pressure in the rock during the initialisation phase. Deeper migration with higher pressures for higher injection rates. Together with Figure 43 it is again observed that the water pressure and air pressure are closely linked. The distance where the air pressure is at the initial condition, there the water pressure is still the initial negative water pressure. The graph starts to show the same phenomenon also seen with the adapted permeability that the negative water pressure is starting to increase on the rock side due to water flows from the rock into the lining.

During the operational phase, the initial pressure is different and a similar but more extreme behaviour in comparison with the previous case is observed.

Where for the increased global injection rate the air pressure almost halves over 81 cycles, the reduced global injection rate only drops 25% (Figure 44). Regarding the migration into the rock (Figure 45), the latter case does not migrate as far as in the previous chapter. So the base pressure also plays an important role regarding migration in the rock.

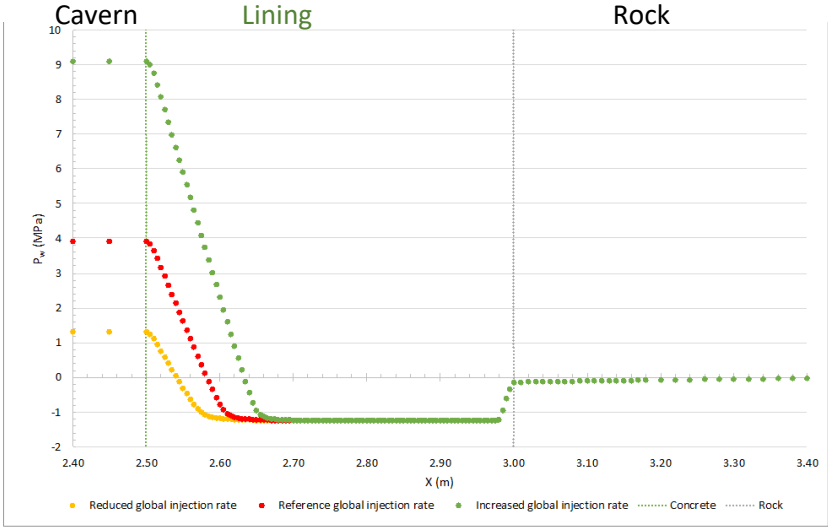


Figure 43 Horizontal water pressure profile after initialisation for different global injection rates (H).

Where in the previous chapter, with the higher base pressure of 5.5MPa the air pressure was adapted to just over 6m from the cavern center. The case in this chapter with a lower base pressure of 2.75MPa has influence to just under 5m from the cavern center.

Figure 46 shows that the water pressure in the lining for the reduced injection rate is more changing due to water inflow from the rock to

the lining than with the other injection rates. This is due to the fact that the lower air pressure compresses the water less.

In Appendix B the full horizontal profile for the water and air pressure is added. Again no difference is observed in the degree of saturation, the graph of the initialisation and operational phase also are added.

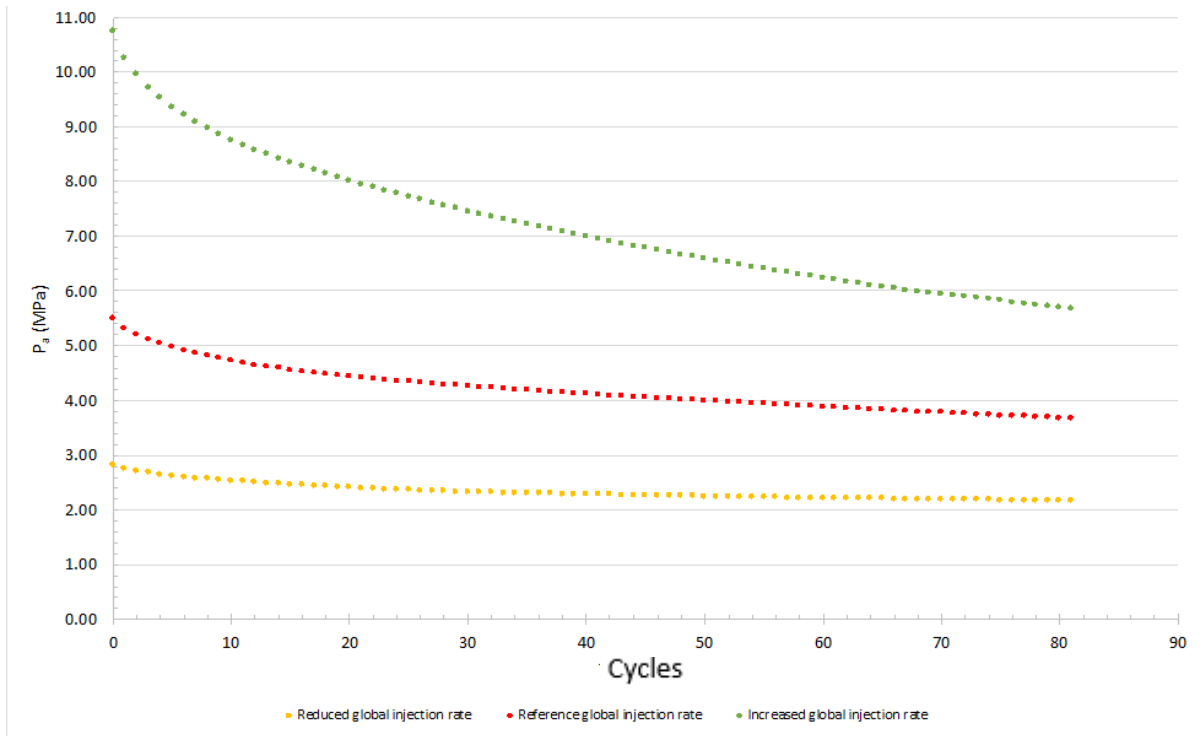


Figure 44 Evolution of the cavern pressure during CAES-operation for different global injection rates at the end of each cycle (H).

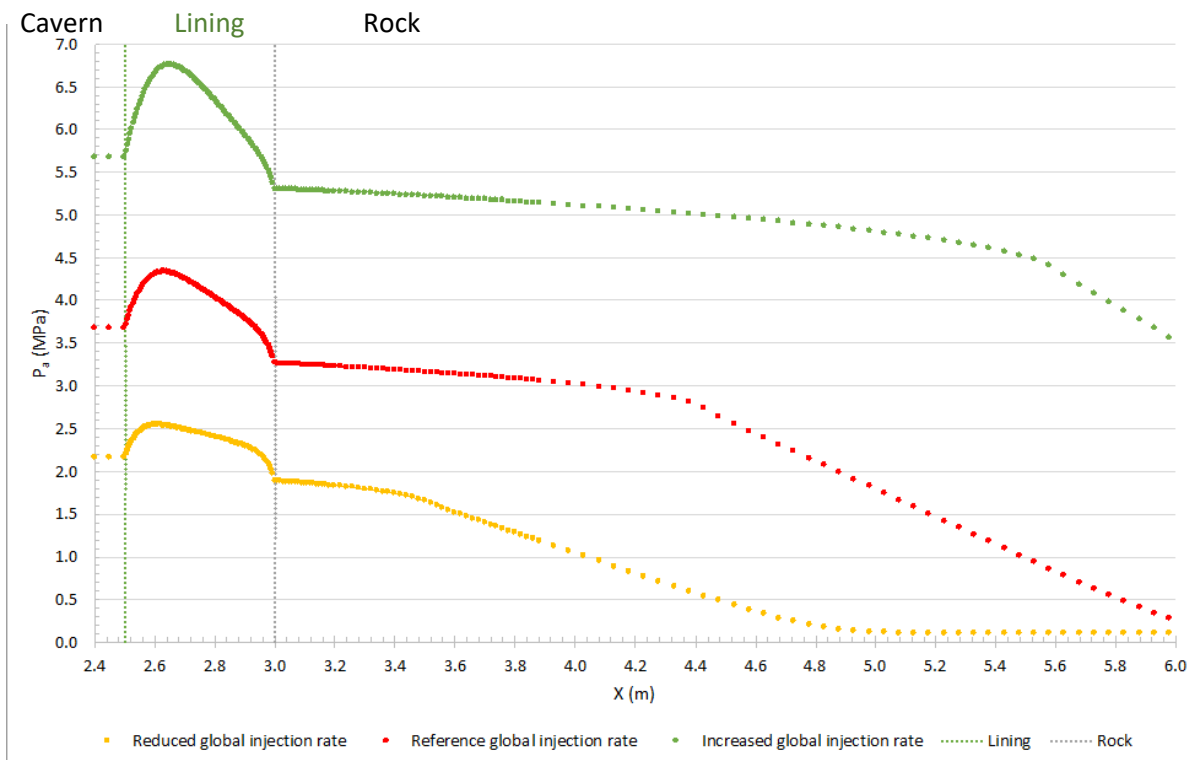


Figure 45 Horizontal air pressure profile at the end of cycle 81 for different global injection rates (H).

In conclusion a compromise has to be made between air loss and efficiency.

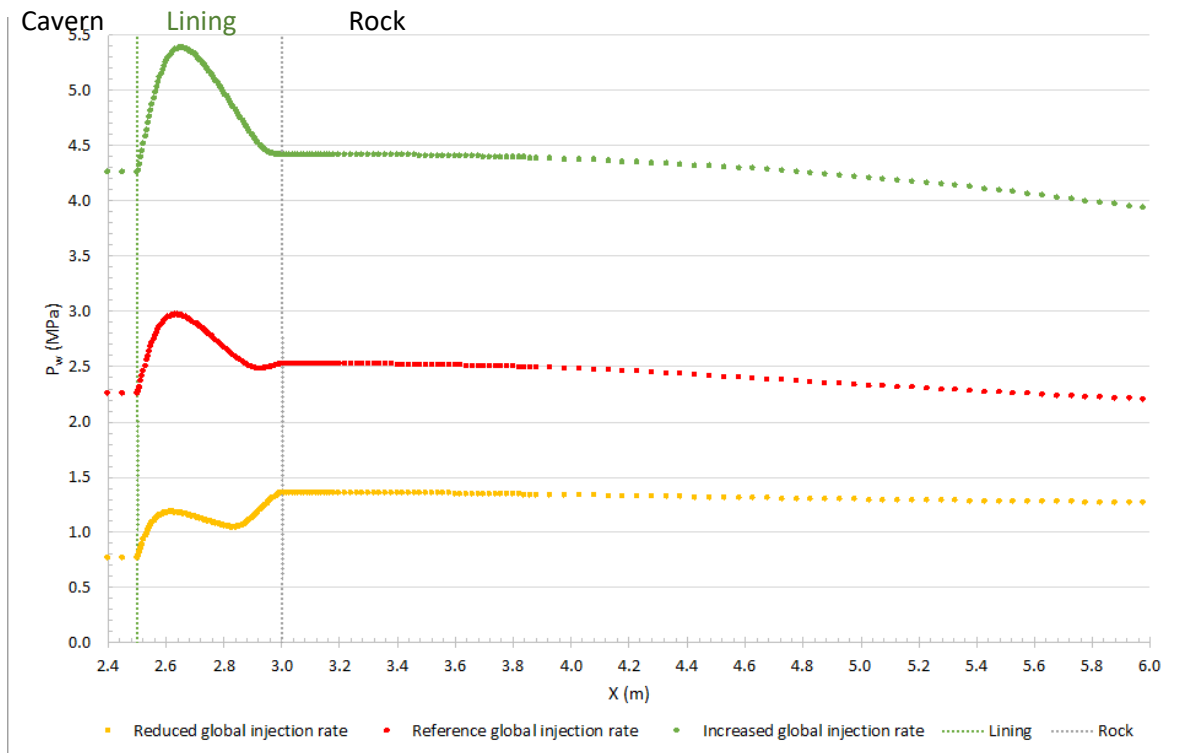


Figure 46 Horizontal water pressure profile at the end of cycle 81 for different global injection rates (H).

4.1.2.3 Leakage

Table 6 Leakage for all hydraulic simulations.

Leakage (%)	Reduced	Increased
Reference	0.857	-
Intrinsic permeability	0.390	-
Operational injection rate	1.505	0.514
Global injection rate	0.612	1.203
Air entry pressure (rock)	0.845	0.713
Air entry pressure (lining and rock)	1.159	0.065

These leakages can be compared to the unlined case which had a leakage of 1.18%. A reduced operational injection rate, an increased global injection rate and a reduced air entry pressure in the lining and rock cause higher leakage. Leakage can be prevented by choosing a high air entry pressure for both the lining and the rock. For the base pressure, the reference injection rate is advised. During operation a higher injection rate, causes lower leakage and is able to store more energy. This is positive for the overall efficiency.

In the case the cavern base pressure has dropped too much, it is possible to add a temporary injection period in order to restore the base pressure in the cavern.

4.2 Thermo-hydraulic model

In this chapter the effects of injecting air at a temperature different from the initial temperature of the surrounding rock is investigated because the model stands closer to reality. The temperature is only at the side of the cavern imposed during injection. For the reference, the air injection temperature is set at 21°C. Due to the ideal gas law, a temperature rise causes a pressure increase if the volume remains constant. The fluid flows are expected to increase as they are enhanced by convection (thermal flow) in combination with a fluid dilation due to temperature increases.

The warm air is only injected during the CAES-operation. This means that during the excavation and the initialisation, the temperature remains fixed in the model, which makes that only the results of the last operational phase are discussed as the excavation and the initialisation are an exact copy of the hydraulic graphs. This choice was made to have only the temperature effects of the daily cycle operation. During initialisation air is still injected with a temperature of 13°C. This is only needed to be able to perform the daily operation as a certain base pressure is needed.

4.2.1 Thermal reference case

The reference case injects air with a temperature of 21°C, which is imposed during injection periods at the cavern side wall.

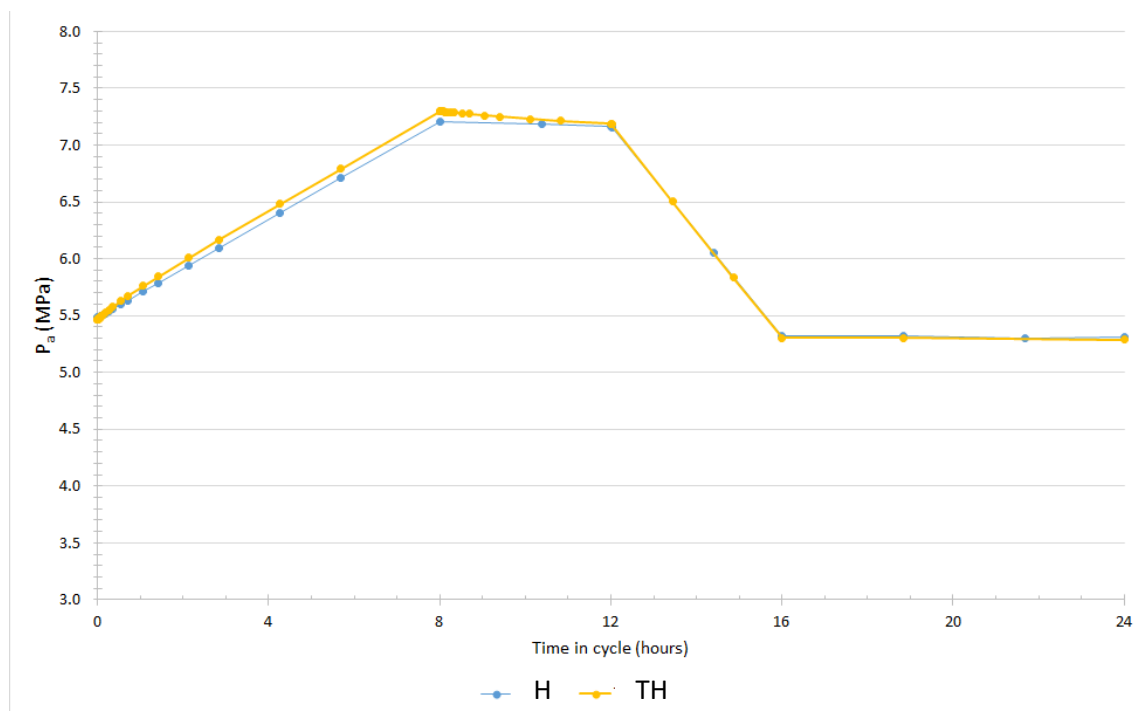


Figure 47 Cavern air pressure envelop for the first cycle of the hydraulic and thermal case (TH)

In Figure 47 the envelop of the first thermal cycle is plotted. As is visible the cavern pressure is slightly higher in the thermal case. Figure 48 shows the temperature evolution in the cavern during the first thermal cycle for cavern side and the middle of the cavern. The middle of the cavern only reaches maximum about 290K. During injection, the temperature increases. This temperature rise causes a pressure increase according to the ideal gas law.

$$\frac{P_1}{T_1} = \frac{P_2}{T_2}$$

In this case the pressure increase is related to the temperature in the middle of the cavern which is more or less the mean temperature in the cavern. If 1 stands for $t=0$ and 2 stands for $t=8h$, this leads at the end of injection ($t=8h$) to $P_2 = 7.395MPa = P_1 * \frac{T_2}{T_1} = P_1 * \frac{290K}{286K} = 1.014P_1 = 1.014 * 7.295MPa$. Figure 48 shows that directly after the injection the temperature starts to decrease. The cavern exchanges its heat with the surrounding lining to come back at an equilibrium temperature. This temperature decrease continues during the withdrawal of the air, until the temperature reaches a minimum at the end of the withdrawal. It is from this point that the side and middle of the cavern have about the same temperature. The next 8h resting the temperature gradually increases back to the initial temperature by heat exchange with the lining.

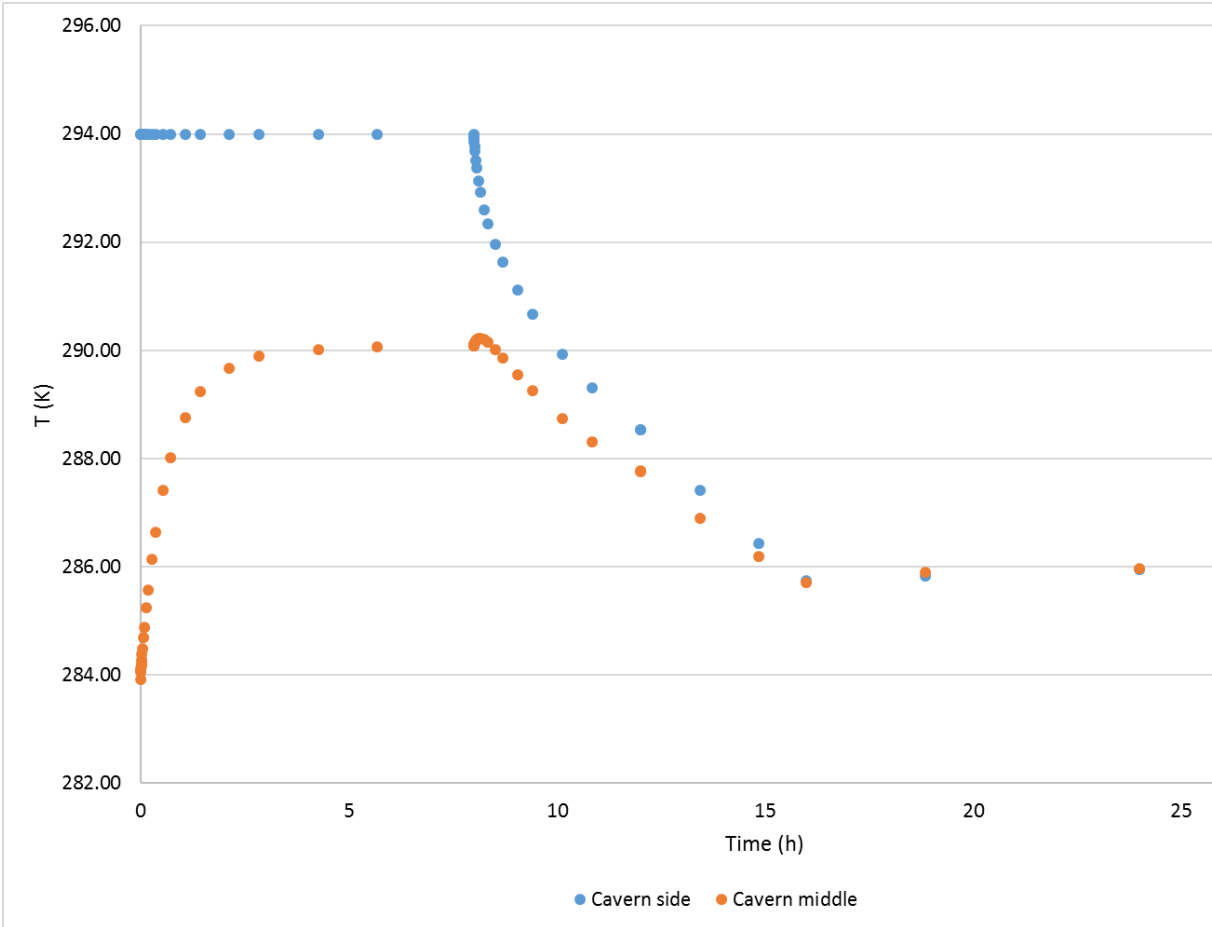


Figure 48 Temperature evolution in the cavern for the first thermal cycle at the cavern side and cavern middle (TH).

Figure 49 shows the steady increase in the lining and rock temperature for increasing number of cycles after the last waiting period of a cycle. Figure 50-Figure 53 show almost exactly the same as the graphs for the hydraulic reference case (Figure 20-Figure 25). The air pressure variations are much less than 0.1MPa. The small water pressure variation is due to the air pressure ones. Generally, the difference in water pressure is smaller than the air pressure. As this is the case for all simulations, the graphs are shown but not discussed.

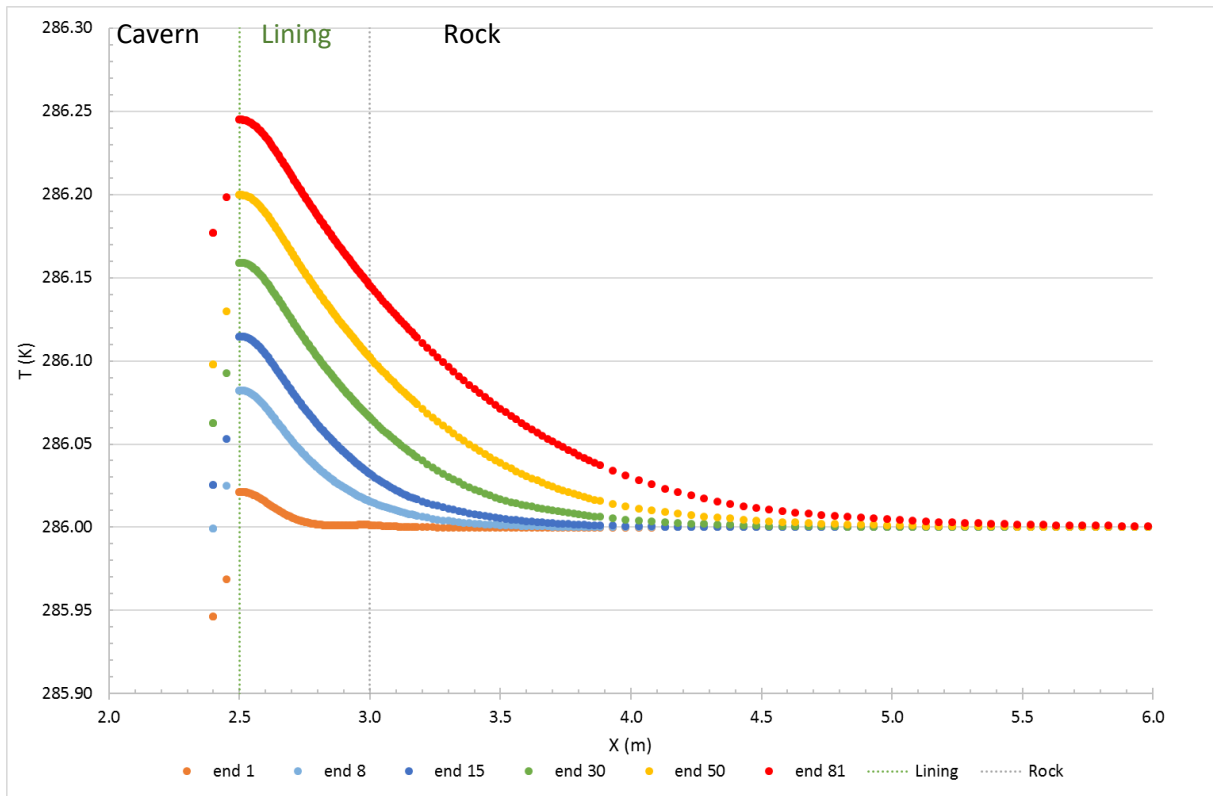


Figure 49 Horizontal temperature profile during CAES-operation for different cycles in end-state (TH).

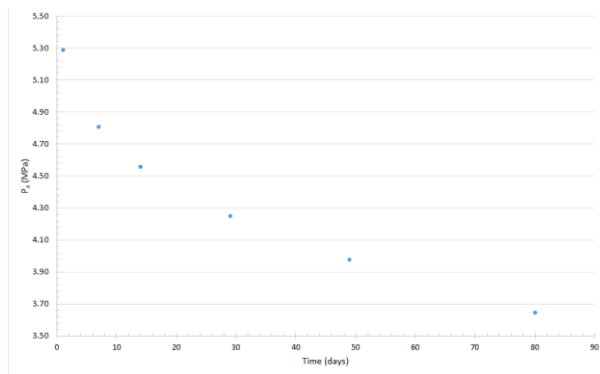


Figure 50 Cavern pressure evolution at the end of each cycle during CAES-operation (TH).

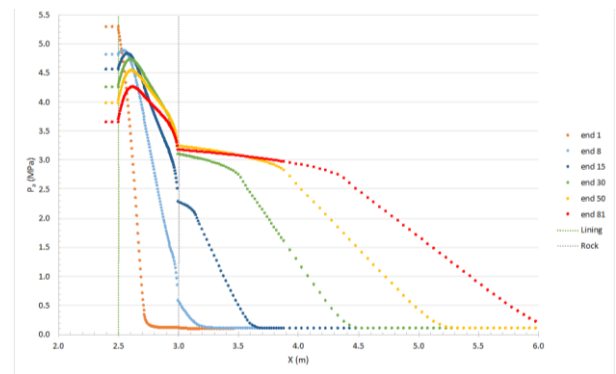


Figure 51 Horizontal air pressure profile during CAES-operation for different cycles end-state (TH).

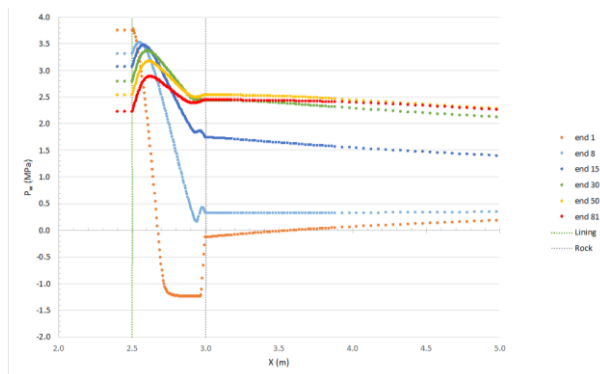


Figure 52 Horizontal water pressure profile during CAES-operation for different cycles end-state (TH).

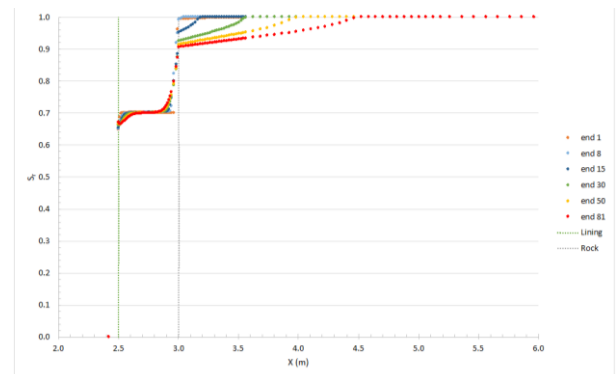


Figure 53 Horizontal degree of saturation profile during CAES-operation for different cycles end-state (TH).

4.2.2 Sensitivity analysis

4.2.2.1 Increased injection temperature

The injection temperature is now 50°C, the reference case (21°C) situation is also plotted for comparison. This higher temperature was chosen as less cooling is needed and causes a pressure increase of 0.5MPa for the maximal cavern pressure after injection compared to the reference case. The main difference is observed in the temperature profile in the concrete lining and rock. Figure 54 shows that the temperature in the lining is 1°C to 0.5°C higher than the reference case at the end of cycle 81. The higher injection temperature mainly causes a slight temperature increase in the concrete lining and rock which influence goes further than in the reference case. The higher temperature in the rock and lining causes directly a small pressure increase in the water and air pressure profile (Figure 56 & Figure 57). For the degree of saturation, no difference is observed (Figure 58). This immediately indicates that the coupling between temperature and pressure is very low. The main pressure differences are due to the injection and the corresponding fluid flows. These flows are affected by temperature changes but to a very limited extent.

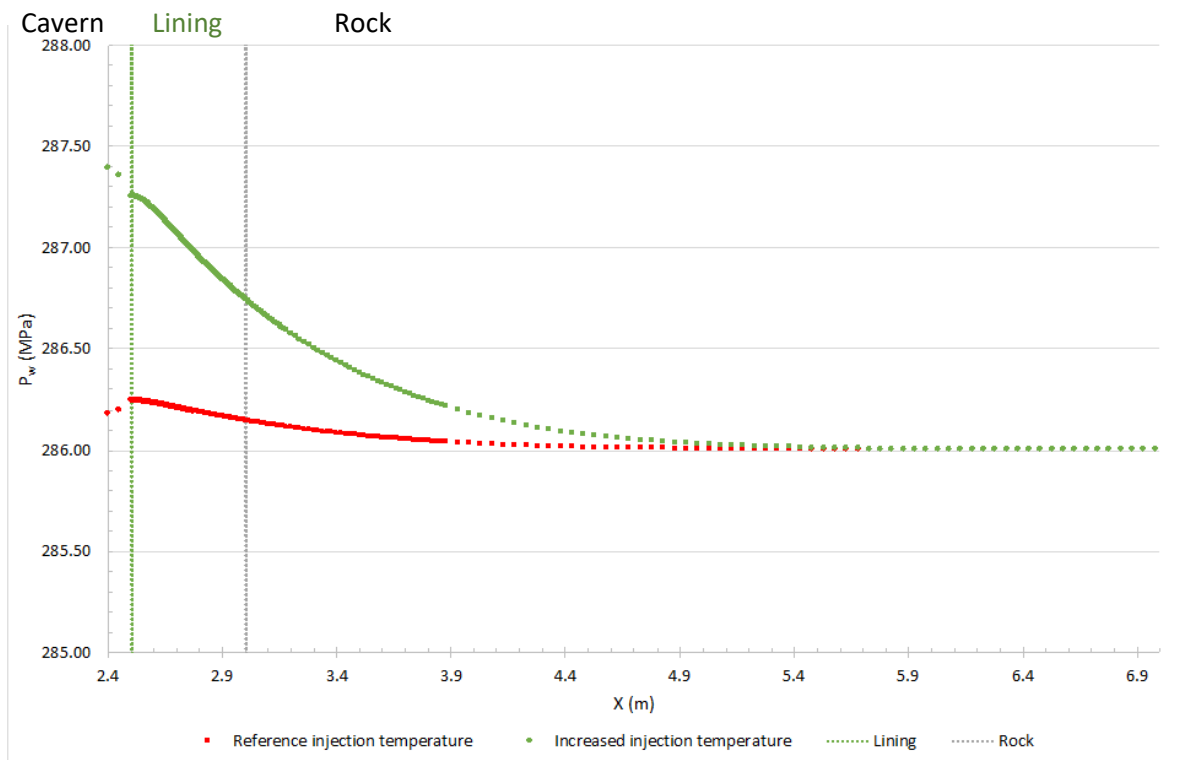


Figure 54 Horizontal temperature profile during CAES-operation at the end of cycle 81 for different injection temperatures (TH).

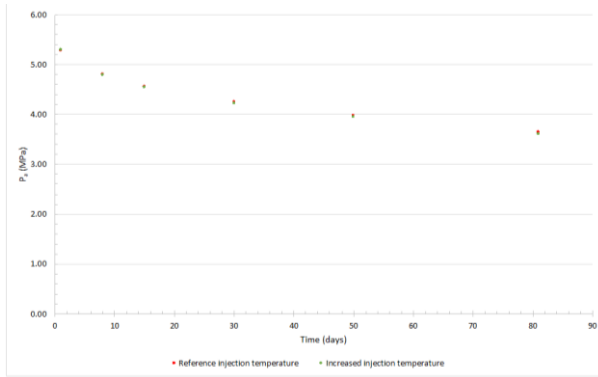


Figure 55 Cavern pressure evolution at the end of each cycle during CAES-operation for different injection temperatures (TH).

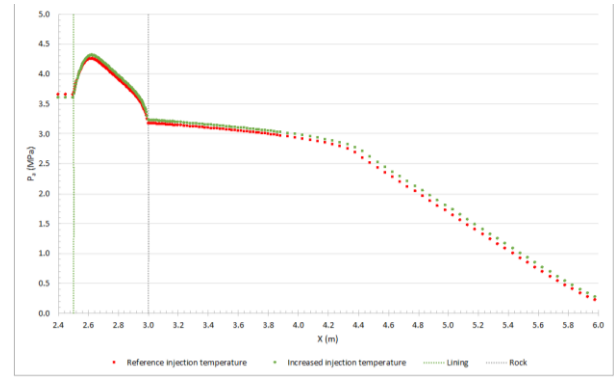


Figure 56 Horizontal air pressure profile during CAES-operation at the end of cycle 81 for different injection temperatures (TH).

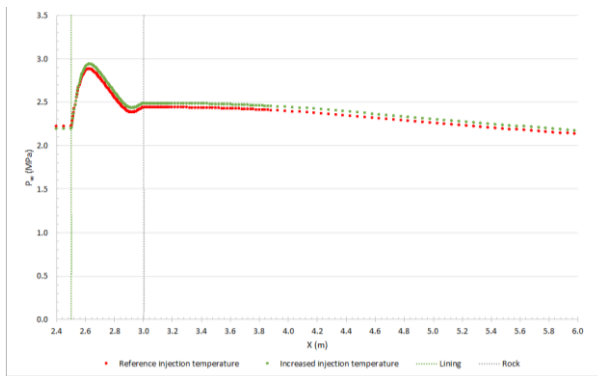


Figure 57 Horizontal water pressure profile during CAES-operation at the end of cycle 81 for different injection temperatures (TH).

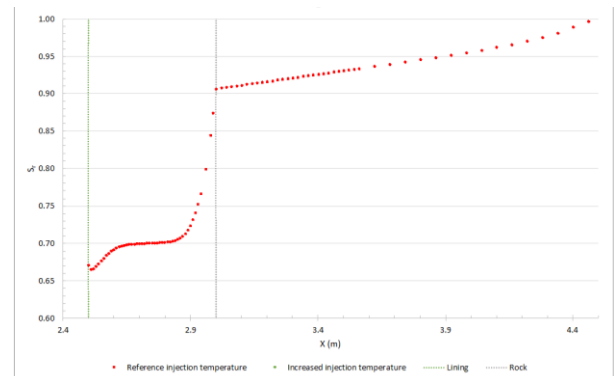


Figure 58 Horizontal degree of saturation profile during CAES-operation at the end of cycle 81 for different injection temperatures (TH).

4.2.2.2 Injection temperature imposed at whole cavern

In this case the injection temperature of 21°C is not only imposed on the outside of the cavern, but on all the cavern nodes. This makes that the cavern is directly uniform at 21°C when injecting. This case is not realistic as in reality the temperature rises steadily during the 8h injection period.

Figure 59 shows the difference in temperature profile at the end of cycle 81 for imposing the injection temperature at the side and the whole cavern. Clearly, when the cavern is directly homogeneous at 21°C, the lining also has a higher temperature between 20°C and 18°C in this case. The conductivity and the thermal convectivity by the air and water flows cause an increase in temperature much further in the rock than all previous cases. Figure 60 confirms again that due to the temperature increase in the cavern, which is now constant at 21°C during injection, the pressure increases accordingly with the ideal gas law. A 3.5% increase in maximal cavern pressure is now obtained in consideration of a 1.4% increase in the reference case. Thus, a faster warm-up of the cavern has a slightly higher coupling between the temperature and pressure as the thermal flows gain a little of importance. Figure 60 shows that the loss of pressure is the same for each cycle at the end of it.

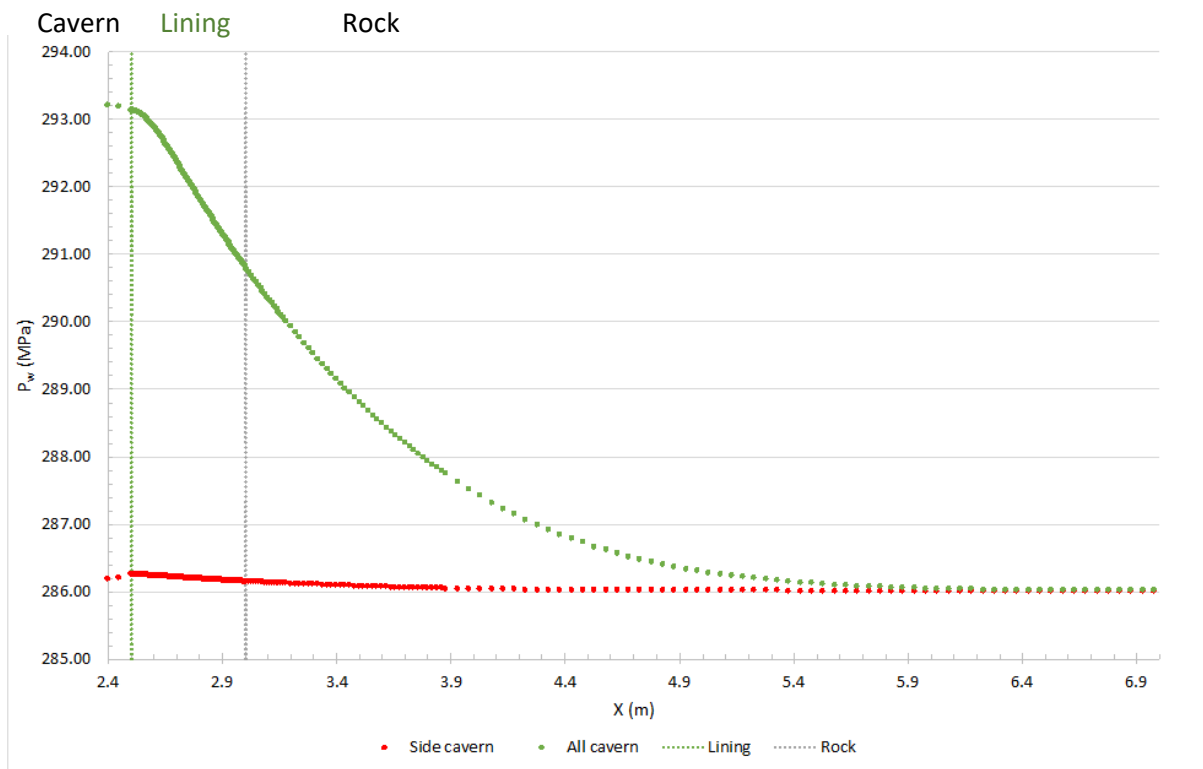


Figure 59 Horizontal temperature profile during CAES-operation at the end of cycle 81 for different injection modes (TH).

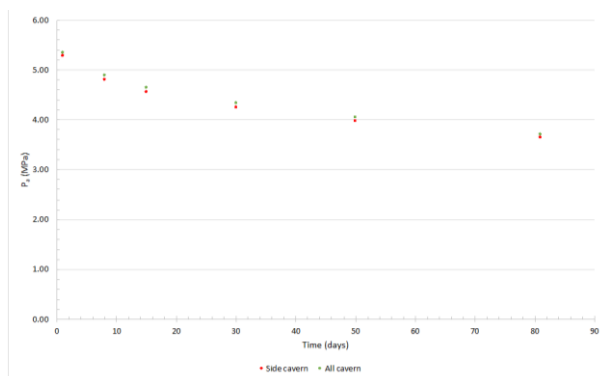


Figure 60 Cavern pressure evolution at the end of each cycle during CAES-operation for different injection modes (TH).

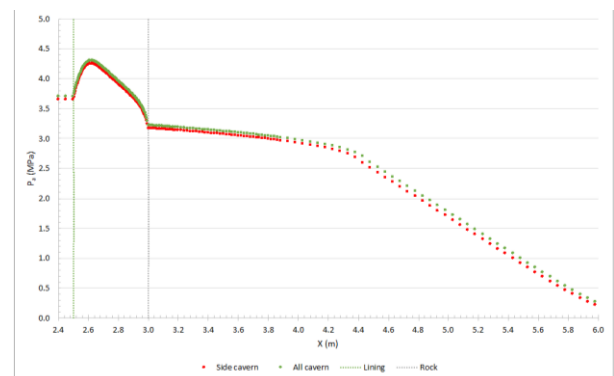


Figure 61 Horizontal air pressure profile during CAES-operation at the end of cycle 81 for different injection modes (TH).

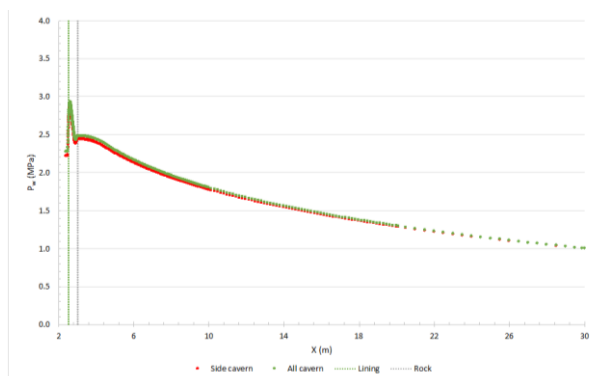


Figure 62 Horizontal water pressure profile during CAES-operation at the end of cycle 81 for different injection modes (TH).

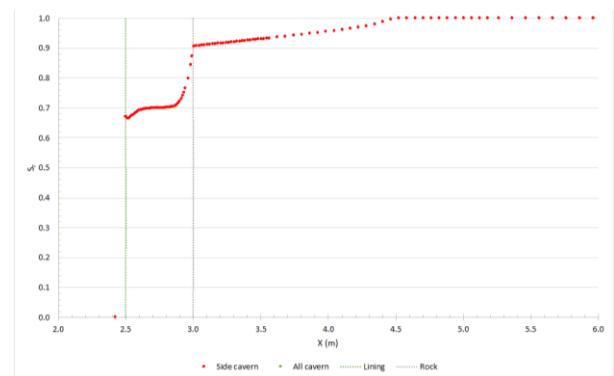


Figure 63 Horizontal degree of saturation profile during CAES-operation at the end of cycle 81 for different injection modes (TH).

4.2.2.3 Cavern thermal conductivity

In this part of the sensitivity analysis, the thermal conductivity of the cavern has been increased to the one of water and the one of rock which are one and two orders of magnitude larger than the one of air respectively.

Table 7 Cavern thermal conductivity sensitivity analysis: changed parameter.

	Water parameter	Reference parameter	Rock parameter
Thermal conductivity applied in cavern (W/mK)	0.58	0.0257	2.637

As thermal conductivity is an important parameter in the heat transfer, it is expected to have a quite large effect. Figure 64 shows the large differences in temperature distribution at the end of cycle 81. The higher the thermal conductivity of the cavern, the higher the temperature in the cavern is at the end of each step. Also during a cycle, the cavern heats up faster and more homogeneous. The rock thermal conductivity causes an air pressure increase with a factor of about 1.02 due to the different temperatures in the cavern. When the water thermal conductivity is used, this factor is slightly smaller with 1.01. Again the low coupling between the pressure and temperature is proven. The horizontal pressure profile is quite constant. Only where the temperature is different, the air pressure follows accordingly (Figure 65).

Figure 65 shows that there is no impact on the loss of air mass. Due to the difference in temperature this will have a small impact on the leakage as the temperature is a parameter in the leakage calculation. Figure 66 and Figure 67 show that the same horizontal pressure profiles are obtained at the end of cycle 81.

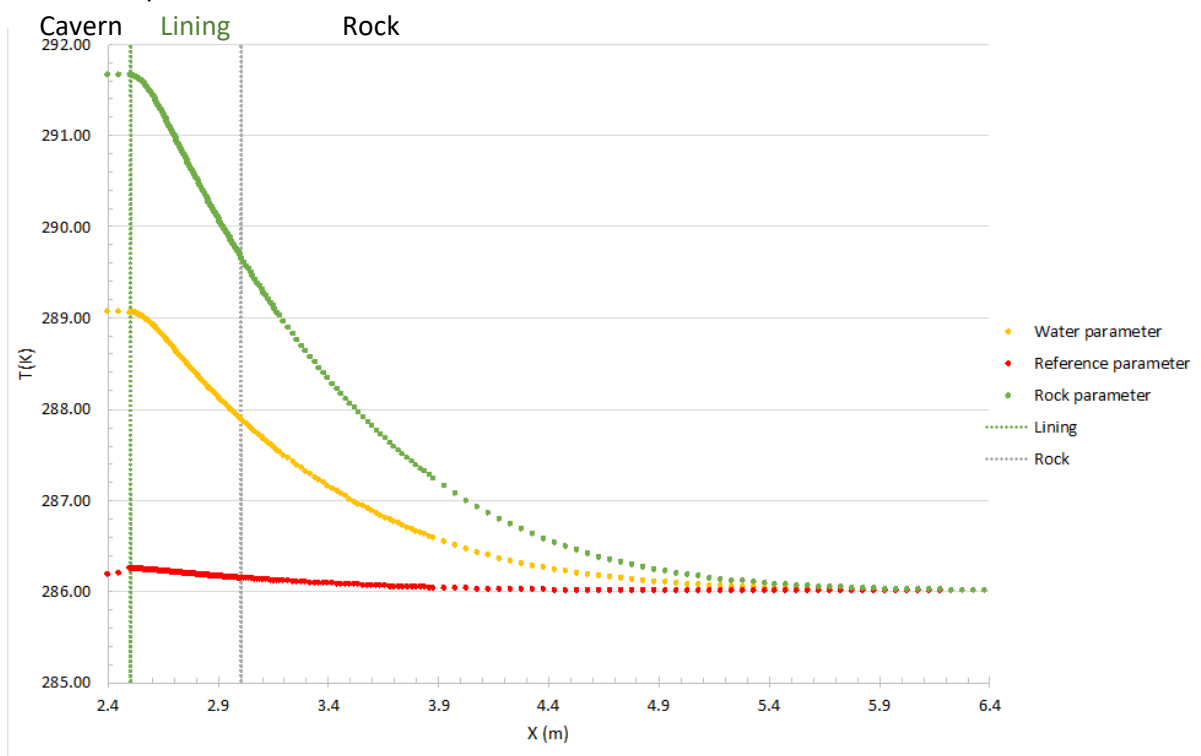


Figure 64 Horizontal temperature profile during CAES-operation at the end of cycle 81 for different thermal conductivities of the cavern (TH).

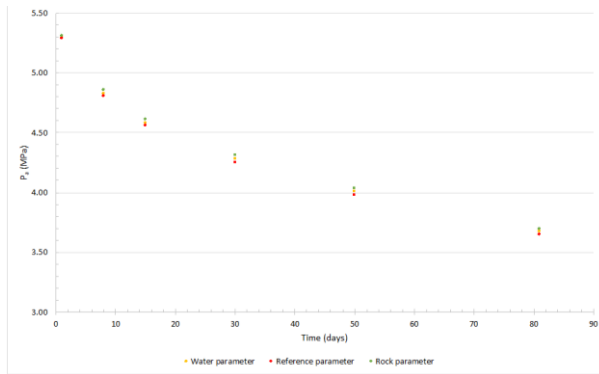


Figure 65 Cavern pressure evolution at the end of each cycle during CAES-operation for different thermal conductivities of the cavern (TH).

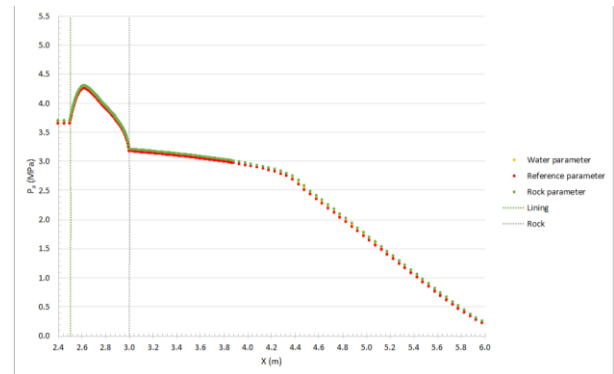


Figure 66 Horizontal air pressure profile during CAES-operation at the end of cycle 81 for different thermal conductivities of the cavern (TH).

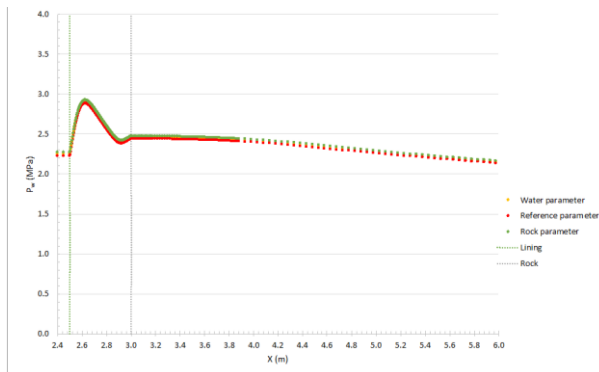


Figure 67 Horizontal water pressure profile during CAES-operation at the end of cycle 81 for different thermal conductivities of the cavern (TH).

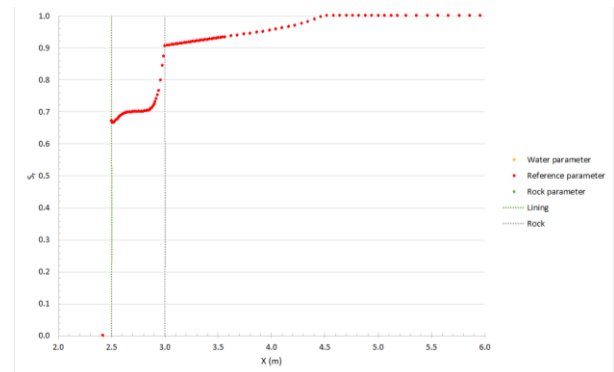


Figure 68 Horizontal degree of saturation profile during CAES-operation at the end of cycle 81 for different thermal conductivities of the cavern (TH).

4.2.2.4 Adapted permeability

Here an intrinsic permeability of 10^{-20}m^2 for the lining and 10^{-16}m^2 for the rock is used. When the intrinsic permeability of the lining has increased with one order of magnitude and of the rock decreases with one order of magnitude, it is observed that this generally has a negative effect on the temperature distribution in the lining/rock. Figure 69 shows an overall slight increase in temperature of the surrounding while the pressure in the lining is about 0.1MPa lower for the water and 0.15MPa lower for the air. Here, the ideal gas law cannot be used as the volume is not closed like in the cavern which is closed by a much more permeable wall. The temperature increase is possibly due to the thermal conductivity which becomes slightly more important as the transfer of heat by the air and water flow is less due to the more impermeable lining. (Figure 70-Figure 73)

The phenomenon of the slight lower air and water pressure is observed in all other sensitivity analysis cases. For this reason, only the graphs are given but not spoken about. The general behaviour due to the changed parameter is still compared to the corresponding reference case on the graph, but the observations for air/water pressure and distance of migration are exactly the same as in the chapter Injection in rock with lining. Thus, only the thermal results are discussed in the following cases.

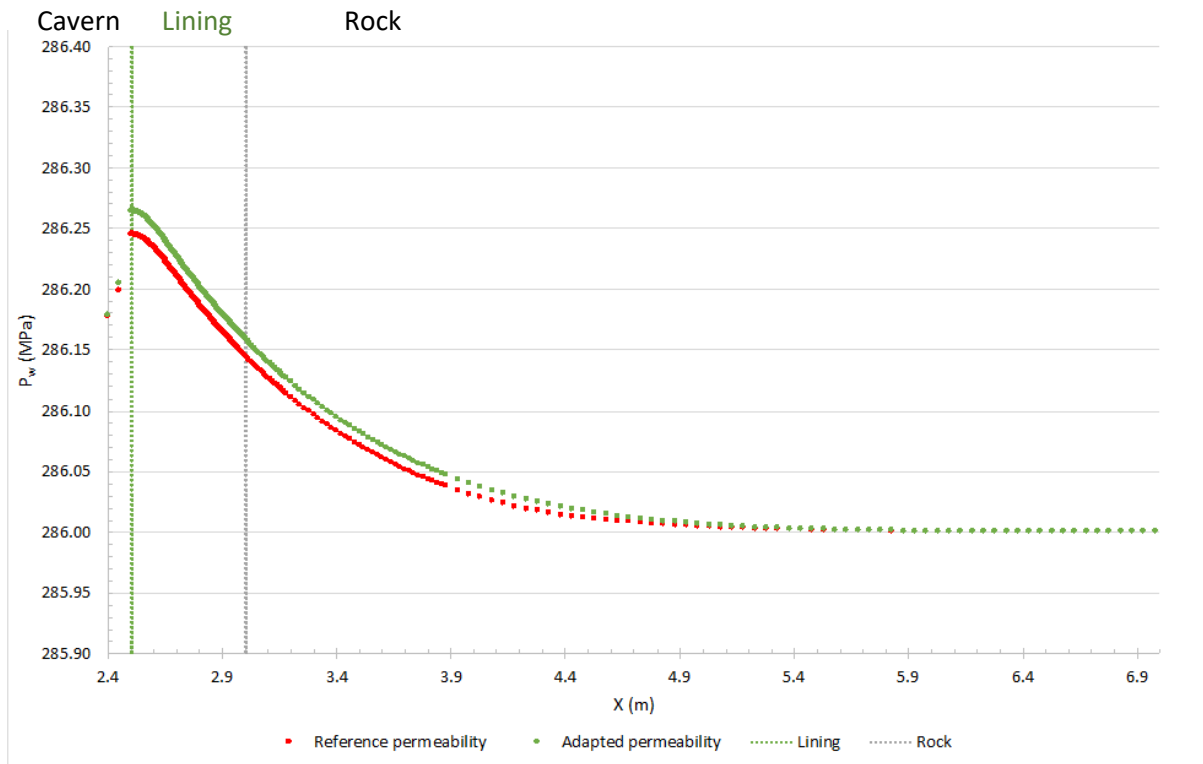


Figure 69 Horizontal temperature profile during CAES-operation at the end of cycle 81 for different permeability configurations (TH).

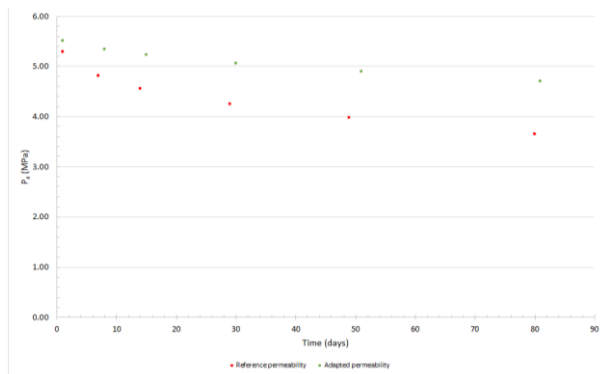


Figure 70 Cavern pressure evolution at the end of each cycle during CAES-operation for different permeability configurations (TH).

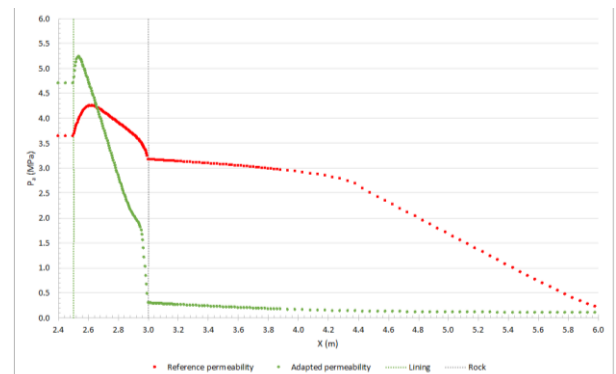


Figure 71 Horizontal air pressure profile during CAES-operation at the end of cycle 81 for different permeability configurations (TH).

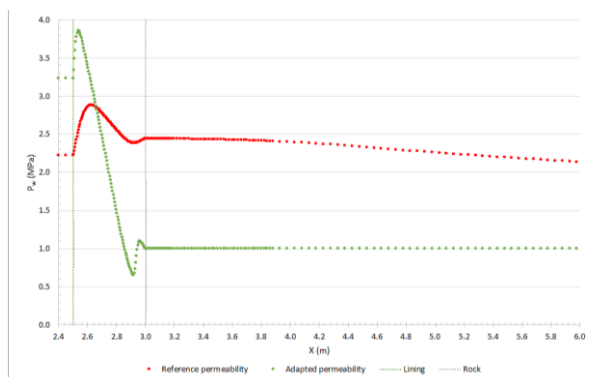


Figure 72 Horizontal water pressure profile during CAES-operation at the end of cycle 81 for different permeability configurations (TH).

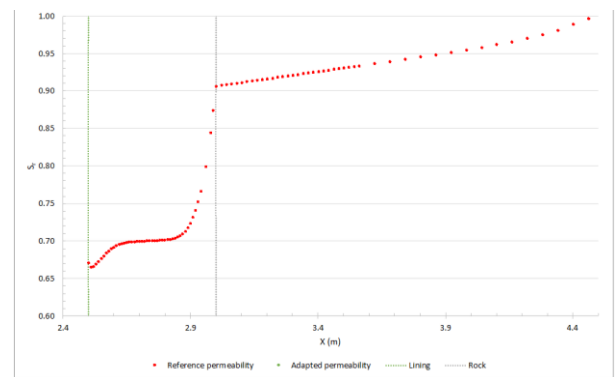


Figure 73 Horizontal degree of saturation profile during CAES-operation at the end of cycle 81 for different permeability configurations (TH).

4.2.2.5 Air entry pressure

The following values for air entry pressure are used: 735kPa (reduced), 1.47MPa (reference) and 14.7MPa (increased). Two cases are studied:

- Only AEP of rock is adapted
- AEP of concrete lining and rock is adapted

The change in air entry pressure causes also changes for the temperature except in the case with a reduced air entry pressure in the rock only (Figure 74). Previously in the hydraulic model, also the pressures in the lining were in this case close to the simulation with reference air entry pressure.

The change of the overall air entry pressure of the concrete lining and rock has the biggest influence on the temperature. An increase in global air entry pressure causes an immediate increase in the horizontal temperature profile, the opposite happens if there is a global air entry pressure reduction. This can be linked to the cavern air pressure at the end of a cycle, thus the base pressure, which makes that the global air entry pressure sensitivity analysis is exactly the same as with the global injection rates in Initialisation + operational phase.

For the increase in air entry pressure for the rock, the temperature increase is limited. Again, a relation between the temperature and the air pressure in the lining can be observed. As the air pressure in the concrete lining is only a bit higher than the reference case, the temperature is also.

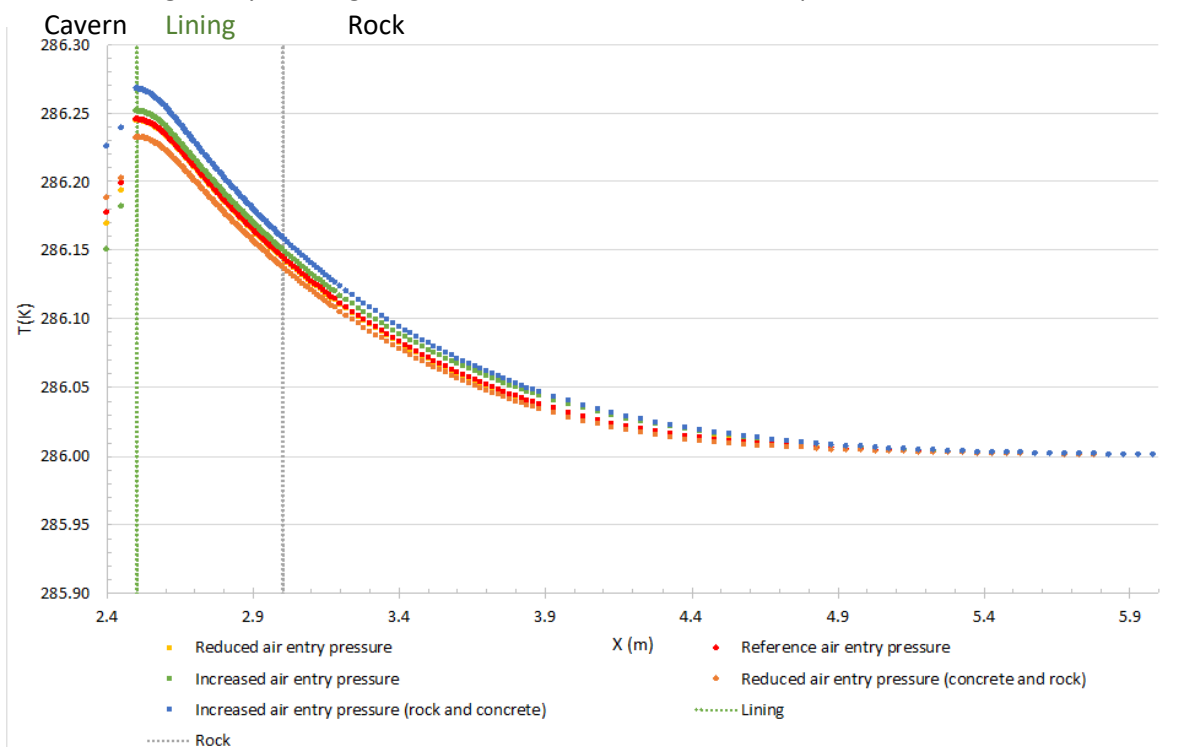


Figure 74 Horizontal temperature profile during CAES-operation at the end of cycle 81 for different air entry pressures (TH).

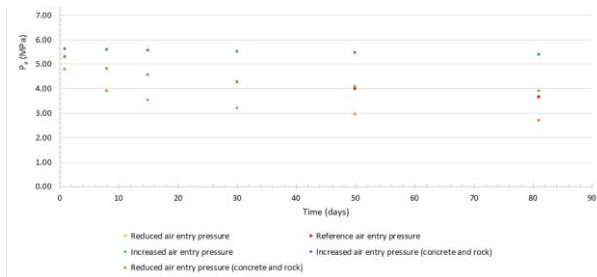


Figure 75 Cavern pressure evolution at the end of each cycle during CAES-operation for different air entry pressures (TH).

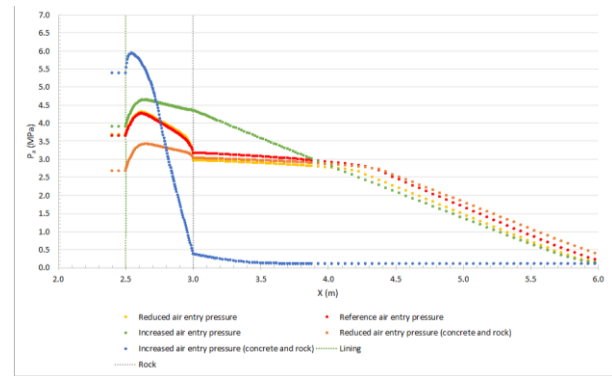


Figure 76 Horizontal air pressure profile during CAES-operation at the end of cycle 81 for different air entry pressures (TH).

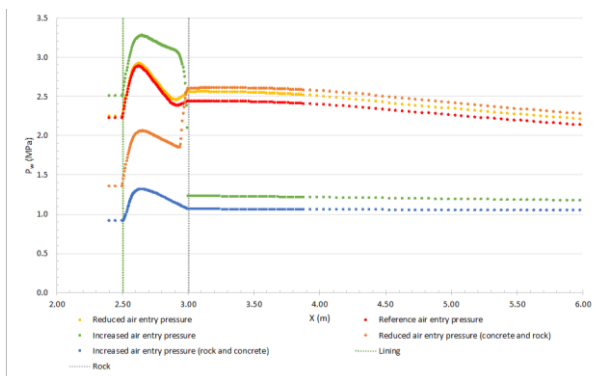


Figure 77 Horizontal water pressure profile during CAES-operation at the end of cycle 81 for different air entry pressures (TH).

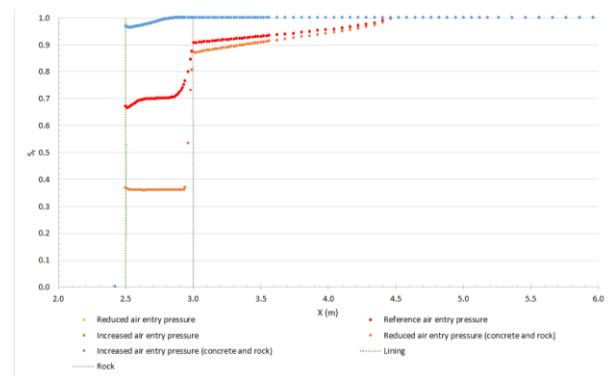


Figure 78 Horizontal degree of saturation profile during CAES-operation at the end of cycle 81 for different air entry pressures (TH).

4.2.2.6 Injection rate

The following chapter deals with the influence of an injection rate that is twice higher or lower. The injection rates used are $3.957 \cdot 10^{-5}$ kg/s (reduced), $7.913 \cdot 10^{-5}$ kg/s (reference) and $15.826 \cdot 10^{-5}$ kg/s (increased). Two cases have been investigated:

- Only the operational phase
- Initialisation + operational phase

Operational phase

Increased injection rate during the operational phase causes a lower air pressure in the cavern after each cycle, as seen before, but also lead to lower lining and rock temperatures. Figure 79 shows the temperature profile which is closely related to Figure 80. This is according to the ideal gas law behaviour. Next to that, during withdrawal of the air at higher rates, the cavern reaches lower temperatures and thus also starts cooling down the concrete lining in the 8h waiting period. So during injection, the temperature influences the pressure slightly, but during withdrawal, the pressure reduction causes temperature changes.

On the other side for reduced injection rates, the temperature is generally higher. This is due to the smaller variation on the base pressure, which causes that the overall pressure in the cavern is more 'homogeneous' as with the increased rate pressure variation is much larger. This low variation causes lower temperature variation which allow an easier thermal transfer.

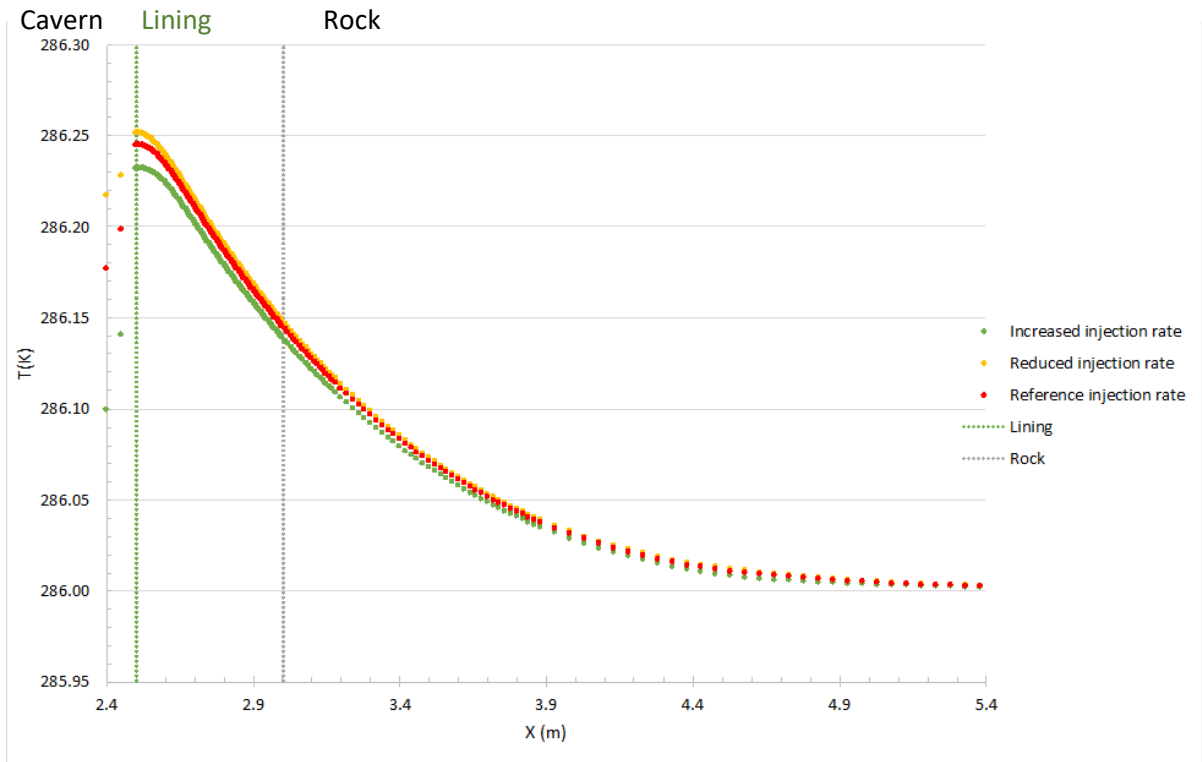


Figure 79 Horizontal temperature profile during CAES-operation at the end of cycle 81 for operational injection rates (TH).

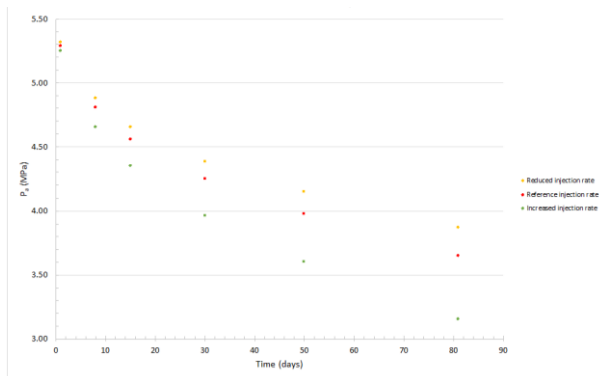


Figure 80 Cavern pressure evolution at the end of each cycle during CAES-operation for operational injection rates (TH).

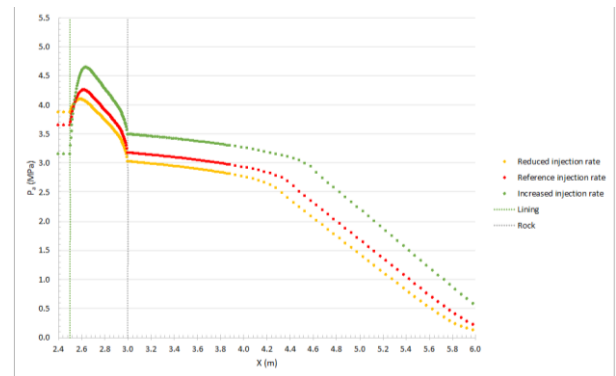


Figure 81 Horizontal air pressure profile during CAES-operation at the end of cycle 81 for operational injection rates (TH).

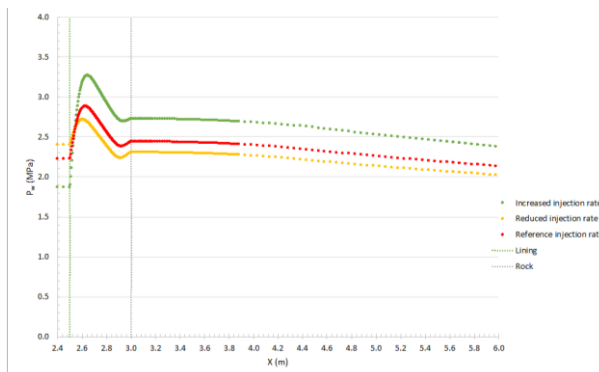


Figure 82 Horizontal water pressure profile during CAES-operation at the end of cycle 81 for operational injection rates (TH).

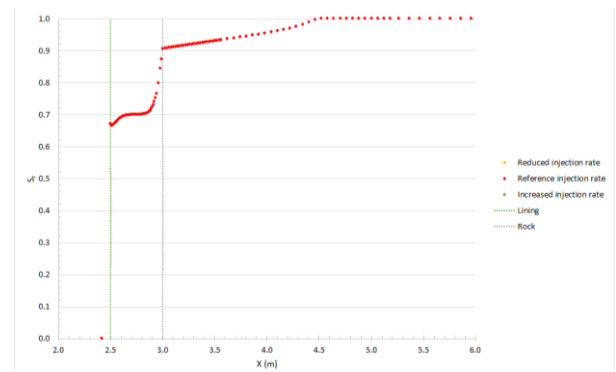


Figure 83 Horizontal degree of saturation profile during CAES-operation at the end of cycle 81 for operational injection rates (TH).

Initialisation + operational phase

In the case where the injection pressure is changed for all processes, the opposite of the previous case with only operational injection rate changes, is observed. Due to the higher base pressure in the cavern, the air migrates further and easier in the rock. Upon this base pressure, pressure variation in the cavern cause temperature changes. The high base pressure has higher variations in opposite to the one with low base pressure. These higher temperature changes are transferred mainly by the air flow and also the water flow in the lining and rock. In this case, exchange of heat caused by the fluid flows are more important.

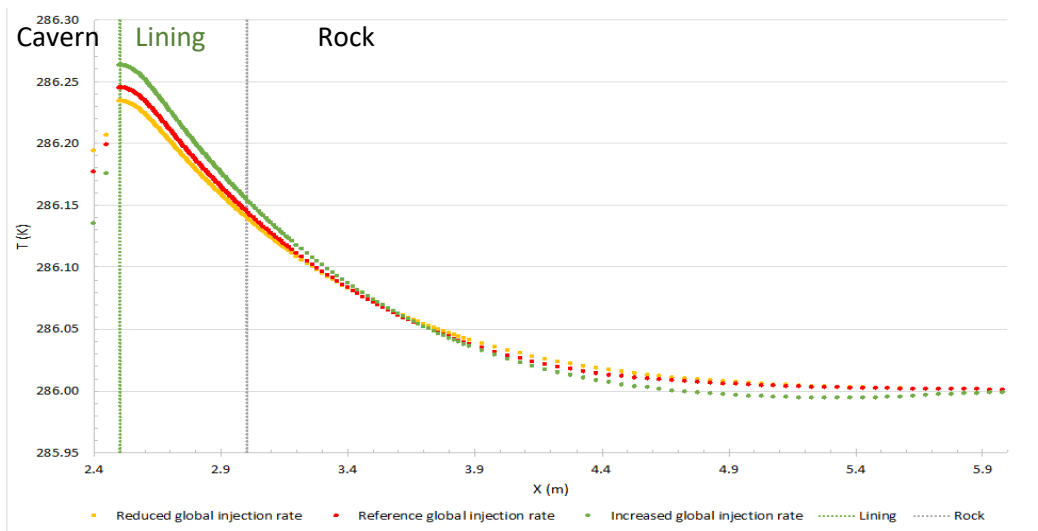


Figure 84 Horizontal temperature profile during CAES-operation at the end of cycle 81 for global injection rates (TH).

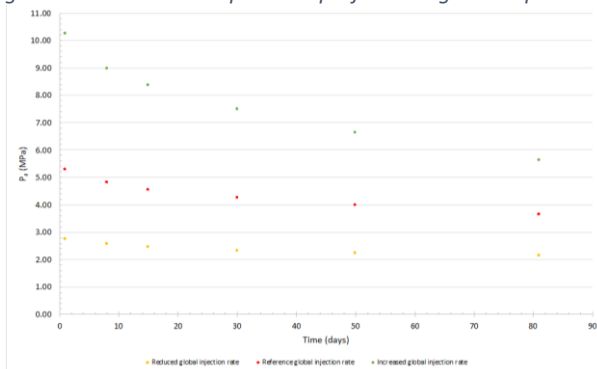


Figure 85 Cavern pressure evolution at the end of each cycle during CAES-operation for global injection rates (TH).

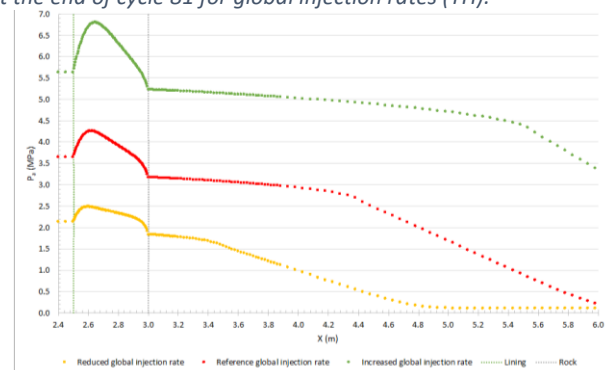


Figure 86 Horizontal air pressure profile during CAES-operation at the end of cycle 81 for global injection rates (TH).

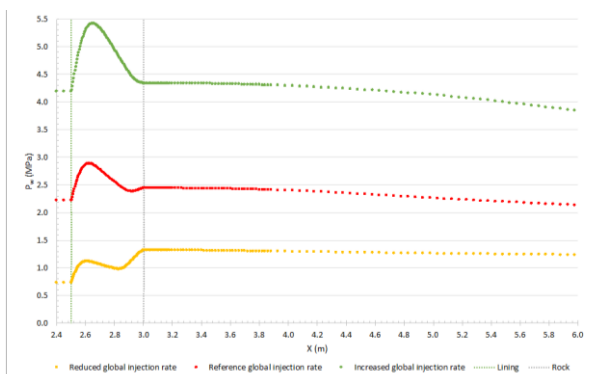


Figure 87 Horizontal water pressure profile during CAES-operation at the end of cycle 81 for global injection rates (TH).

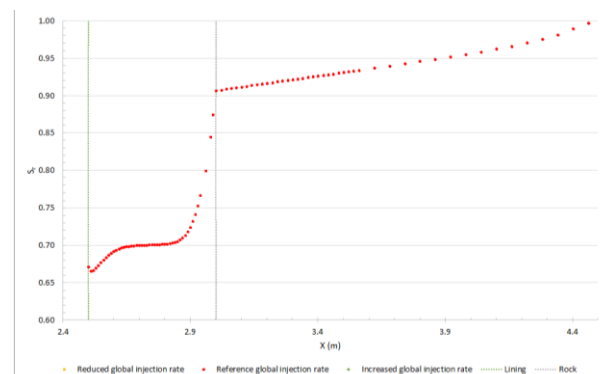


Figure 88 Horizontal degree of saturation profile during CAES-operation at the end of cycle 81 for global injection rates (TH).

4.3 Efficiency

In this chapter the daily average leakage between all different hydraulic and thermo-hydraulic cases are studied for 80 cycles between the end-state of cycles 1 and 81. Table 8 shows the overview of the leakage of all cases. For the reference, case the hydraulic and thermo-hydraulic are very corresponding. The same is valid for almost all other cases. Only both global air entry pressure sensitivity analyses show a slight bigger difference between the two cases. Generally, the coupling between pressure and temperature is low. The influence on the leakage is a slight increase with the introduction of the thermal aspect in the model. Only the reduction of the air entry pressure in the rock and lining show a decrease in leakage. This is due to an easier withdrawal of air from the lining in combination with the temperature variations.

As can be observed the permeability of the concrete lining has a big influence of the leakage. One order of magnitude lower permeability for the lining and one higher for the rock leads to a reduction of the leakage by 50%. So, concrete linings, when additional steel or rubber sealing are absent, should be installed very carefully.

Table 8 Overview of leakage percentage based on the mean daily air mass loss for all simulated cases in the hydraulic and thermo-hydraulic model with the difference between both.

Leakage (%)	Value	Hydraulic	Thermo-hydraulic	Absolute difference	Relative difference
Reference	-	0.857	0.863	0.006	0.69
Adapted permeability	10^{-20}m^2 & 10^{-16}m^2	0.390	0.429	0.039	9.92
Operational injection rate increased	$15.826 \cdot 10^{-5}\text{kg/s}$	0.514	0.552	0.037	7.29
Operational injection rate reduced	$3.956 \cdot 10^{-5}\text{kg/s}$	1.505	1.522	0.017	1.16
Global injection rate increased	$15.826 \cdot 10^{-5}\text{kg/s}$	1.203	1.209	0.006	0.49
Global injection rate reduced	$3.956 \cdot 10^{-5}\text{kg/s}$	0.612	0.637	0.025	4.15
Air entry pressure increased (rock)	14.7MPa	0.713	0.734	0.021	2.98
Air entry pressure reduced (rock)	0.735MPa	0.845	0.855	0.010	1.23
Global air entry pressure increased (lining+rock)	14.7MPa	0.065	0.121	0.057	87.58
Global air entry pressure reduced (lining+rock)	0.735MPa	1.159	1.106	0.052	4.52
Increased injection temperature	50°C		0.887		
Whole cavern imposed temperature	-		0.875		
Cavern thermal conductivity rock	2.637 W/mK		0.873		
Cavern thermal conductivity water	0.58W/mK		0.867		

The operational injection rate upon the reference base pressure should be high enough as higher pressure variation reduced the leakage. However, the air can migrate slightly further in the rock than in the reference case. When the injection rate is changed globally, thus having a different base pressure in the cavern, the inverse is observed. There the high base pressure with according high pressure

variation is worse than the reference case. This can be explained by the fact that the high base pressure pushes the air into the lining and rock much further and at higher pressures leading to bigger losses. Due to the high base pressure it is more difficult for this air to flow back to the cavern.

Thus, injection rate at relative low base pressure with a higher operational injection rate is advised. The high operational pressure should assure that a large amount of energy can be stored in the cavern as this is directly linked to the mass of air. The low base pressure can however make it more difficult in terms of efficiency to extract the total amount of air injected during a cycle. A compromise should be found between leakage and overall efficiency.

The decreasing cavern pressure can be solved by introducing additional phases every 15 or 30 days to bring the cavern back to the base pressure.

The air entry pressure has a positive effect on the leakage when it increases. The most ideal situation is a concrete lining with a high air entry pressure and a rock where the air entry pressure is of the same order of magnitude. As a value that is lower for the rock causes a leakage similar to the reference. This last is confirmed by comparing the reduced air entry pressure (rock only) to the reference case. Of course a higher air entry pressure of the rock helps to lower the leakage.

The last four thermo-hydraulic cases are in terms of leakage all slightly worse than the reference case. Increasing injection temperature prevents the cooling and reheating of air upon energy production, but it negatively influences the leakage, in a minor way. The thermal conductivity of the cavern, which is most logically the one of air, is also the best solution for having low leakage. The higher thermal conductivities cause higher temperatures and as observed higher temperatures are less efficient in terms of leakage due to higher pressures in general. But the influence of the thermal aspect of the simulation remains neglectable in comparison to the influence of pressure loss in the cavern.

In conclusion, it is advised to operate a CAES-plant with a base pressure equal to the one of the reference case (5.5MPa) or slightly lower. This, in a cavern which has a high impermeable lining (10^{-20}m^2) with high air entry pressure(1.47MPa-14.7MPa). The properties of the rock are less important, remarking that the mechanical behaviour and stresses are the most limiting factor here and were not studied. Injection during daily cycles happens at reference injection rate ($7.913 \cdot 10^{-5}\text{kg/s}$) or preferentially higher with air that is cooled to temperatures that are close to the ambient temperatures of the surrounding rock, to guarantee the overall efficiency. Generally, a large cavern is needed as this stores high masses of air. This makes that the relative leakage stays limited in comparison to low air mass containing caverns as leakage is proportionally higher.

4.4 Perspectives on rock cracking

Suppose that after years of operation, somewhere in the underground a crack appears in the rock. This changes the parameters of the rock. This has mainly influence on the porosity and permeability of the rock. Also the air entry pressure can change in that part of the rock. As a crack is a preferential way of fluid flow due to the low restrictions, leakage will increase. The main factor for the efficiency consequences are in the location and extent of the crack. If the whole rock mass is cracked, leakage can increase with at least some percentages. If only a small part of the rock is cracked, take a crack over a distance of 2m for example, the location is determining. Close to the lining, the influence on the leakage will be higher than when the crack is located at 25m from the cavern center. Based on monitoring of the average daily leakage it is possible to detect potential cracks when sudden changes appear. It is then important to take the corresponding measures like installing an internal seal of steel or rubber if there are a large amount of cracks. Or in case of fewer crack or bigger cracks it is possible to fill these crack with grout or other special chemical filling materials.

Chapter 5 Conclusion

This thesis investigated the thermo-hydraulic behaviour of a compressed air energy storage cavern and its efficiency. This is done by simulations in the finite element software Lagamine of a lined and unlined model. This chapter gives a brief overview of the main aspects of the thesis.

The compressed air energy storage is used to store renewable energy at off-peak hours. This compressed air is then used during peak hours to produce energy in a modified gas turbine. This allows to produce more energy with the same amount of fuel as the compression stage is an energy demanding step. Operation of the CAES-cavern happens in daily cycles where air is injected for 8h, after which a rest period of 4h comes. Followed by 4h of withdrawal at twice the injection rate after which the cavern stabilises for 8 more hours.

Earlier research was done mostly by Rutqvist and Kim. Their research is based and linked partially to the operational real-scale CAES-facilities. The research is mainly in the field of thermo-mechanical behaviour.

The unlined hydraulic model shows acceptable leakage rates if the rock mass has a sufficient low permeability ($<10^{-18}\text{m}^2$). These kind of caverns are often found in salt rock. The lined hydraulic model has a 50cm thick concrete lining with a permeability of 10^{-19}m^2 . The sensitivity analysis made it possible to determine a set of parameters that allows to reduce the daily average leakage calculated over a period of 80 days. In general, it is advised to operate a CAES-plant with a base pressure of 5.5MPa or slightly lower. This, in a cavern which has a high impermeable lining (10^{-20}m^2) with high air entry pressure (1.47MPa-14.7MPa). The properties of the rock are less important than the ones of the lining, remarking that the mechanical behaviour and stresses are the most limiting factor here and were not studied. However, a higher air entry pressure of the rock influences the leakage positively. Injection during daily cycles happens at an injection rate of $7.913 \cdot 10^{-5}\text{kg/s}$ or preferentially higher with air that is cooled to temperatures that are close to the ambient temperatures of the surrounding rock. A large cavern is advisable as it is able to store a higher mass of air and is better at limiting the leakage due to the high air mass. With this set of parameters it is possible to limit the leakage to less than 0.5%/day.

The thermo-hydraulic model does not bring new insights. It proves that the temperature-pressure coupling is low. The temperature of injection should be around the ambient temperature of the surroundings but a compromise can be made if this increases the efficiency of the overall CAES-plant with gas turbine.

A solution to the decreasing cavern pressure can be solved by introducing additional phases every 15 or 30 days to bring the cavern back to the base pressure. This guarantees a higher overall efficiency and comes at a small extra cost.

For future research it would be interesting to see what the effect of long term storage brings to the rock if the proposed parameters are used. The occurrence of natural cracks in rock should be taken into account in a model to have an idea of the additional leakage caused by these cracks. In a further stage, the model can be included in a simulation of the overall process, starting from renewable energy production, over CAES-storage and energy production to delivery on the power grid.

Chapter 6 Bibliography

- British Geological Survey, 2015. *Underground natural gas storage in the UK*. [Online] Available at: <http://www.bgs.ac.uk/research/energy/undergroundGasStorage.html> [Accessed 5 May 2015].
- Bullough, C. et al., 2004. *Advanced adiabatic compressed air energy storage for integration of wind energy*. London UK, EWEC 2004, pp. 22-25.
- Charlier, R. et al., 2013. An unsaturated hydro-mechanical modelling of two in-situ experiments in Callovo-Oxfordian argillite. *Engineering Geology*, Issue 165, pp. 46-63.
- Fluxys, 2012. *Storage programme*, Loenhout: Fluxys.
- Gerard, P., 2011. Impact des transferts de gaz sur le comportement poro-mécanique des matériaux argileux. *PhD Thesis*, p. 301.
- Ibrahim, H., Ilinca, A. & Perron, J., 2008. Energy storage systems-Characteristics and comparisons. *Renewable and Sustainable Energy Reviews*, Issue 12, pp. 1221-1250.
- Kim, H.-M. et al., 2013. Characterizing excavation damaged zone and stability of pressurized lined rock caverns for underground compressed air energy storage. *Rock Mechanics and Rock Engineering*, Issue 46, pp. 1113-1124.
- Kim, H.-M. et al., 2012. Exploring the concept of compressed air energy storage (CAES) in lined rock caverns at shallow depth: A modeling study of air tightness and energy balance. *Applied Energy*, Issue 92, pp. 653-667.
- Lagamine, 2008. *Lagamine code preprocessore user's guide*, Brussels: LagaProgs.
- Laudone, G. M., Gribble, C. M., Jones, K. L. & J., C. H., 2015. Validated a priori calculation of tortuosity in porous materials including sandstone and limestone. *Chemical Engineering Science*, Issue 131, pp. 109-117.
- Martin, L. B., Rutqvist, J. & Birkholzer, J., 2015. Long-term modeling of the thermal-hydraulic-mechanical response of a generic salt repository for heat-generating nuclear waste. *Engineering Geology*, Issue 193, pp. 198-211.
- McGrail, B. et al., 2013. Grid-scale technology for renewable integration in the Pacific Northwest. *Pacific Northwest National Laboratory*, Issue PNNL-22235-FL, p. 8.
- Mohanto, S., Singh, K., Chakraborty, T. & Basu, D., 2014. Cyclic thermo-mechanical analysis of wellbore in underground compressed air energy storage cavern. *Geotechnical and Geological Engineering*, Issue 32, pp. 601-616.
- Rutqvist, J. et al., 2012. Modeling of coupled thermodynamic and geomechanical performance of underground compressed air energy storage in lined rock caverns. *International Journal of Rock Mechanics & Mining Sciences*, Issue 52, pp. 71-81.
- Wang, T. et al., 2013. A new shape design method of salt cavern used as underground gas storage. *Applied Energy*, Issue 104, pp. 50-61.
- Wyllie, M., 1965. *Underground gas storage process*. USA, Patent No. 3.175.614.
- Xia, C. et al., 2015. A simplified and unified analytical solution for temperature and pressure variations in compressed air energy storage caverns. *Renewable Energy*, Issue 74, pp. 718-726.

Yang, C. et al., 2015. Feasibility analysis of using abandoned salt caverns for large-scale underground energy storage in China. *Applied Energy*, Issue 137, pp. 467-481.

Zlender, B., Jelusic, P. & Boumezerane, D., 2013. The feasibility analysis of underground gas storage caverns. *Engineering Structures*, Issue 55, pp. 16-25.

Appendix A *Unlined hydraulic model*

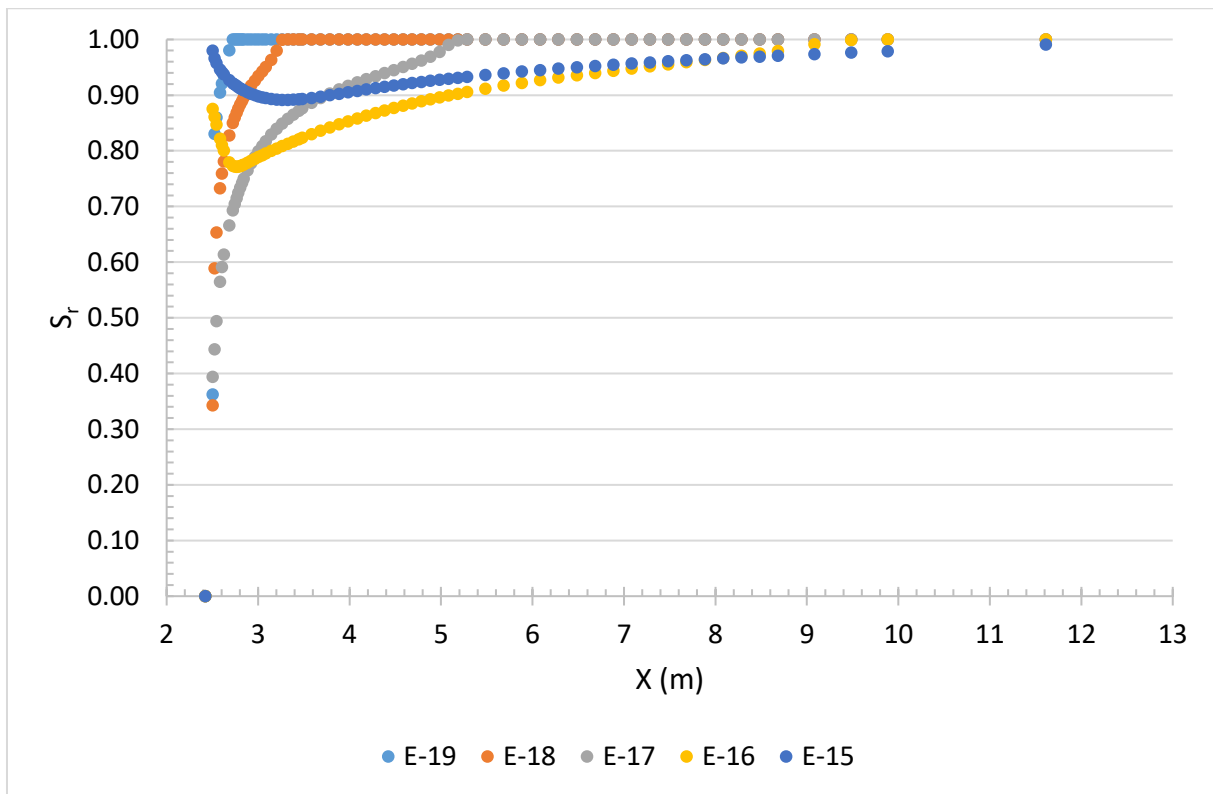


Figure 89 Horizontal profile of the degree of saturation at the end of cycle 81 for different permeabilities for the unlined hydraulic model.

Appendix B Lined hydraulic model

B.1 Reference case

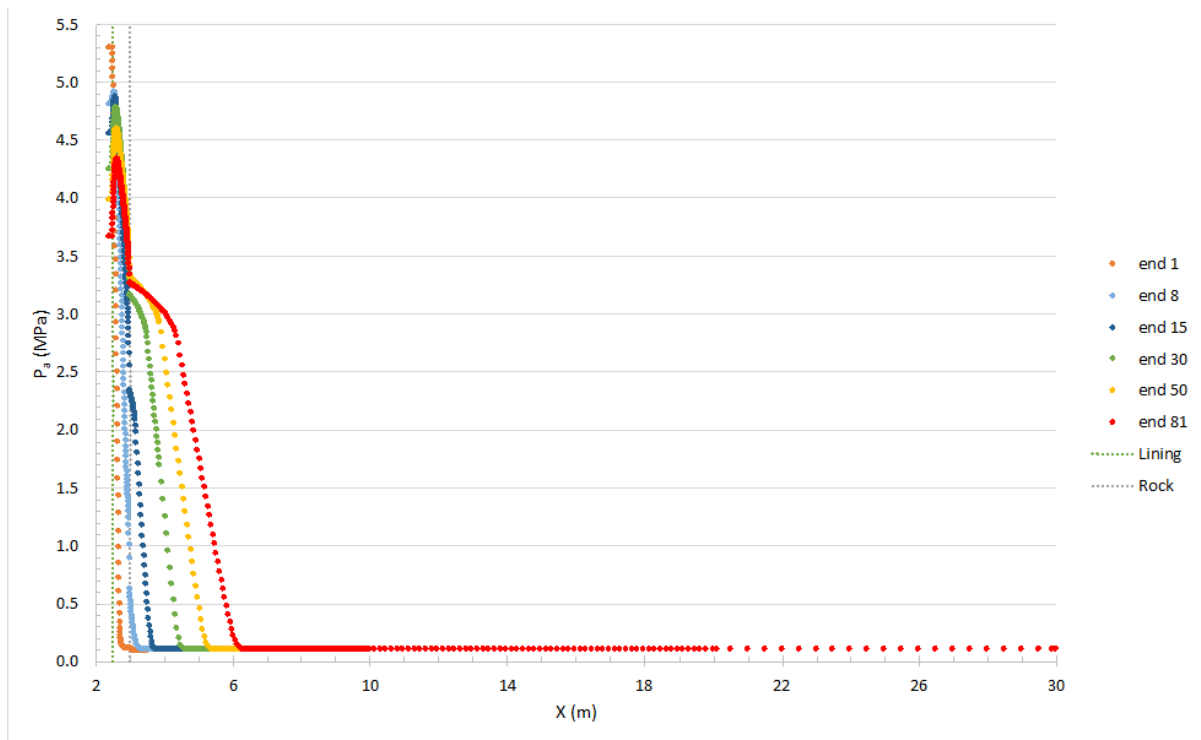


Figure 90 Full horizontal air pressure profile for the reference concrete case (H).

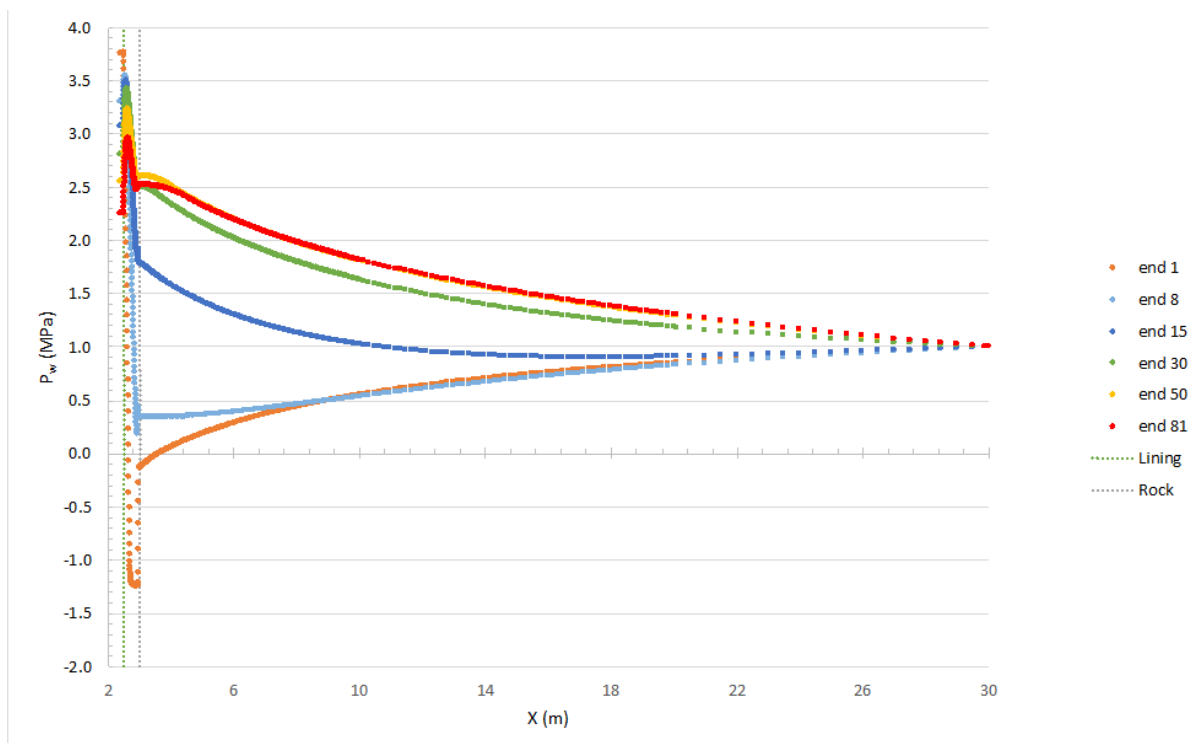


Figure 91 Full horizontal water pressure profile for the reference concrete case (H).

B.2 Adapted permeabilities

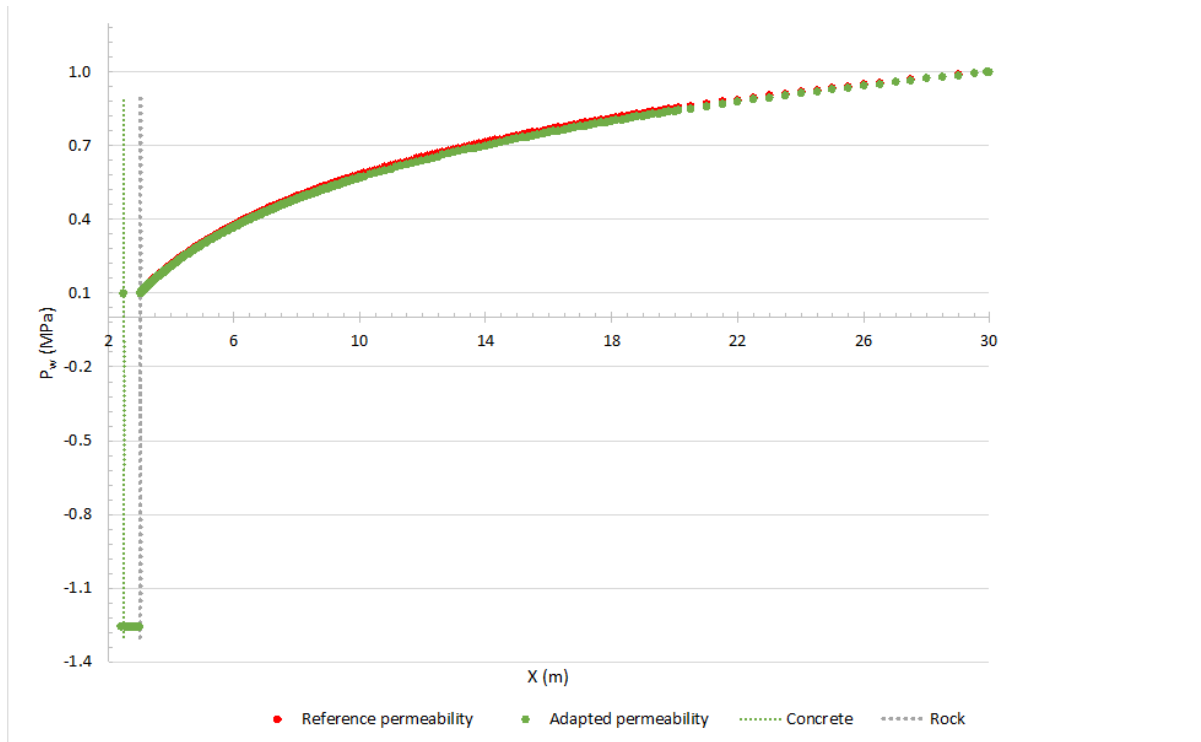


Figure 92 Horizontal water pressure profile for the sensitivity analysis with adapted intrinsic permeability after the excavation stage (H).

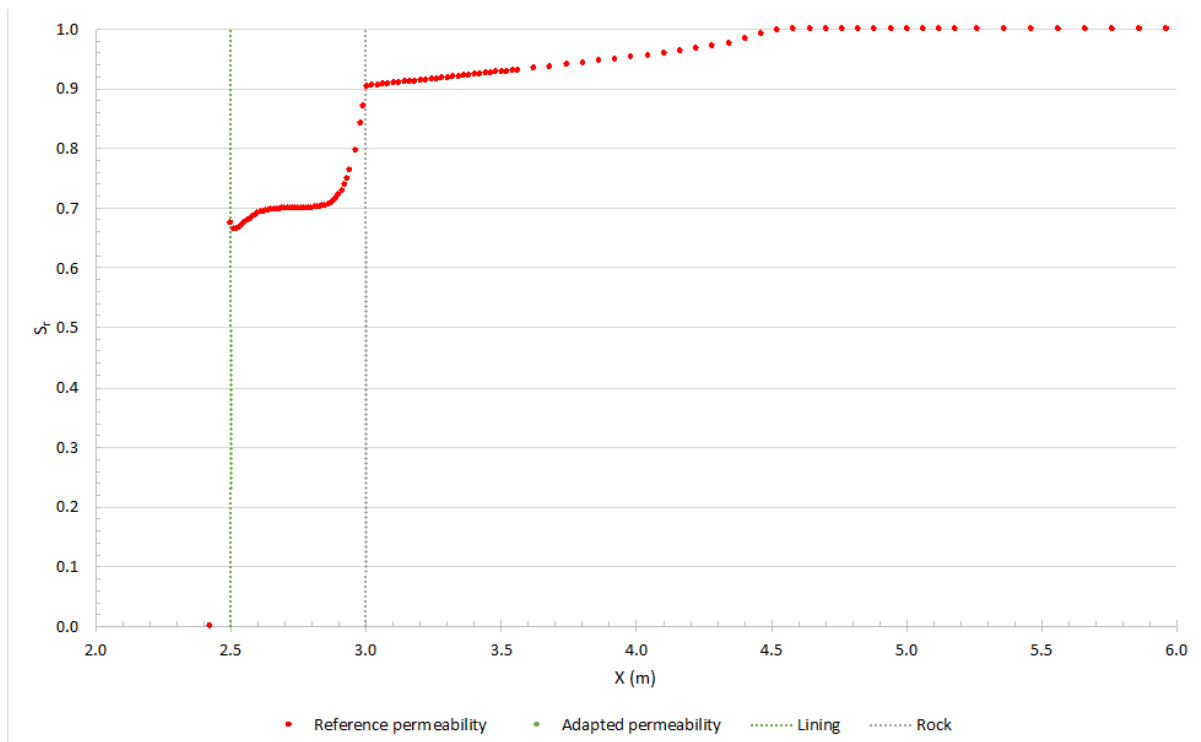


Figure 93 Horizontal profile of degree of saturation for the adapted permeability sensitivity analysis during CAES-operation (H).

B.3 Air entry pressure

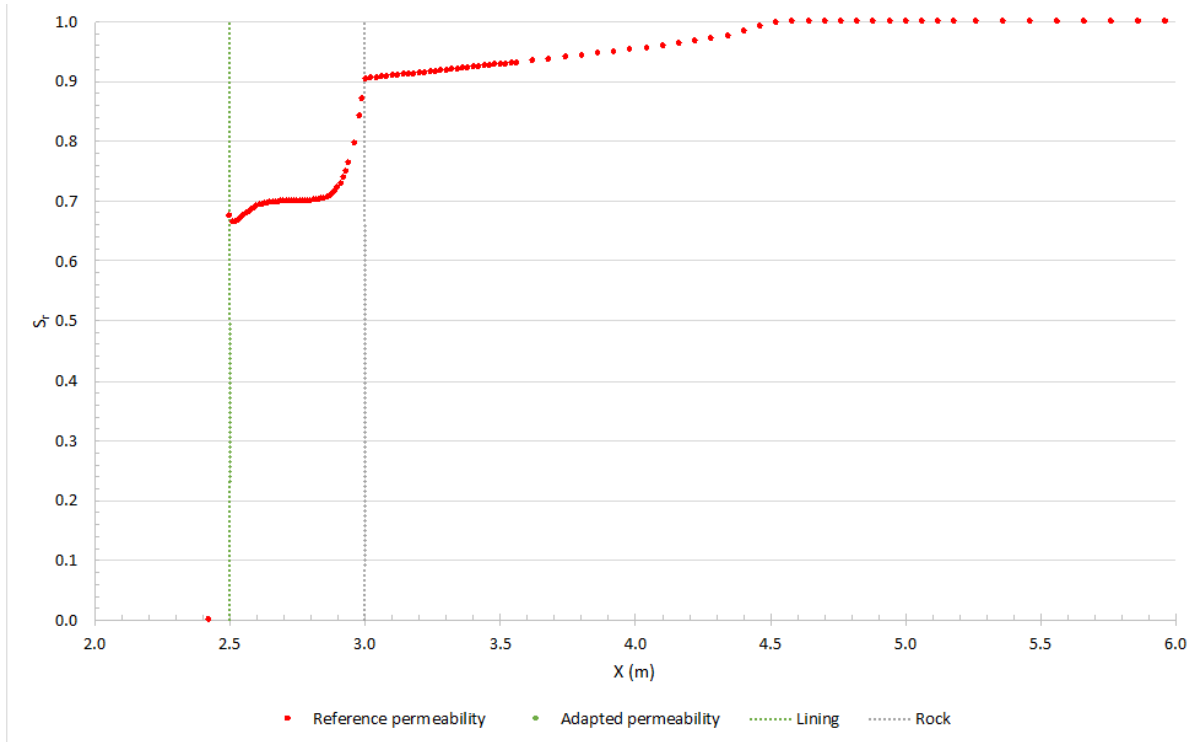


Figure 94 Horizontal profile of degree of saturation for operational air entry pressure sensitivity analysis during CAES-operation (H).

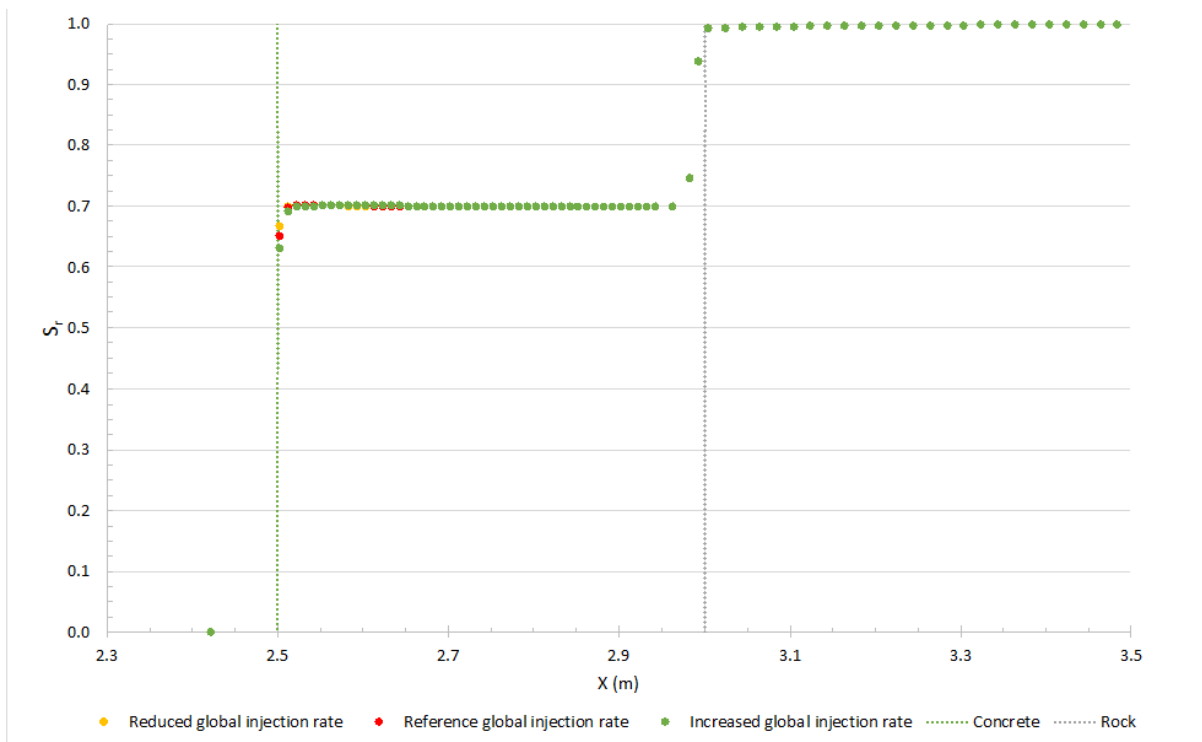


Figure 95 Horizontal profile of degree of saturation for global air entry pressure sensitivity analysis after initialisation (H).

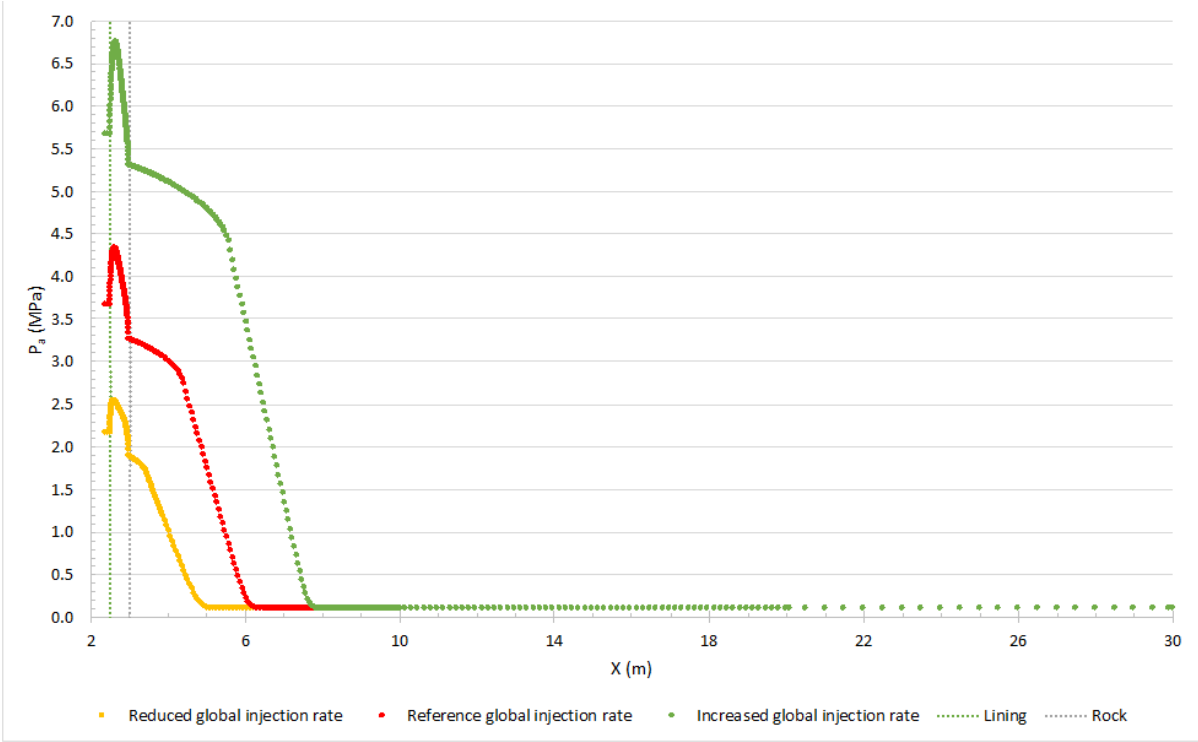


Figure 96 Full horizontal air pressure profile at the end of cycle 81 during CAES-operation for different global injection rate (H).

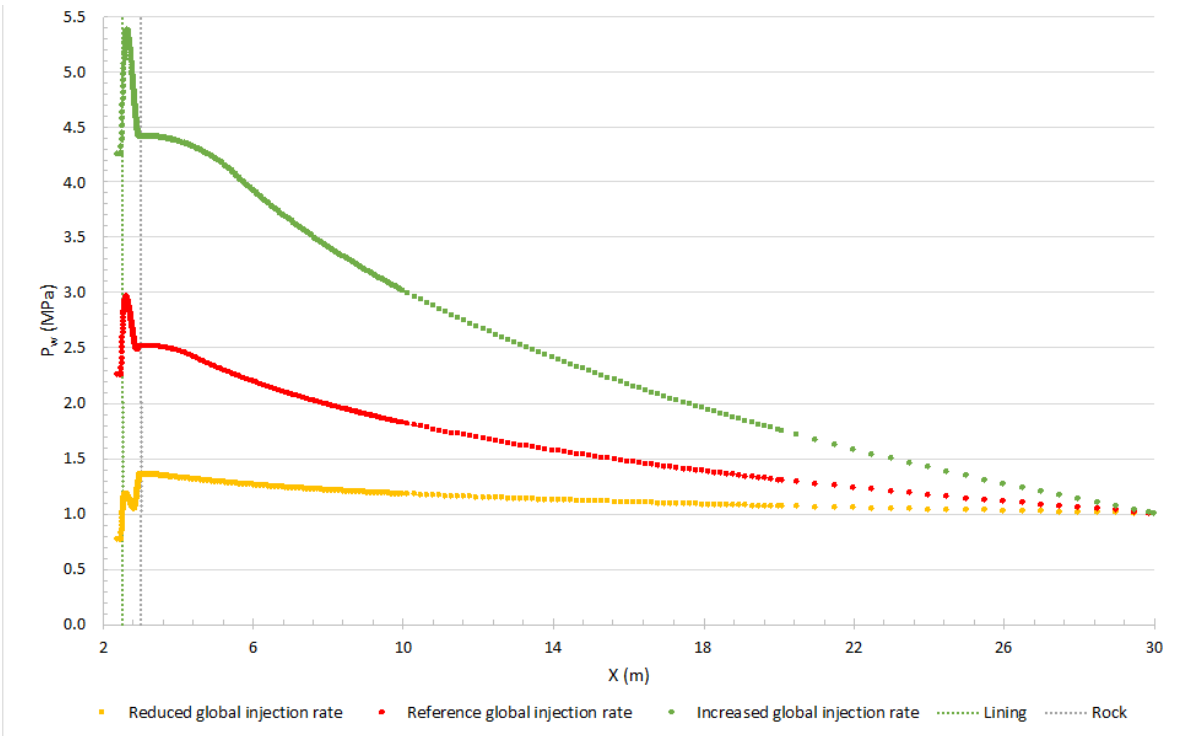


Figure 97 Full horizontal water pressure profile at the end of cycle 81 during CAES-operation for different global injection rate (H).

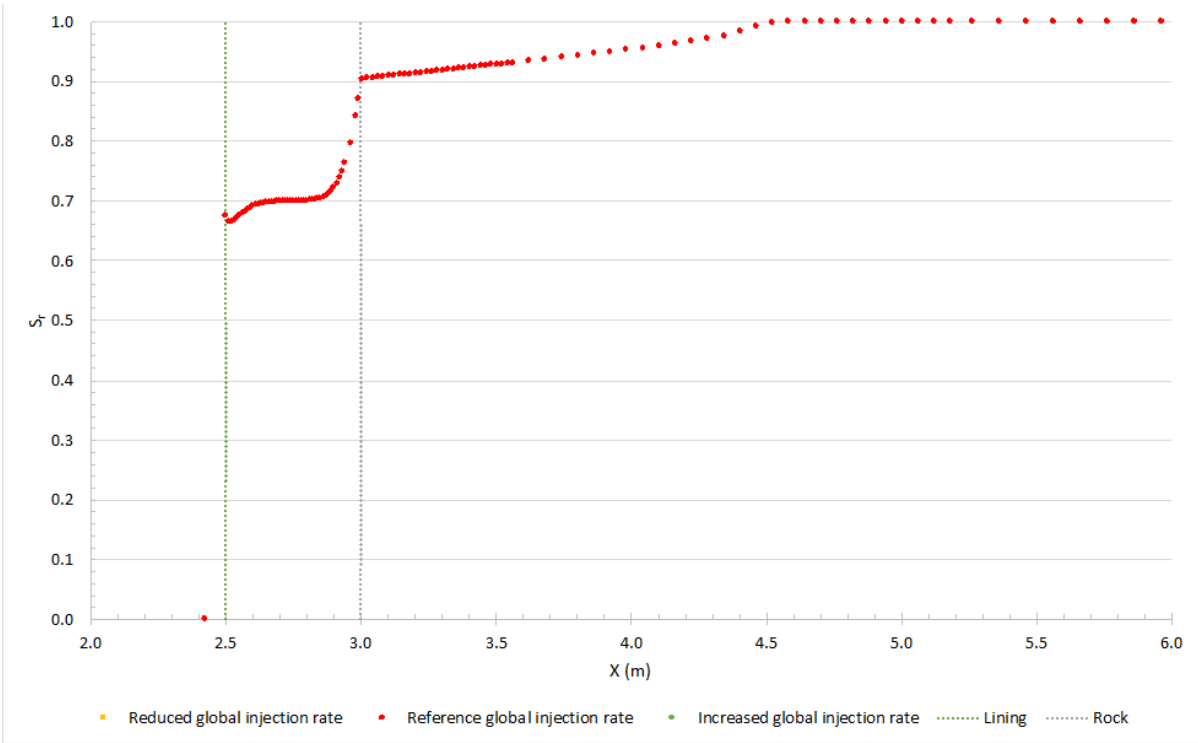


Figure 98 Horizontal profile of degree of saturation for operational air entry pressure sensitivity analysis during CAES-operation (H).

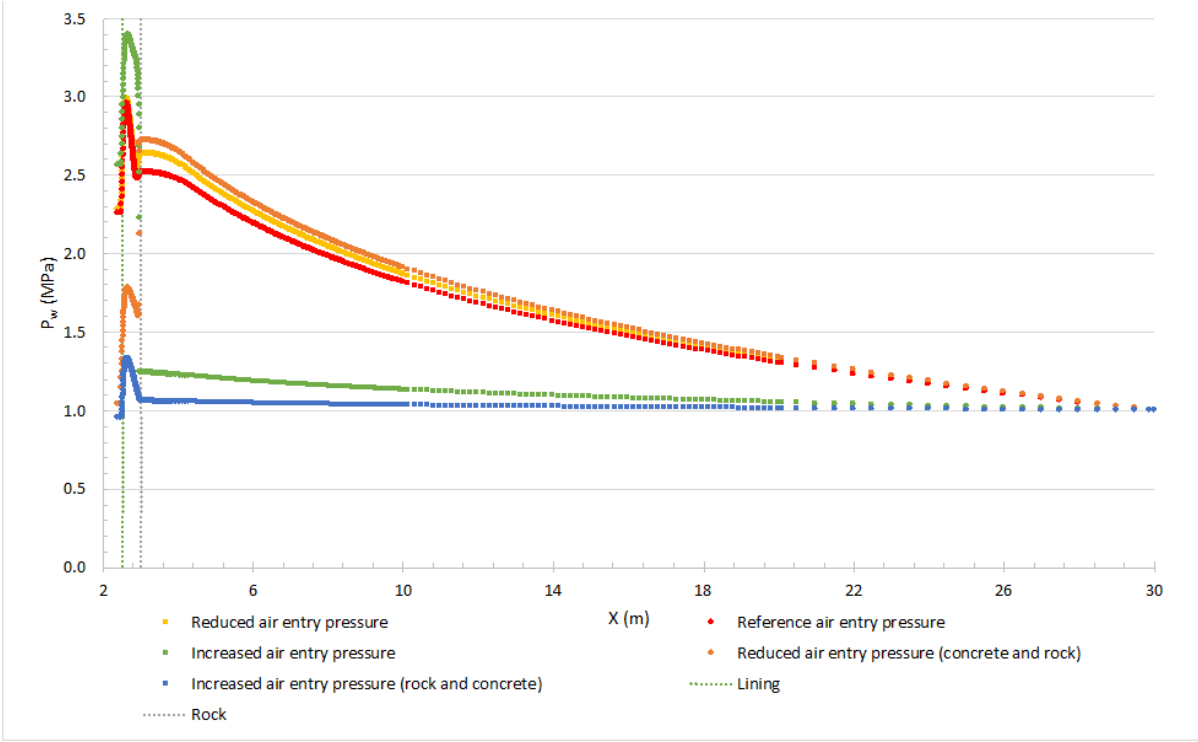


Figure 99 Full horizontal water pressure profile for different air entry pressures (H).

Appendix C Leakage calculation

Below a general calculation scheme is presented. In the property 1 & 2 column, the pressure and temperature at that time can be found. On the top right of the scheme the current case is mentioned followed by a letter indicating the model. B for unlined hydraulic model, H for lined hydraulic model and TH for thermo-hydraulic model.

Leakage rate calculation cycle1-81			Permeability	E-19
Properties	1	2	B	
P	P1	P2	Pa	
V	V	V	m ³	
R	286.9	286.9	J/kgK	
T	T1	T2	K	
time (s)	t2-t1			
delta m	Ideal gas law	kg		
	Leakage rate			
Mean daily leakage	*86400	kg/day		
Leakage rate	Delta m/time	kg/s		
Injection rate	0.0198	kg/s		
Injection time (s)	28800	s		
Injected mass	633.6	kg/day		
Performance	(Inj-(inj-leak)) /inj *100	%		

C.1 Unlined hydraulic model

Leakage rate calculation cycle1-81			Permeability	E-19
Properties	1	2	B	
P	4539000.5	4368004.0	Pa	
V	19.63	19.63	m ³	
R	286.9	286.9	J/kgK	
T	286	286	K	
time (s)	6912000			
delta m	40.91	kg		
Mean daily leakage	0.51	kg/day		
Leakage rate	5.92E-06	kg/s		
Injection rate	0.0198	kg/s		
Injection time (s)	28800	s		
Injected mass	570.24	kg/day		
Performance	0.09	%		

Leakage rate calculation cycle1-81			Permeability E-18
Properties	1	2	
P	4519061.40	3762974.50	Pa
V	19.63	19.63	m ³
R	286.9	286.9	J/kgK
T	286	286	K
time (s)	6912000		
delta m	180.88	kg	
Mean daily leakage	2.26	kg/day	
Leakage rate	2.62E-05	kg/s	
Injection rate	0.0198	kg/s	
Injection time (s)	28800	s	
Injected mass	570.24	kg/day	
Performance	0.40	%	

Leakage rate calculation cycle1-81			Permeability E-17
Properties	1	2	
P	4928763.70	2672375.10	Pa
V	19.63	19.63	m ³
R	286.9	286.9	J/kgK
T	286	286	K
time (s)	6912000		
delta m	539.81	kg	
Mean daily leakage	6.75	kg/day	
Leakage rate	7.81E-05	kg/s	
Injection rate	0.0198	kg/s	
Injection time (s)	28800	s	
Injected mass	570.24	kg/day	
Performance	1.18	%	

Leakage rate calculation cycle1-81			Permeability E-16
Properties	1	2	
P	3537282.00	930465.87	Pa
V	19.63	19.63	m ³
R	286.9	286.9	J/kgK
T	286	286	K
time (s)	6912000		
delta m	623.64	kg	
Mean daily leakage	7.80	kg/day	
Leakage rate	9.02E-05	kg/s	
Injection rate	0.0198	kg/s	
Injection time (s)	28800	s	
Injected mass	570.24	kg/day	
Performance	1.37	%	

Leakage rate calculation cycle1-81			Permeability	E-15
Properties	1	2		
P	2294163.70	439997.24	Pa	
V	19.63	19.63	m ³	
R	286.9	286.9	J/kgK	
T	286	286	K	
time (s)	6912000			
delta m	443.58	kg		
Mean daily leakage	5.54	kg/day		
Leakage rate	6.42E-05	kg/s		
Injection rate	0.0198	kg/s		
Injection time (s)	28800	s		
Injected mass	570.24	kg/day		
Performance	0.97	%		

C.2 Lined hydraulic model

Leakage rate calculation cycle1-81			Reference	H
Properties	1	2		
P	5301905.4	3.67E+06	Pa	
V	19.63	19.63	m ³	
R	286.9	286.9	J/kgK	
T	286	286	K	
time (s)	6912000			
delta m	390.98	kg		
Mean daily leakage	4.89	kg/day		
Leakage rate	5.66E-05	kg/s		
Injection rate	0.0198	kg/s		
Injection time (s)	28800	s		
Injected mass	570.24	kg/day		
Performance	0.86	%		

Leakage rate calculation cycle1-81			Adapted permeability	H
Properties	1	2		
P	5516378.8	4.77E+06	Pa	
V	19.63	19.63	m ³	
R	286.9	286.9	J/kgK	
T	286	286	K	
time (s)	6912000			
delta m	178.01	kg		
Mean daily leakage	2.23	kg/day		
Leakage rate	2.58E-05	kg/s		
Injection rate	0.0198	kg/s		
Injection time (s)	28800	s		
Injected mass	570.24	kg/day		
Performance	0.39	%		

Leakage rate calculation cycle1-81			Increased operational injection rate	
Properties	1	2		
P	5.26E+06	3.30E+06	Pa	H
V	19.63	19.63	m ³	
R	286.9	286.9	J/kgK	
T	286	286	K	
time (s)	6912000			
delta m	469.01	kg		
Mean daily leakage	5.86	kg/day		
Leakage rate	6.79E-05	kg/s		
Injection rate	0.0396	kg/s	*2	
Injection time (s)	28800	s		
Injected mass	1140.48	kg/day		
Performance	0.51	%		

Leakage rate calculation cycle1-81			Reduced operational injection rate	
Properties	1	2		
P	5.32E+06	3.89E+06	Pa	H
V	19.63	19.63	m ³	
R	286.9	286.9	J/kgK	
T	286	286	K	
time (s)	6912000			
delta m	343.30	kg		
Mean daily leakage	4.29	kg/day		
Leakage rate	4.97E-05	kg/s		
Injection rate	0.0099	kg/s	*0.5	
Injection time (s)	28800	s		
Injected mass	285.12	kg/day		
Performance	1.51	%		

Leakage rate calculation cycle1-81			Increased global injection rate	
Properties	1	2		
P	1.03E+07	5.67E+06	Pa	H
V	19.63	19.63	m ³	
R	286.9	286.9	J/kgK	
T	286	286	K	
time (s)	6912000			
delta m	1097.68	kg		
Mean daily leakage	13.72	kg/day		
Leakage rate	1.59E-04	kg/s		
Injection rate	0.0396	kg/s	*2	
Injection time (s)	28800	s		
Injected mass	1140.48	kg/day		
Performance	1.20	%		

Leakage rate calculation cycle1-81			Reduced global injection rate	
Properties	1	2		
P	2.74E+06	2.16E+06	Pa	H
V	19.63	19.63	m ³	
R	286.9	286.9	J/kgK	
T	286	286	K	
time (s)	6912000			
delta m	139.53	kg		
Mean daily leakage	1.74	kg/day		
Leakage rate	2.02E-05	kg/s		
Injection rate	0.0099	kg/s	*0.5	
Injection time (s)	28800	s		
Injected mass	285.12	kg/day		
Performance	0.61	%		

Leakage rate calculation cycle1-81			Increased air entry pressure	
Properties	1	2		
P	5.30E+06	3.94E+06	Pa	H
V	19.63	19.63	m ³	
R	286.9	286.9	J/kgK	
T	286	286	K	
time (s)	6912000			
delta m	325.34	kg		
Mean daily leakage	4.07	kg/day		
Leakage rate	4.71E-05	kg/s		
Injection rate	0.0198	kg/s		
Injection time (s)	28800	s		
Injected mass	570.24	kg/day		
Performance	0.71	%		

Leakage rate calculation cycle1-81			Reduced air entry pressure	
Properties	1	2		
P	5.30E+06	3.69E+06	Pa	H
V	19.63	19.63	m ³	
R	286.9	286.9	J/kgK	
T	286	286	K	
time (s)	6912000			
delta m	385.32	kg		
Mean daily leakage	4.82	kg/day		
Leakage rate	5.57E-05	kg/s		
Injection rate	0.0198	kg/s		
Injection time (s)	28800	s		
Injected mass	570.24	kg/day		
Performance	0.84	%		

Leakage rate calculation cycle1-81			Increased air entry pressure (C+R)	
Properties	1	2		
P	5.61E+06	5.49E+06	Pa	H
V	19.63	19.63	m ³	
R	286.9	286.9	J/kgK	
T	286	286	K	
time (s)	6912000			
delta m	29.47	kg		
Mean daily leakage	0.37	kg/day		
Leakage rate	4.26E-06	kg/s		
Injection rate	0.0198	kg/s		
Injection time (s)	28800	s		
Injected mass	570.24	kg/day		
Performance	0.06	%		

Leakage rate calculation cycle1-81			Reduced air entry pressure (C+R)	
Properties	1	2		
P	4.66E+06	2.45E+06	Pa	H
V	19.63	19.63	m ³	
R	286.9	286.9	J/kgK	
T	286	286	K	
time (s)	6912000			
delta m	528.58	kg		
Mean daily leakage	6.61	kg/day		
Leakage rate	7.65E-05	kg/s		
Injection rate	0.0198	kg/s		
Injection time (s)	28800	s		
Injected mass	570.24	kg/day		
Performance	1.16	%		

C.3 Thermo-hydraulic model

Leakage rate calculation cycle1-81			Reference	
Properties	1	2		
P	5288977.8	3.65E+06	Pa	TH
V	19.63	19.63	m ³	
R	286.9	286.9	J/kgK	
T	2.86E+02	2.86E+02	K	
time (s)	6912000			
delta m	393.67	kg		
Mean daily leakage	4.92	kg/day		
Leakage rate	5.70E-05	kg/s		
Injection rate	0.0198	kg/s		
Injection time (s)	28800	s		
Injected mass	570.24	kg/day		
Performance	0.86	%		

Leakage rate calculation cycle1-81				Increased injection temperature
Properties	1	2		
P	5.29E+06	3.60E+06	Pa	TH
V	19.63	19.63	m ³	
R	286.9	286.9	J/kgK	
T	2.87E+02	2.87E+02	K	
time (s)	6912000			
delta m	404.44	kg		
Mean daily leakage	5.06	kg/day		
Leakage rate	5.85E-05	kg/s		
Injection rate	0.0198	kg/s		
Injection time (s)	28800	s		
Injected mass	570.24	kg/day		
Performance	0.89	%		

Leakage rate calculation cycle1-81				Injection temperature whole cavern
Properties	1	2		
P	5.35E+06	3.70E+06	Pa	TH
V	19.63	19.63	m ³	
R	286.9	286.9	J/kgK	
T	2.90E+02	2.93E+02	K	
time (s)	6912000			
delta m	399.32	kg		
Mean daily leakage	4.99	kg/day		
Leakage rate	5.78E-05	kg/s		
Injection rate	0.0198	kg/s		
Injection time (s)	28800	s		
Injected mass	570.24	kg/day		
Performance	0.875	%		

Leakage rate calculation cycle1-81				Rock parameter
Properties	1	2		
P	5.31E+06	3.70E+06	Pa	TH
V	19.63	19.63	m ³	
R	286.9	286.9	J/kgK	
T	2.87E+02	2.92E+02	K	
time (s)	6912000			
delta m	398.21	kg		
Mean daily leakage	4.98	kg/day		
Leakage rate	5.76E-05	kg/s		
Injection rate	0.0198	kg/s		
Injection time (s)	28800	s		
Injected mass	570.24	kg/day		
Performance	0.873	%		

Leakage rate calculation cycle1-81			
Properties	1	2	Water parameter
P	5.30E+06	3.68E+06	Pa TH
V	19.63	19.63	m ³
R	286.9	286.9	J/kgK
T	2.86E+02	2.89E+02	K
time (s)	6912000		
delta m	395.51	kg	
Mean daily leakage	4.94	kg/day	
Leakage rate	5.72E-05	kg/s	
Injection rate	0.0198	kg/s	
Injection time (s)	28800	s	
Injected mass	570.24	kg/day	
Performance	0.867	%	

Leakage rate calculation cycle1-81			
Properties	1	2	Adapted permeability
P	5.51E+06	4.70E+06	Pa TH
V	19.63	19.63	m ³
R	286.9	286.9	J/kgK
T	2.86E+02	2.86E+02	K
time (s)	6912000		
delta m	195.66	kg	
Mean daily leakage	2.45	kg/day	
Leakage rate	2.83E-05	kg/s	
Injection rate	0.0198	kg/s	
Injection time (s)	28800	s	
Injected mass	570.24	kg/day	
Performance	0.429	%	

Leakage rate calculation cycle1-81			
Properties	1	2	Increased operational injection rate
P	5.25E+06	3.15E+06	Pa TH
V	19.63	19.63	m ³
R	286.9	286.9	J/kgK
T	2.86E+02	2.86E+02	K
time (s)	6912000		
delta m	503.21	kg	
Mean daily leakage	6.29	kg/day	
Leakage rate	7.28E-05	kg/s	
Injection rate	0.0396	kg/s	*2
Injection time (s)	28800	s	
Injected mass	1140.48	kg/day	
Performance	0.552	%	

Leakage rate calculation cycle1-81			Reduced operational injection rate	
Properties	1	2		
P	5.32E+06	3.87E+06	Pa	TH
V	19.63	19.63	m ³	
R	286.9	286.9	J/kgK	
T	2.86E+02	2.86E+02	K	
time (s)	6912000			
delta m	347.27	kg		
Mean daily leakage	4.34	kg/day		
Leakage rate	5.02E-05	kg/s		
Injection rate	0.0099	kg/s	*0.5	
Injection time (s)	28800	s		
Injected mass	285.12	kg/day		
Performance	1.522	%		

Leakage rate calculation cycle1-81			Increased global injection rate	
Properties	1	2		
P	1.03E+07	5.63E+06	Pa	TH
V	19.63	19.63	m ³	
R	286.9	286.9	J/kgK	
T	2.86E+02	2.86E+02	K	
time (s)	6912000			
delta m	1103.03	kg		
Mean daily leakage	13.79	kg/day		
Leakage rate	1.60E-04	kg/s		
Injection rate	0.0396	kg/s	*2	
Injection time (s)	28800	s		
Injected mass	1140.48	kg/day		
Performance	1.209	%		

Leakage rate calculation cycle1-81			Reduced global injection rate	
Properties	1	2		
P	2.74E+06	2.14E+06	Pa	TH
V	19.63	19.63	m ³	
R	286.9	286.9	J/kgK	
T	2.86E+02	2.86E+02	K	
time (s)	6912000			
delta m	145.32	kg		
Mean daily leakage	1.82	kg/day		
Leakage rate	2.10E-05	kg/s		
Injection rate	0.0099	kg/s	*0.5	
Injection time (s)	28800	s		
Injected mass	285.12	kg/day		
Performance	0.637	%		

Leakage rate calculation cycle1-81			Increased global AEP	
Properties	1	2	(C+R)	
P	5.61E+06	5.38E+06	Pa	TH
V	19.63	19.63	m ³	
R	286.9	286.9	J/kgK	
T	2.86E+02	2.86E+02	K	
time (s)	6912000			
delta m	55.28	kg		
Mean daily leakage	0.69	kg/day		
Leakage rate	8.00E-06	kg/s		
Injection rate	0.0198	kg/s		
Injection time (s)	28800	s		
Injected mass	570.24	kg/day		
Performance	0.121	%		

Leakage rate calculation cycle1-81			Reduced global AEP	
Properties	1	2	(C+R)	
P	4.78E+06	2.68E+06	Pa	TH
V	19.63	19.63	m ³	
R	286.9	286.9	J/kgK	
T	2.86E+02	2.86E+02	K	
time (s)	6912000			
delta m	504.68	kg		
Mean daily leakage	6.31	kg/day		
Leakage rate	7.30E-05	kg/s		
Injection rate	0.0198	kg/s		
Injection time (s)	28800	s		
Injected mass	570.24	kg/day		
Performance	1.106	%		

Leakage rate calculation cycle1-81			Increased AEP	
Properties	1	2	(C+R)	
P	5.30E+06	3.90E+06	Pa	TH
V	19.63	19.63	m ³	
R	286.9	286.9	J/kgK	
T	2.86E+02	2.86E+02	K	
time (s)	6912000			
delta m	335.03	kg		
Mean daily leakage	4.19	kg/day		
Leakage rate	4.85E-05	kg/s		
Injection rate	0.0198	kg/s		
Injection time (s)	28800	s		
Injected mass	570.24	kg/day		
Performance	0.734	%		

Leakage rate calculation cycle1-81				
Properties	1	2	Reduced AEP	
P	5.30E+06	3.67E+06	Pa	TH
V	19.63	19.63	m ³	
R	286.9	286.9	J/kgK	
T	2.86E+02	2.86E+02	K	
time (s)	6912000			
delta m	390.06	kg		
Mean daily leakage	4.88	kg/day		
Leakage rate	5.64E-05	kg/s		
Injection rate	0.0198	kg/s		
Injection time (s)	28800	s		
Injected mass	570.24	kg/day		
Performance	0.855	%		